Spin Dynamics of n-doped Gallium Arsenide

Matthew David Hodgson

Doctor of Philosophy

University of York
Physics

January 2014

Abstract

The emerging technology of spintronics promises to revolutionise computing by allowing considerably more energy efficient computing than is currently possible. Gallium Arsenide is one candidate material for use in semiconductor spintronic devices and as such detailed study of the spintronic properties of Gallium Arsenide is required. In this thesis we develop a semiclassical approach to the simulation of the electron population in Gallium Arsenide. We then use this model to look at the properties of the electron system, in particular the time taken for the electron population to undergo spin depolarisation. Comparison of the results to experimental values for the spin depolarisation suggest that the currently well accepted approach is accurate for low to moderate n type doping densities, but for higher densities there is a significant departure from the experimentally obtained results. We explore a number of improvements to the usual model showing substantial improvement in the range of densities that can be accurately predicted.

As Dilute Magnetic Semiconductors have been the topic of substantial research, we also apply the model to investigate the properties of an magnetic impurity in n doped Gallium Arsenide We compare the results to the Langevin enhanced Landau Lifshitz Gilbert equation, which shows good agreement allowing us to predict an appropriate damping constant as a result of the magnetic interaction with the electron population. We also investigate the nature of the noise felt by the magnetic atom showing that the usual white noise approximation is of limited validity.

Contents

List of Figures

List of Tables

Acknowledgements

I would not have been able to write this Thesis without the kind and generous support of many people around me, many of whom it is impossible to give a specific mention to here.

In particular I would like to thank my supervisors Irene D'Amico and Roy Chantrell as without their help, support and above all patience this thesis would not have been possible. Roy's dedication and generosity in giving up much of his Christmas break to help ensure this work was completed on time is worth a special mention here.

I would also like to thank Nigel Woolsey for his excellent advice as the non supervisory TAP member without whom it is quite likely that I would never have managed to complete on time.

This thesis would have not been possible without help in typing over last summer from Anna Ruth Rowan, who took excellent dictation when the pain in my arm was too severe and prevented typing. Her help always with a smile and full of enthusiasm helped me remember why I wanted to do this.

The nature of this work has always been a close collaboration with Gionni Marchetti, and any acknowledgement would be incomplete without mentioning the close nature of both our work and the friendship we have formed during our PhDs. It is hard to imagine how this work would even have started without the collaboration with Gionni.

A good support system is essential to surviving a PhD, while many have contributed a special mention should be made to all past and current residents at 43a Moorland Road, not least of whom Jenefried without whose support and belief in me, I would at times have been truly lost. Without the strong friendships I doubt my sanity would have survived the more difficult

times and the good times would not have been so good. I will always fondly remember the many Sunday roasts had together.

I would like to say a heartfelt thanks to my parents, brother and sister for their unequivocal support throughout my PhD and in particular my Dad for help with proof reading.

Finally I would like to thank everyone that has made York University, and in particular the Physics department, an exceptionally warm and welcoming place.

Declarations

I declare that the work presented in this thesis, except where otherwise stated, is based on my own research and has not been submitted previously for a degree in this or any other university.

This work was done in close collaboration with Gionni Marchetti and was supervised by Dr. Irene D'Amico and Prof. Roy Chantrell. In particular the derivations of the screening length and the third body correction were carried out by Gionni Marchetti (presented in Chapter 5) while the implementation of the classical forces (also in Chapter 5) was entirely conducted by myself. The basic model was implemented primarily by me, while Gionni did contribute to the development of various parts including the implementation of an early version of the routine responsible for rotating an electron's momentum once the scattering angle had been decided and he carried out the implementation of the reduced units used internally by the simulation and the method for converting between those units and SI units. The decisions taken on which scattering mechanisms to implement was a joint decision, with Gionni taking the lead role in the choice of approximations used to derive the various scattering rates and which of a variety of scattering formulas to implement.

The data for all the graphs, unless explicitly stated otherwise, were produced, analysed and plotted by myself. Signed

Matthew Hodgson

Chapter 1

Introduction

Spintronics[1] is an emerging technology that aims to exploit the spin properties, and the associated magnetic moment, as well as the charge properties of electrons in solid state devices, including semiconductor lasers [1], spin based transistor [2] and MRAM (Magnetoresistive Random Access Memory) [3]. The increased drive to research spintronic devices, as well as other emergent technologies, is motivated by a lack of long term plans for the continued improvement of standard silicon devices [4, 5, 6, 7].

It is worth noting, at this point, that the classical analogy for spin, that of a particle classically spinning on its own axis, is unhelpful if not actually misleading and so far any attempt to find an accessible classical-like explanation of spin has failed. This is of no great concern as we are primarily interested in the practical applications of this property and accepting the mathematical origin of spin (as a consequence of the unification of quantum theory with special relativity and a requirement for angular momentum to be conserved [8]) and its experimental observation should suffice. In this regard we should no more be concerned by a lack of understanding of the

---

[1] A portmanteau of spin and electronics

origin of an electron's spin than we are of the origin of its charge.

In recent years there has been increased concern [9] over the break down of the so called "Moore's law", the observation that the size of a transistor available in commercial device halves every eighteen months [10]. While Moore's law was originally intended only to consider transistor size until the early 2000s it could be applied to almost any metric of computing power be it floating point operations per second, hard drive disk capacity [11] or drawn triangles per second[2] [13].

Spintronics is not the only potential to this crises within the electronics community, with active investigation also into quantum computing [14], DNA computing [15] and optical computing [16], amongst others. Each of these alternative technologies have the potential to revolutionise computing, however spintronics is generally considered the most likely to succeed in part because it allows much of the current technology associated with device fabrication to be reused.

Quantum Computing is perhaps the most promising of the alternatives to spintronics amongst the emerging technologies. Quantum computing relies on the manipulation of entanglement [14] between quantum bits ("qubit") and as such relies on the maintaining of coherent states during the operation of the quantum computer, an idea not dissimilar to the requirement in spintronics for the maintaining of a coherent net spin. The promise of quantum computing is not a gradual increase in the performance of a computer but in a dramatic change to the types of problems computers can solve efficiently[3].

---

[2] A measure of the performance of a graphics processing unit, graphics cards draw all elements of a 3D environment by rendering a polygon mesh consisting of many triangles [12]

[3] A sufficiently large classical computer can simulate a quantum computer, although without the performance increases, so it does not change the types of problems that can be, in theory solved, as such the gains from quantum computing does not invalidate the Church-Turing Thesis [17]; that a function is computable if, and only if, a Turing machine can compute it.

The exact class of problems that a quantum computer would improve is not known [18], but is known to include key problems; for example integer factorisation, which would make much modern encryption essentially useless. The limitation of the range of problems[4] that they can solve faster than a classical computer suggests that the use may be limited to national governments and research institutions, rather than mass consumer use[5].

Optical and DNA computing aim to replace the semiconductor technologies with alternative materials than allow for greater speed of calculation. Optical computers aim to replace the flow of current with lasers, increasing significantly the data bandwidth and in principle speed of calculation. The need to replace the semiconductor transistor with an optical equivalent, consisting of a material with non-linear refractive index makes optical computation expensive and while optical logic gates have been developed, so far they require more power, have failed to be miniaturised and offer little benefit over conventional electronics [20]. DNA computing similarly looks to replace the integrated circuit, in this case with biological molecules, fundamentally the promise of DNA computing is massive parallelisation which for many applications would allow a massive performance gain. To date there has, despite the implementation of DNA logic gates, been limited success [15] in comparison with conventional computing.

The field of spintronics emerged from a series of discoveries in the 1980s most famously the discovery of giant magnetoresistance (GMR), in 1988 by Albert Fert *et al.* [21]. In these experiments it was shown that the spin properties of an electron can, in a well chosen device, have a profound

---

[4] The NP complete class of problems is generally regarded, but not proven, to not be in the class of problems that can be more efficiently solved on a quantum computer [19].

[5] Although the parallels here to the infamous "There is a world market for maybe five computers" allegedly said by Thomas Watson, CEO of IBM in 1943, cannot entirely be ignored.

impact on the electronic properties. This discovery opened the possibility of computation involving the spin component of the electron as well as the electronic charge.

GMR is the variable electrical resistance observed in thin film layers of adjacent ferromagnetic materials in either parallel or anti parallel alignment. In the anti-parallel alignment the electron current becomes spin polarised as it passes through the first magnetic layer and then on reaching the second layer requires a significant amount of energy to overcome the energy barrier from the opposite magnetic field. In the parallel case there is no energy cost associated with crossing into the second layer and as such the resistance is much lower [21]. This has a wide variety of industrial applications the most famous of which is in hard disk drives which relies on the effect to read the state of a particular bit [22]. The enormous practical application of this discovery resulted in it being awarded the 2007 Nobel prize.

The practical applications of spintronics are expected to move beyond the use in storage technologies and into semiconductor logic in commercial devices by around 2025[6], replacing the current CMOS logic which is increasingly running into difficulties with further miniaturisation. Complementary-Metal-Oxide-Semiconductor[7](CMOS), is a style of circuitry design used in integrated circuits [23], including microprocessors and microcontrollers.

The important innovation of CMOS devices was the existence, for each logical unit, of a p doped and an n doped channel, the aim being to create at all times a high resistance path between the high voltage and earthed lines (the p-doped channel has a high resistance for positive voltage difference and low for the reverse, while the n-doped channel has the opposite behaviour

---

[6] The 2025 estimate originates from the International Technology Roadmap for Semiconductors http://www.itrs.net/

[7] The name is now somewhat archaic; as modern CMOS devices no longer use the metals or oxides in the field effect transistors that the technique was named for.

[23]). During switching however both channels allow current to flow, and it is during this time that power usage is highest. CMOS logic has allowed significant miniaturisation however there are a number of difficulties with miniaturisation significantly beyond current levels as a range of finite size effects, including current leakage through ever thinner insulating layers, and increased difficulty in keeping the device within operating temperatures are becoming significant [24].

Spintronics aims to significantly improve the power usage, and hence heating problems, by the introduction of the idea of spin current. An ideal, or pure, spin current consists of a flow of spin up polarised electron while in the opposite direction there is a flow of spin down electrons [25], the result is that there is no net flow of current as a result a device, using spin currents would have extremely low power dissipation[8]. This lower power usage is incredibly important in its own right, as currently more than half of the power consumed by electronic devices is due to the energy cost of cooling [27] key components, additionally lower power usage opens the possibility of non-volatile logic [28]. Current computer logic relies on maintaining a constant flow of current without which the information is lost, non volatile computing would allow a loss of power to merely stop further calculations, but would not cause data loss.

The interest in spintronics is extremely broad, with interest in material properties of semiconductors, metals and half-metals. Half-metals are materials that have band structure that is different for the majority and minority spin channels, resulting in an energetically favourable spin direction. As a result half-metals show spontaneous polarisation even in the absence of an applied magnetic field; as such all half metals are by definition ferromagnetic

---

[8] The spin coulomb drag effect however does mean that even though there is no net current there will still be some dissipation [26].

(or at least ferrimagnetic) although only a small minority of ferromagnets are half metals [29]. by showing strong polarisation of the electron spin population are interesting for spintronic applications, especially for injection of a spin polarised current [30]. This half-metal spin polarisation has been observed in the Heusler alloys, a broad class of materials with substantial research interest.

There are over 20 Heusler alloys so any discussion of the precise properties is impossible but in general Heusler alloys are face-centred cubic crystals consisting of non ferromagnetic elements but overall they are ferromagnetic due to a double exchange mechanism between neighbouring ions [31]. This results in a significant Curie temperature with room temperature ferromagnetism being commonly observed, for example the original Heusler alloy (Cu_2MnSn) has a Curie temperature of 630 K. In most Heusler alloys the magnetic moment lies almost solely on the atom at the centre of the cubic structure, usually a manganese atom.

In this work we concentrate on the properties of n doped Gallium Arsenide (GaAs) as a candidate material for spintronic technologies. GaAs is a III/V semiconductor which has been used in a range of devices including integrated circuits, laser diodes and solar cells [32, 33]. GaAs is a good candidate for spintronic devices as it has the desired spintronic properties, particularly a high spin depolarisation time allowing the manipulation of spin currents, as well as being amenable to fabrication on an industrial scale [32] indeed GaAs has already been used in place of silicon, most notably the Cray-3 supercomputer[9]. GaAs junctions can function at very high frequencies (around 250 GHz), much faster than silicon devices, and are much

---

[9] Which due to inadequate commercial backing was a complete failure, managing to secure only one order and eventually resulted in the bankruptcy of Cray Computer Corporation [34]

less heat sensitive than silicon junctions, due to possessing a large band gap [35].

The low hole mobility [32] in GaAs prevents the use of CMOS logic gates and as a result conventional computing using Gallium Arsenide has generally required large amounts of power[10]. This drawback is not present in a spintronic system, which will look to implement spin currents rather than the more conventional current.

The electronic properties of GaAs have motivated interest in it as a potential material for spintronic devices. GaAs lacks a preferred spin orientation which allows it to sustain a spin current consisting of equal numbers of spin up and spin down electrons. This would allow the propagation of spin currents in GaAs, however these currents will not be extremely long lasting due to the spin depolarisation mechanisms present in GaAs. GaAs lacks inversion symmetry, as it is a compound semiconductor, and as such a charge carrier experiences strong spin-orbit interaction (the Dresselhaus term) [36] (more details in Chapter 2). This spin-orbit interaction results in an effective magnetic field which lifts the degeneracy between up and down electrons for any electron with non-zero momentum. The spin orbit interaction is highly dependent on the electron momentum and as such each electron is likely to feel a very different effective magnetic field, around which the spin part of the electron wavefunction will precess in Larmor precession (i.e. the magnetic moment precesses around the applied magnetic field).

The depolarisation can only be explained by considering an ensemble of electrons. Initially all electrons have the same momentum and spin. As the Dresselhaus field depends only on momentum they all experience the same effective field and as such precess around it maintaining coherence.

---

[10] As noted earlier CMOS logic requires two similar channels, one n doped and one p doped

The direction of spin polarisation may change but the magnitude of the ensemble averaged spin should remain constant. In reality the different electrons over time become scattered resulting in different electrons having different velocities and therefore different effective fields. As each electron will exhibit Larmor precession around a different field over time they will come to be out of phase with each other and therefore the average spin will eventually decay. This depolarisation mechanism is known as the D'yakonov Perel (DP) spin relaxation.

There are other spin depolarisation mechanisms such as the Elliott-Yafet mechanism (caused by scattering events not being spin symmetric), the Bir-Aronov-Pikus mechanism (caused by electron-hole exchange interactions) and hyperfine interactions with nuclear spins. These mechanisms are however generally much weaker than the DP mechanism in GaAs so this work concentrates only on the depolarisation caused by the D'yakonov Perel relaxation mechanism.

In addition to the use of doped Gallium Arsenide for the medium in which spin currents travel and various devices, additional possibilities are created by the introduction of magnetic impurities. These can be introduced as an addition or as a replacement to the usual doping. These materials, dilute magnetic semiconductors (DMS) have generated interest due to their unusual properties [37]. These materials have a somewhat controllable magnetic properties which can be tuned by varying the concentration and type of the magnetic impurities making them of interest for spintronics research [38, 39, 40].

This work is a theoretical approach to simulating large scale n-doped, bulk, Gallium Arsenide with the aim to find the spin properties of the system and how they vary with density and temperature. To handle this problem we use the ensemble Monte Carlo simulation [41], which treats the electrons semiclassically with random scattering events representing the interaction with the environment (including each other). The ensemble Monte Carlo approach is a stochastic method for numerical simulation of transport problems, by solving the Boltzmann transport equation [42] which has recently been adapted to handle the problem of spin transport [43]. The use of the ensemble Monte Carlo technique forces us to pay particular attention to the electron-electron interaction, which for simple transport could be neglected (as it does not change the average momentum), which is notoriously difficult to solve and which previous attempts have had only limited success with.

1.1 Structure of this Document

The work as a whole first describes the ensemble Monte Carlo technique, the choice we have made as to which scattering mechanisms to include and the various numerical techniques used to efficiently carry out the time evolution of the electron. We then discuss the material properties our model predicts for GaAs samples around 300 K for a large range of densities, showing that we have a good agreement with experiment for most of the experimental range. To further improve this agreement we show a number of ways of going beyond the basic model, and show that using the classical forces to carry out the electron-electron and electron-impurity interactions is an improvement over the scattering approaches. Finally we look at the impact of introducing a single magnetic impurity, and how that impurity behaves in a an applied field.

In Chapter 2 we detail the ensemble Monte Carlo technique and our implementation of it. We also outline the procedure used to calculate the various scattering rates including derivations of non-relativistic scattering theory, and the approximations used to handle the electron-electron and electron-ionized impurity scattering. The numerical scheme for updating the momentum of the electrons and the detail of the spin orbit interaction are also shown here.

In Chapter 3 we discuss the novelties introduced by our technique, including an accurate way to determine the spin depolarisation time, our attempt to localise the electron-electron scattering and the numerical technique used for the evolution of the spin part of the electron wavefunction. We also verify that our simulation is producing physically reasonable behaviour by testing the thermalisation of our electron population and outline the thermalisation procedure used to typical calculation runs.

In Chapter 4 we show the results of our model, particularly detailing the role of the various scattering mechanisms at a range of densities and determine a suitable value for the spin-orbit interaction coupling constant (a_{42}[11]). We then show the resulting spin depolarisation times for system and a range of densities and temperatures showing particularly strong agreement up to densities of around $n = 10^{17}$ cm^{-3}.

In Chapter 5 we present a number of potential improvements over the basic model, presented in Chapter 4, these include corrections for degeneracy effects at higher densities and a correction in the electron-electron scattering rates due to the presence of a third scattering body. We then discuss an approach based on solving the problem using classical electrostatic forces, which shows a considerably better behaviour throughout the entire impurity density range studied. In order to use this approach we are forced to take a computational approach, known as the Barnes-Hut approach [44], to allow long range interactions to be treated as the interaction with groups consisting of many particles, characterised by their mean position and net charge (otherwise the number of interactions rises too quickly with increased particle number and soon becomes computationally intractable).

In Chapter 6 we analyse the impact of the introduction of a single magnetic spin site and show that interaction with the electron "gas" causes it to thermalise to an applied magnetic field. To allow simulations over a larger scale we introduce the Landau-Lifshitz-Gilbert equation, an approach to the simulation of micromagnetics, and parametrise the behaviour of the spin in our electron gas in terms of the Gilbert damping constant α. Importantly we show that the noise experienced by the magnetic spin as a result of the interaction with the electron population cannot be considered to be a white

---

[11] This constant is relatively poorly known with a very wide range of values suggested by theory and experiment

noise heat bath, which is a current approximation used in the overwhelming majority of all current ultrafast laser induced magnetisation processes, with notable exceptions showing that the type of noise can make a substantial difference. [45]

Chapter 2

Method

2.1 Ensemble Monte Carlo

In order to study spin de-coherence we need to be able to simulate a very large number of particles (of the order of 10,000). This is not computationally tractable for a fully *Ab Initio* approach, so instead we use the Ensemble Monte Carlo (EMC) technique [41]. The EMC technique works by treating the charge carriers (in this case the electrons) as classical particles up to scattering events which are generally quantum mechanical in nature.

To carry out an ensemble Monte Carlo calculation we start with a conventional molecular dynamics calculation, where we update the momentum, position and forces acting on each particle at fixed time steps, use some form of numerical integration to calculate the new values for these properties and then iterate over many time steps to carry out the evolution over a suitable time scale. In addition to this traditional molecular dynamics approach we introduce “scattering events”, this can be used to include interactions with objects not directly in the simulation (for example we could consider the impact of laser heating as a scattering mechanism) or as a way of going beyond the classical interaction allowing us to also consider some quantum effects of interactions between our particles. The implementation of the scattering relies on knowing the scattering rate for each particle, we then calculate the appropriate time to the next scattering event and update the position and momentum of the scattered particle to that time (which will be less than the time to the next time step) and apply the scattering. The scattering will in general alter the momentum of the particle by changing the angle and/or the magnitude of the velocity. Once we have carried out the scattering for one particle we then iterate over many particles until we reach the time step and which point all particles are updated to that point in time, notably particles that have scattered since the previous time step will need updating by a smaller amount than those that have not scattered.

In general ensemble Monte Carlo treats the scattering events as being instantaneous and uncorrelated[1] [41]. As such the scattering rate only depends on the properties, typically momentum, of the charge carrier.

2.1.1 Self Scattering

For numerical convenience we would like each particle to have a constant scattering rate, and that each particle has the same scattering rate. To achieve this we will introduce a fictitious scattering ("self scattering") [46] which does not affect the particle but simply ensures the total scattering rate remains constant. This results in the probability distribution for the time between scattering for one particle of $p\left(\tau_{scatter}\right) = \exp(-\tau_{scatter}\Gamma)$, where Γ is the maximum scattering rate, or $p\left(\tau_{scatter}\right) = exp(-\frac{\tau_{scatter}}{N}\Gamma)$ for N particles. As each particle is equally likely to be the next to scatter, irrespective

---

[1] That is the scattering rate depends only on properties of the electron being scattered, not on how recently it scattered, as some scatterings can induce a change in momentum or energy of the particle there can still be some induced correlations

of when it last scattered, this can be used to calculate the next scattering time for any particle; we can then choose the next particle in a uniform random way with each particle having equal probability of scattering.

This “self scattering” is simply a numerical simplicity taking advantage of the relative ease of generating numbers with an exponential decay.

The EMC technique, as the name suggests, is a Monte Carlo technique and as such makes heavy use of pseudo random numbers. Throughout this work we use the 32 bit Mersenne twister algorithm [47] as the source of random numbers. This random number generator has very good properties showing long correlation times, no discernible biases and passes most, but not all, of the “Diehard Tests”[2]

2.1.2 Ensemble Monte Carlo & the Classical Picture

The ensemble Monte Carlo technique is normally described in two ways, firstly as a solution to the Boltzmann transport equation,

$$\frac{df_{\vec{k}}}{dt} + \underbrace{\frac{1}{\hbar}\nabla_{\vec{k}}E_{\vec{k}} \cdot \nabla_{\vec{r}}f_{\vec{k}}}_{\text{Dispersion Relation}} + \underbrace{\frac{F}{\hbar}\nabla_{\vec{k}}f_{\vec{k}}}_{\text{Classical Forces}} = \left(\frac{df_{\vec{k}}}{dt}\right)_{coll}, \qquad (2.1)$$

and secondly as classical motion plus scattering. It is worth noting the extent to which the two explanations are equivalent. There are a few ways in which the classical model plus scattering may lead to a misunderstanding of the actual physics being considered, the most obvious and important is the dispersion relation, which gives rise to a mass like term, provided the band structure is sufficiently parabolic and the energies involved are small enough, the use of a classical mass can be justified, although we should of course use the effective mass not the normal electron mass (For Gallium Arsenide

---

[2] A selection of very strict tests for randomness of a set of data [48].

any error, due to non parabolicity, is small and in this work we neglect any corrections beyond the parabolic band structure). Secondly Umklapp processes would not be apparent from a classical picture but are, in principle, present in any periodic system although in the case of Gallium Arsenide at or close to room temperature they are vanishingly rare. Additional issues with the classical picture are introduced if the energy required to create a electron-hole pair is readily available, again in GaAs at the temperatures we are considering this is a non issue.

The classical picture will always struggle to cope as we head into the degenerate regime, in that case though the overall approach is weakened but some attempt can be made to cope with degeneracy one approach is outlined in Chapter 6 but otherwise is sufficiently robust to give a good intuitive feel of the system.

2.1.3 Structure of this document

In this chapter we will go on to discuss the implementation of the various aspects of the ensemble Monte Carlo technique, as implemented in our simulations. The next section deals with the calculation of the scattering rates for the various important scattering mechanisms in n-doped Gallium Arsenide, starting with the theoretical framework for calculation of scattering properties including the Born Approximation (Section 2.2) then moving onto the scattering rates, and typical scattering angles, for each of the scattering processes (Section 2.3). This is followed by a section on the deterministic motion, including how we handle both the momentum updates (using the velocity verlet algorithm) and a discussion of the field present that causes the individual spins to precess due to the presence of a spin-orbit field (Section 2.4). Additional notes on implentation are also present in Chapter 3 where we discuss some of the fine details of how we implement the electron-electron scattering, and how that compares to previous work, and how we carry out the spin evolution (using the Crank-Nicoloson scheme).

In Chapter 6 we discuss some approaches to further improving how we the electron-electron interaction is handled, of particular importance here is the classical electrostatic approach which replaces the electron-electron interaction via a scattering mechanism, this technique shows excellent agreement over a wide range of impurity doping densities and is the method we recommend for general use, this approach had not previously been implemented due to extreme computational cost, and we describe and approach for minimising this issue.

2.2 Scattering Theory

Scattering theory has an important history in the explanation of many physical phenomena. Although to some extent known (at least for classical theory) for some time, modern scattering theory was developed in the early days of quantum theory [49], and is referred to throughout as conventional scattering theory. The scattering mechanisms for our simulation can in principle be taken from *Ab Initio*, experimental or conventional scattering theory. Here we use conventional scattering theory to derive appropriate scattering rates and the corresponding anisotropy in the scattering angle. Conventional scattering theory relies on two key results from quantum mechanics, Fermi's golden rule and the Born approximation, although higher order approximations can be invoked when necessary. In both cases these are low order approximations that assume that the scattering is small. The energies obtained by carriers in a typical semiconductor device are sufficiently low we need only consider non-relativistic scattering theory, which makes solving the problem significantly simpler computationally.

2.2.1 Total Scattering

The total scattering is the characteristic quantity in any scattering process. It is defined in terms of a scattering cross section, σ_{tot}, which represents the total chance of scattering into any state. The exact definition arises naturally from the way scattering experiments are conducted. We consider a well collimated beam of particles of a known energy, E, directed at a target containing a macroscopic scale sample of scattering centres (generally particles, but it could equally be a material with a known defect density). σ_{tot} is determined, experimentally, by the placing of suitable detectors in the path of the transmitted beam. The measured intensity compared to the initial intensity gives a definition of the total scattering cross section

$$\frac{F_i}{F_t} = \frac{n\sigma}{A}, \tag{2.2}$$

where F_i and F_t are the incident and transmitted flux respectively, n is the number of scattering centres and A is the area of the beam [50]. The idea of a scattering cross section is that of an area, per scattering centre, that if the incoming particle passes inside it will cause it to scatter with the scattering target (classically a hard sphere approach which has particles scattering if, and only if, they contact the surface of the sphere). Although this idea has a good connection with classical scattering theory, caution is needed in applying it quantum mechanically. Of particular note is that the scattering rate can vary strongly with the energy. We are normally more interested in the differential cross section, $\frac{d\sigma}{d\Omega}$, which represents the scattering rate into a given solid angle Ω [51] as this allows us to go beyond merely knowing if a particle will scatter, by determining how much it will scatter.

2.2.2 Fermi's Golden Rule

Fermi's golden rule is a fundamental result of quantum mechanics, it allows the calculation of the transition rate from an eigenstate[3] of the quantum system to a continuum of states, due to a perturbing field,and is so named because Fermi referred to it as one of the golden rules of quantum theory.

Assumptions

Consider a potential of the type $V' = V(x) + v(x,t)$ where $v(x,t)$ is a weak perturbing potential Assuming the perturbing potential is switched on at

---

[3] More strictly from an eigenstate state or from a very narrow range of practically indistinguishable eigenstates states, as the derivations rely on results based on a density of states argument

$t = 0$ and then ceases to change, until it is switched off, and that before the potential is "switched on" the wave function is in an eigenstate state of energy E_k. Then providing that the potential is weak enough, or it is switched on for a short enough time, any transition is minimal. Writing the unperturbed wavefunction as

$$\Psi(x,t) = e^{-iEt/\hbar}\psi(x), \tag{2.3}$$

where ψ are the solutions of the time independent Schroedinger equation for the unperturbed system, we can write the perturbed wavefunction as

$$\Psi'(x,t) = \sum_n a_n(t)\psi(x). \tag{2.4}$$

Derivation

Substituting into the Schroedinger equation for the perturbed system gives

$$\underbrace{\sum_n a_n \left[-\frac{\hbar^2}{2m}\frac{\partial^2\Psi_n}{\partial x^2} + V\Psi_n - i\hbar\frac{\partial\Psi_n}{\partial t}\right]}_{\text{Unperturbed Term}} + \sum_n a_n v\Psi_n - i\hbar\sum_n \frac{da}{dt}\Psi_n = 0, \tag{2.5}$$

the first term of which is zero as it is just the Schroedinger equation for the unperturbed system. If we then multiply by the complex conjugate of some Ψ_m and integrate over all space this reduces to

$$\sum_n a_n e^{-i(E_n-E_m)t/\hbar}\int \Psi_m^* v\Psi_n d\tau = i\hbar\sum_n \frac{da_n}{dt}\int \Psi_m^*\Psi_n d\tau. \tag{2.6}$$

As Ψ_m and Ψ_n are orthonormal this can be further reduced to

$$\sum_n a_n e^{-i(E_n-E_m)t/\hbar}\int \Psi_m^* v\Psi_n = i\hbar\frac{da_m}{dt}. \tag{2.7}$$

If we start in the eigenstate state, k, then at $t = 0$ we have $a_k = 1$ and for a sufficiently small perturbation at any time later $a_k \approx 1$ and $a_n \ll 1$ for any $n \neq k$

$$\frac{da_n}{dt} = -\frac{i}{\hbar} e^{i(E_k - E_n)t/\hbar} v_{nk}, \tag{2.8}$$

where v_{nk} is $\int \Psi_n^* v \Psi_k d\tau$. So

$$a_n(t) = v_{nk} \frac{1}{\Delta E} \left[e^{-i\Delta E t/\hbar} - 1 \right], \tag{2.9}$$

where $\Delta E = E_k - E_n$. The physically meaningful quantity is $a_n^* a_n$, as it represents the probability of finding the particle in the new state, is

$$a_n^*(t) a_n(t) = \frac{v_{nk}^* v_{nk}}{\hbar^2} \frac{\sin^2\left(\frac{\Delta E}{2\hbar} t\right)}{\left(\frac{\Delta E}{2\hbar}\right)^2}. \tag{2.10}$$

Note that the energy range in which we expect to find a transition decreases with increasing time, due to the $\left(\frac{\sin(X)}{X}\right)^2$ term. This gives the occupancy of any state $n \neq k$ and we can define a probability of transition to any state as $P_k \equiv \sum_{n \neq k} a_n^* a_n$

If we consider the special case of scattering to a continuum of states defined by a density of states, ρ_n and that ρ_n and v_{nk} vary slowly then we get

$$P_k = v_{nk}^* v_{nk} \rho_n \frac{2}{\hbar} t \int_{-\infty}^{\infty} \frac{sin^2(X)}{X^2} dX, \tag{2.11}$$

where $X = \frac{\Delta E t}{2\hbar}$ And we have, by integration, Fermi's Golden Rule [52]

$$R_k = \frac{2\pi}{\hbar} v_{nk}^* v_{nk} \rho_n, \tag{2.12}$$

where R_k is the rate of transition from the state k.

2.2.3 Born Approximation

The Born Approximation is a first order perturbation approach to scattering theory. It is this approach that we employ to derive the scattering rates and the form of the anisotropy, where relevant, for the scattering mechanisms. If we consider a general potential $U(r)$ with a typical magnitude of $|U|$ and typical length a acting on a particle of mass (or reduced mass) m and velocity v then the Born approximation is valid if either [53]

$$|U| \ll \frac{\hbar^2}{ma^2}, \tag{2.13}$$

or

$$|U| \ll \frac{\hbar v}{a}. \tag{2.14}$$

That is the Born approximation holds for sufficiently weak potentials, or for sufficiently fast particles in any potential. The first of these conditions is equivalent (for an attractive potential) to saying that the potential is not strong enough to allow the formation of bound states. This is a not unsurprising condition as the formation of bound states would lead to the particle having a chance of spending some time bound to the attractive potential delaying the scattering.

Consider a beam incident on the region of scattering, represented as a plane wave

$$\Psi(r) = Ae^{i\vec{k}\vec{r}}, \tag{2.15}$$

where $k = \frac{mv}{\hbar}$ and A is required for normalisation, if we assume the wave is contained in a Volume L^3 then $A = L^{-\frac{3}{2}}$.

As the potential is usually centrosymmeteric we naturally want to use spherical polars with the potential centred on the origin

$$\Psi(r) = Ae^{i\vec{k}\vec{r}\cos\theta}, \tag{2.16}$$

or

$$\Psi(r) = Ae^{i\vec{k}\cdot\vec{r}}, \tag{2.17}$$

and a particle travelling in a different direction with velocity v'

$$\Psi(r) = Ae^{i\vec{k}'\cdot\vec{r}}. \tag{2.18}$$

The problem is in essence to find at what rate does the potential $V(r)$ cause the transition from $\vec{k}$ to $\vec{k}'$ As the k' states are essentially continuous we can apply Fermi's golden rule (2.12) Assuming the particle is initially in the eigenstate state k and that transition is rare this becomes

$$R_k = \frac{2\pi}{\hbar} V^*_{\vec{k}'\vec{k}} V_{k'\vec{k}} \rho\vec{k}', \tag{2.19}$$

where $\rho_{\vec{k}}$ is the density of states of k over a small solid angle, $d\Omega = 2\pi\sin(\theta)d\theta$, and $V_{\vec{k}'\vec{k}}$ is the matrix element of the potential between $\vec{k}$ and $\vec{k}'$ that is

$$V_{\vec{k}'\vec{k}} = \int V(r)e^{i(\vec{k}'-\vec{k})r}d\tau, \tag{2.20}$$

and

$$\rho_{\vec{k}} = \frac{mL^3\left|\vec{k}\right|}{8\pi^3\hbar^2}d\Omega. \tag{2.21}$$

Defining $S(\theta)$ to be the scattering per unit time into a state with an angle different by θ, and using the solid angle $d\omega$ we have

$$S(\theta) = \frac{mL^{-3}\left|\vec{k}'\right|}{4\pi^2\hbar^3}, \tag{2.22}$$

using

$$S(\theta) = \frac{d\sigma}{d\Omega} I, \tag{2.23}$$

where I is the incident flux. We can finally write the Born Approximation as [53]

$$\frac{d\sigma}{d\Omega} = \frac{S(\theta)}{I} = \left(\frac{m}{2\pi\hbar^2}\right)^2 V^*_{\vec{k}'\vec{k}} V_{\vec{k}'\vec{k}}. \tag{2.24}$$

2.2.4 Linking Scattering Rate to Scattering Cross-Section

Most scattering calculations rely on the concept of a scattering cross section (σ), discussed later, equivalent to an area in which the particle will undergo scattering. For ensemble Monte Carlo though, a scattering rate, a typical rate of scattering events, is more useful as it can be more readily implemented in our simulation. For the two ideas to be comparable a number of conditions must be met. The media must only slowly vary in concentration of scattering centres and the cross section must be much smaller than the typical distance between scattering centres. In that case we can define Γ_{event} [53] to be the typical time between scattering events, where

$$\Gamma_{event} = \frac{nv\sigma}{8\pi^3}, \tag{2.25}$$

here n is scattering centre number density, v is the particle velocity and σ is the total scattering cross section. We can combine numerous different scattering events to give a total $\Gamma_{tot} = \Gamma_1 + \Gamma_2 + \ldots$ as the rate of any scattering happening to an individual particle.

2.3 Important Scattering Mechanisms in GaAs

While a large number of scattering mechanisms are present in real GaAs systems, such as neutral impurity scattering [54], scattering to higher bands [35] and interface scattering [55]. We model only the more important mechanisms (polar optical phonons, acoustic phonons, ionised impurities and electron-electron scattering), the others play only a small role, or are important under conditions not studied here (such as in the presence of a strong applied field). Of these the electron-electron scattering is the only event that scatters simultaneously two particles in our simulation and as such plays an especially important role in the model, it should be noted here that the careful handling of the electron-electron scattering is detailed in Chapters 4 & 5 where we eventually conclude that the best approach is not a scattering approach.

2.3.1 Ionised Impurities

The ionised impurities (both the doping material and the free electrons) can be simulated in two distinct ways. Firstly, scattering can be considered using the quantum mechanics already discussed. To do this we must make a number of assumptions about the nature of these particles, for example, we treat them as being uniformly distributed throughout the system and that they are effectively screened by the presence of the other charged particles. The other approach is to consider the electron population as a classical system feeling classical electrostatic forces, this approach is discussed in detail in the later half of Chapter 5. Here we introduce the approach taken when treating it as a scattering event, the results of which are detailed in Chapter 4.

Yukawa Type Screening

The scattering rate for a long ranged interaction, becomes infinite, which is clearly unphysical. To prevent this we introduce a screened interaction, this originates in the screening played by the electron population which reduces the long range Coulomb effects felt in the device. The simplest form of the electronic screening is a Yukawa type (screened Coulomb) approach [56] which has the form

$$V_y(r) = -g^2 \frac{e^{-\lambda r}}{r}. \tag{2.26}$$

This approach depending on the value for λ, the screening length, includes a large range of possible screening types including a Debye type screening, that we introduce here, an alternative more detailed screening calculation is presented in Chapter 5.

Debye Screening

In the classical, non-degenerate limit (low doping densities [57]) we would expect any form of the screening to approach the Debye limit. The Debye limit is derived assuming weak fields and assuming the electron gas can be treated as a continuum over the length scales considered. Starting with Poisson's equation [58],

$$\nabla^2 \phi = -\frac{\rho}{\epsilon_0 \epsilon_b}, \tag{2.27}$$

where ρ is the excess charge ($\rho = (n_i - n_e)e$). Here we will assume that the ionized impurities play no role in the screening, as they are stationary. Considering a localised potential then we would expect that a long way from it the electron density would be in equilibrium, that is $n_e = n_i = n_\infty$. Also assuming that the electron population is in thermal equilibrium and that the total of excess electrons is much smaller than the total number of electrons then we also have (from the Boltzmann distribution i.e. $p(x) \propto \frac{E_x}{k_B T}$, i.e. the probability of occupation of a given microstate of energy E decays for increasing energy, at a given temperature.)

$$n_e = n_\infty \exp\left[\frac{e\phi}{k_b T}\right]. \tag{2.28}$$

Substituting into Poisson's equation we get

$$\nabla^2 \phi = \frac{e n_\infty}{\epsilon_0 \epsilon_b}\left(\exp\left[\frac{e\phi}{k_b T}\right] - 1\right). \tag{2.29}$$

Linearising the above expression by assuming that $\frac{e\phi}{k_b T} \ll 1$ then we get

$$\nabla^2 \phi = \frac{e^2 n_\infty}{\epsilon_0 \epsilon_b k_b T}\phi + \mathcal{O}(\phi^2), \tag{2.30}$$

which has exponential solutions and therefore allows us to define a distance, $\lambda_D^2 = \frac{\epsilon_0 \epsilon_b k_b T}{e^2 n_\infty}$ [59], the Debye length over which ϕ is screened. For this expression to be reliable the electron population must behave as a non-degenerate gas ($E_{\text{Fermi}} \ll k_b T$) and the electron population must behave as a continuum; i.e. there must be a large number of particles over a sphere the size of the Debye length. We can define the plasma parameter [60], $N_D = \frac{4}{3}\pi\lambda_D^2 n_\infty$, to test this which must be large for the Debye screening to have validity. Practically in our simulations for much, if not all, of the range the later criterion is not met as strongly (if at all) as one would hope (See Figure 2.1) and further corrections are needed to compensate for this. In addition at higher densities the non-degeneracy approximation does not hold and corrections must be made for this, one approach to handle this is outlined in Chapter 5.

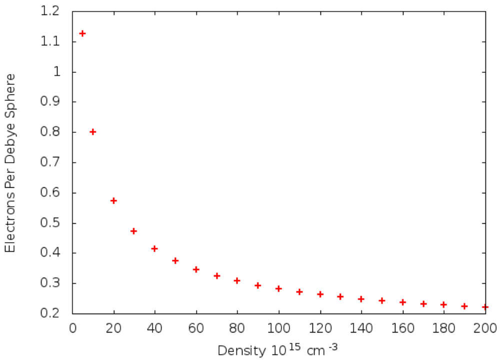

Figure 2.1: The number of electrons per Debye Sphere, against impurity density. For the Debye approximation to be valid we would expect this to be much greater than one, which it clearly isn't. This will impact the reliability of this screening approach. An alternative is outlined in Chapter 5. It should be noted that this is likely to result in an underestimation of the screening length, and hence an underestimation in the impact of electron-electron interactions.

2.3.2 Electron-Electron Scattering

The electron-electron scattering is, to first order, the same as the scattering of ionised impurities[4], in practise the form of the scattering rate and the bias in the scattering angle are the same but the exact values of the parameters differs as both particles can be moving in the laboratory frame. It is useful to define the closing velocity, v_c, as the difference between the velocities of the two particles and to use the energy in the centre of mass reference frame and the reduced mass ($m = \frac{m_1 m_2}{m1+m2}$, here $m_1 = m_2 = m_e^*$) instead of the electron mass.

2.3.3 Scattering From a Yukawa type potential

For the assumption of a Yukawa potential we can derive the scattering rate, and resultant angular distribution. Given the general potential of the form,

---

[4] As noted in the Born Approximation, the scattering only depends on the magnitude not the sign of the potential

$$V(r) = g\frac{\exp(-\lambda r)}{r}, \tag{2.31}$$

where $g = \frac{q_1 q_2}{4\pi\epsilon_0\epsilon_r}$, λ is the screening length and r is the distance between the two particles. We wish to find

$$f(\theta) = -\frac{1}{d}\int_0^\infty V(r\prime)\sin(r\prime)\,dr\prime, \tag{2.32}$$

where $f(\theta) = V_{kk\prime}$ and $d = 2k\sin\frac{\theta}{2}$. Integrating gives

$$f(\theta) = -\frac{2mg}{\hbar^2(\lambda^2 + d^2)}. \tag{2.33}$$

Producing an overall scattering rate of

$$\frac{d\sigma}{d\Omega} = \frac{4mg^2}{\hbar^4(\lambda^2 + d^2)^2}, \tag{2.34}$$

which is the well known result for scattering of the Yukawa potential [61].

2.3.4 Phonon Scattering

GaAs at finite temperature has two notable phonon types, leading to two distinct scattering events. The first, polar optical phonons account for the heat transfer between the lattice and the carriers. The second type, acoustic phonons scatter elastically[5] with the carrier population and as such are not responsible for thermalisation. Here we assume that the phonons are well thermalised and as such obey the Bose-Einstein [63] distribution, that is

$$f_{B-E}(E) = \frac{1}{e^{\left(\frac{E-\mu}{k_B T}\right)-1}}. \tag{2.35}$$

---

[5] Any non elasticity is only significant at low temperatures, less than 100 K [62]

For phonons the energy is $E = \hbar\omega_q$ so the expression becomes

$$\frac{1}{N_0(\omega_q)} = e^{\left(\frac{\hbar\omega_q}{k_B T}\right)} - 1, \tag{2.36}$$

as the chemical potential, μ, is zero.

Polar Optical Phonons

Polar optical phonons (POP) are the most important phonon scattering as they are responsible for the thermalisation of the electron population [64]. Thermalisation occurs by the electron population absorbing and emitting polar optical phonons, in thermal equilibrium the emission and absorption rates are equal, even in the presence of other thermalising interactions, in accordance with the principle of detailed balance [65]. By using the Born approximation it can be shown that the scattering rates are [64]

$$\Gamma_{abs}(E) = C\frac{N}{\sqrt{E}} \ln\left(\frac{\sqrt{E + \hbar\omega_{POP}} + \sqrt{E}}{\sqrt{E + \hbar\omega_{POP}} - \sqrt{E}}\right), \tag{2.37}$$

$$\Gamma_{emi}(E) = C\frac{N+1}{\sqrt{E}} \ln\left(\frac{\sqrt{E - \hbar\omega_{POP}} + \sqrt{E}}{-\sqrt{E - \hbar\omega_{POP}} + \sqrt{E}}\right), \tag{2.38}$$

for the absorption and emission processes. C is defined as

$$C = \frac{\sqrt{m^*}e^2\omega_{POP}}{16\sqrt{2}\pi^2\epsilon_0\hbar}\left(\frac{1}{\epsilon_\infty} - \frac{1}{\epsilon_b}\right). \tag{2.39}$$

The POP scattering is not uniform in the angle to the unscattered motion (θ) and the angle can be chosen using the non uniformity

$$\cos(\theta) = \frac{1 + \delta - (1 + 2\delta)^r}{\delta}, \tag{2.40}$$

where r is a uniformly chosen random number in the range $[0,1)$ and

$$\delta = \frac{2\sqrt{(E \pm \hbar\omega_{POP})}}{\left(\sqrt{E} - \sqrt{(\pm\hbar\omega_{POP})}\right)^2}, \tag{2.41}$$

where + and − refer to the absorption and emission of polar optical phonons respectively [64].

Acoustic Phonons

For acoustic phonons the interaction is nearly perfectly elastic and as such there is only one type of acoustic phonon event. Making use of the known distribution of acoustic phonons and assuming a parabolic band for the electrons we get [64]

$$\Gamma_{ac}(E) = \frac{\sqrt{2\left(m^*\right)^3} k_B T \mathcal{E}_1^2}{\pi\hbar^4 v_s^2 \rho_m}\sqrt{E}. \tag{2.42}$$

It should be noted that this mechanism has an unbounded scattering rate for high energy. To handle this we implement a maximum energy of thirty times the thermal energy; any instances of a particle exceeding this energy are recorded and output as a warning on the reliability of the code, such occurrences are extremely rare (occurring in less than 1% of all stable runs, in which the initial energy of the particles is equal to or less than the phonon thermal energy).

2.4 Deterministic Motion

2.4.1 Momentum Evolution

Velocity Verlet Algorithm

To carry out the momentum and position evolution we use the velocity Verlet algorithm. For notational simplicity here we treat the system as having one position degree of freedom, x, but the method is trivially generalised to the full 3D system. Starting with Newton's equation of motion

$$\frac{d^2x}{dt^2} = \frac{F(x)}{m}. \tag{2.43}$$

We can define $f(x) = \frac{F(x)}{m}$ and using a time step Δt, let

$$t_n = n\Delta t, \tag{2.44}$$

$$x_n = x(t_n) \tag{2.45}$$

and

$$v_n = \frac{dx_n}{dt}. \tag{2.46}$$

The Verlet algorithm is a centred difference method and uses the approximations that

$$\frac{dx}{dt} = \frac{(x_{n+1} - x_n - 1)}{2\Delta t}, \tag{2.47}$$

and

$$\frac{d^2x}{dt^2} = \frac{(x_{n+1} + x_{n-1}) - 2x_n}{2\Delta t}. \tag{2.48}$$

This allows us to write

$$x_{n+1} = 2x_n - x_{n-1} + (\Delta t)^2 f(x_n). \tag{2.49}$$

This can be solved iteratively, unfortunately this method does not give us easy access to the instantaneous velocity. It can be obtained but only after the fact, as the method does not explicitly calculate the velocity at each time step. As we need the velocity to calculate the scattering rates we have to use the (mathematically equivalent) modified velocity Verlet scheme [66]

$$x_{n+1} = x_n + \Delta t \left(v_n + \Delta t \frac{f(x_n)}{2} \right) \tag{2.50}$$

and

$$v_{n+1} = v_n + \frac{\Delta t \left(f(x_{n+1} + f x_n \right)}{2}. \tag{2.51}$$

An additional advantage of this scheme is that it is self starting, that is we only need the values of x_n and v_n to calculate the values at the next step. This in turn means that it is very robust to the effects of any scattering, which induces abrupt changes in the velocity.

2.4.2 Spin Evolution

The electron spins undergo Larmor precession around the effective field [7]. This precession has a frequency of $\omega = \gamma H_{eff}$, where γ is the gyromagnetic ratio and H_{eff} is the effective field. This field may have a number of origins including externally applied fields, interactions with a magnetic site and the velocity dependent spin-orbit interaction i.e.

$$H_{eff} = H_{applied} + H_{Dresselhaus} + \ldots. \tag{2.52}$$

The precession around different fields, drives the spin depolarisation of the electron population, as overtime the spins come to have randomised spins due to precessing around different fields. As such the most important terms in determining the spin depolarisation are those that vary from electron to electron. An applied magnetic field (that does not vary dramatically spatially) should make little difference as each electron would precess in the same way. As such the spin-orbit interaction is the most important driver of spin depolarisation as each particle will experience a different effective field, due to having very different velocities. The implementation of this precession is detailed in Chapter 3.

Dresselhaus Interaction

The Dresselhaus mechanism is the dominant spin orbit coupling in III-V compound semiconductors, such as GaAs. It arises due to the lack of crystallographic inversion symmetry in the material. The complete derivation is beyond the scope of this work[6] but an outline of the method is given here.

Consider the Pauli equation for a single electron in a crystal lattice

$$\left[\frac{\vec{p}^2}{2m} + V_l - \frac{e\hbar}{4m^2c^2}\left(\nabla V \times \vec{p}\right) \cdot \vec{\sigma}\right][\Psi] = E(\Psi), \tag{2.53}$$

where V_l is the lattice potential arising from the electrostatic potential. Since the lattice potential is periodic the wavefunction should have a Bloch form, that is

$$\Psi = e^{ik \cdot r}\left(u_k\left(r\right)\right). \tag{2.54}$$

By making use of a number of group theoretical results and assuming the

---

[6] Readers are directed to the complete derivation by Dresselhaus [36]

p_x,p_y and p_z commute, it can be shown that the lack of inversion symmetry results is a spin-orbit interaction [36] of

$$H_D = a_{42}\sigma \cdot \kappa, \tag{2.55}$$

where

$$\kappa_x = \frac{1}{\hbar^3}\left[p_x\left(p_y^2 - p_z^2\right)\right], \tag{2.56}$$

$$\kappa_y = \frac{1}{\hbar^3}\left[p_y\left(p_z^2 - p_x^2\right)\right], \tag{2.57}$$

$$\kappa_z = \frac{1}{\hbar^3}\left[p_z\left(p_x^2 - p_y^2\right)\right], \tag{2.58}$$

where x, y, z are the principle crystallographic directions [7]. Some care is needed in handling the strength of the interaction (the a_{42} term), as number of experimental [67] and theoretical studies [68] have been conducted to find the correct value for this term with a wide variety of results, ranging typically from 8.5 to 35 eVÅ^3. In order to obtain a reasonable result we fit our value of a_{42} by determining the low density depolarisation time and comparing to experimental data in this limit, more details in the next chapter.

2.5 Experimental Results

Throughout this work we compare our results to experiments carried out by Oertel, Hübner and Oestreich [69]. In particular we compare to the experimental results of the variation of the depolarisation time against density (See Figure 2.2) and temperature (See Figure 2.3), the figures are included

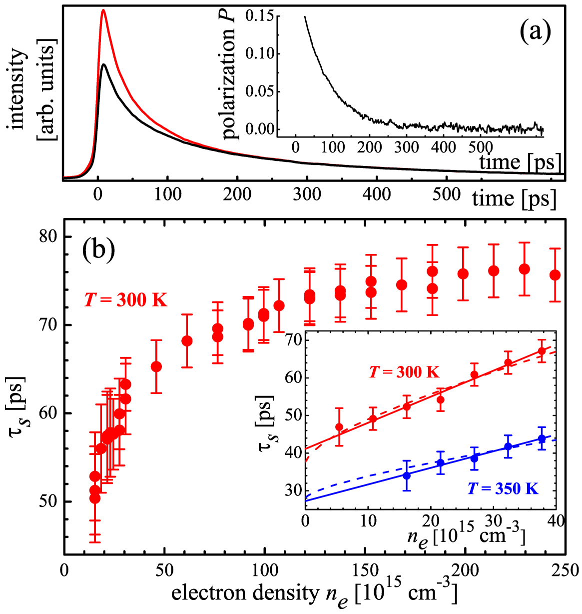

Figure 2.2: The first figure from [69]. This shows the variation of the depolarisation time with impurity density. Comparison to this figure is used in Chapters 3, 4 & 5, as a test of the validity of our simulation. As we have a free parameter (the spin-orbit strength) we also use this figure to determine the correct value of the spin orbit parameter, a_{42}. Reprinted with permission from "High temperature electron spin relaxation in bulk GaAs" [69]

here for completeness[7]. The comparison to the experimental results is of particular significance in Chapters 4 and 5, where we show that for lower densities, a basic scattering approach adequately reproduces the experimental system (Chapter 4), but for higher densities a more detailed model is needed (Chapter 5).

2.6 GaAs material properties

In our simulations throughout our work we use the following values for the material constants in GaAs [70].

v_s is the longitudinal sound velocity, a is the lattice constant. ω_{LO} value

---

[7] Reprinted with permission from "High temperature electron spin relaxation in bulk GaAs" [69]. Copyright 2008, AIP Publishing LLC

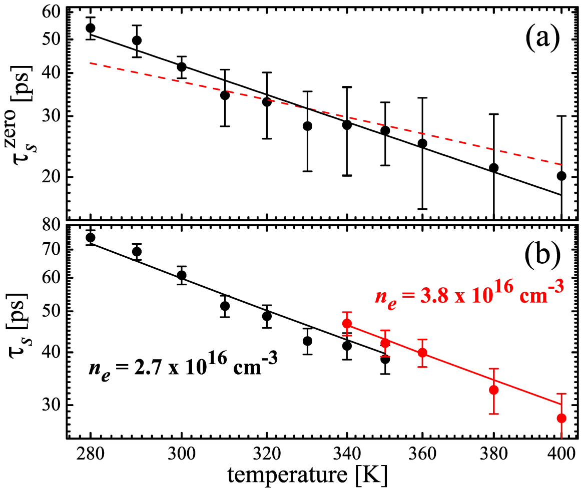

Figure 2.3: The second figure from [69]. This shows the variation of the depolarisation time with electron temperature. The simulation data is compared to this figure in Chapter 4, as part of the analysis of the basic model of electron-electron scattering presented in Chapter 3. Reprinted with permission from "High temperature electron spin relaxation in bulk GaAs" [69]

GaAs Parameters	**Experimental Values**
$\mathcal{E}_1\ (eV)$	7.0
ϵ_b	12.90
ϵ_∞	10.92
$\rho_m\ (Kg/m^3)$	5.36×10^3
$v_s\ (cm/s)$	5.24×10^5
$a\ (\mathring{A})$	5.6533
$\omega_{LO}\ (Thz)$	53.7139
ω_{LO}/ω_{T0}	1.07
E_g(eV)	1.519
$E_g^X\ (eV)$	1.981
$E_g^L\ (eV)$	1.815
$\Delta_{so}\ (eV)$	0.341
$\alpha\ (eV)^{-1}$	0.61
m/m_e	0.067
$m_e\ (Kg)$	9.1×10^{-31}

Table 2.1: Bulk GaAs Parameters

holds for the long wavelength limit. m is the electron effective mass at the bottom of Γ valley. The energy gaps are measured at $T = 300$ K.

2.7 Statistical Terms

Throughout this work we use a number of statistical terms (See Table 2.2), they are included here with formula and a description of the quantity they define [71] for completeness. The terms are calculated from one or more data sets with N elements, donated x_i and y_i, any summation is over the entire set. Sets denoted with a capital i.e. X_i, are sorted numerically in ascending order.

Term	**Explanation**	**Mathematical Definition**
Mean	A measure of the typical, or average, value	$\mu = \frac{\sum x}{N}$
Mode	The most common value in the data set	
Median	The central value	$X_{\frac{N}{2}}$ or $\frac{1}{2}\left(X_{\frac{N-1}{2}} + X_{\frac{N+1}{2}}\right)$
Standard Deviation	The spread of the data	$\sigma = \sqrt{\frac{\sum x^2}{N} - \mu^2}$
Standard Error	The typical error in the calculation of the value of the mean	$\frac{\sigma}{\sqrt{N}}$
Skewness	The extent to which the data is likely to fall above, or below the mean	$\sum \left(\frac{x-\mu}{\sigma}\right)^3$
Kurtosis	A measure of 'peakedness' of the distribution	$\sum \frac{(x-\mu)^4}{\sigma^2} - 3$
Pearson's Product Moment Correlation Coefficient	A measure of the linear correlation of two data sets	$\frac{\sum(x_i-\mu_x)(y_i-\mu_y)}{\sigma_x\sigma_y}$

Table 2.2: Statistical Terms

It should be noted here that the definition given for the kurtosis is strictly the excess kurtosis, the measure behaves the most reasonably of the various measures of kurtosis, the subtraction can be considered a correction to ensure the normal distribution has a kurtosis of zero, a property that is useful for multivariate calculations.

2.8 Conclusion

In this chapter we have discussed the ensemble Monte Carlo to technique, to summarise each electron is treated as behaving classically in any applied field plus scattering mechanisms that introduce some of the quantum mechanics(See Figure 2.4). The probability of scattering for each particle at any given time depends on its momentum, to make calculation easier we introduce the concept of "self scattering". self scattering is not a real process and is simply the result of us assuming that the scattering rate is always

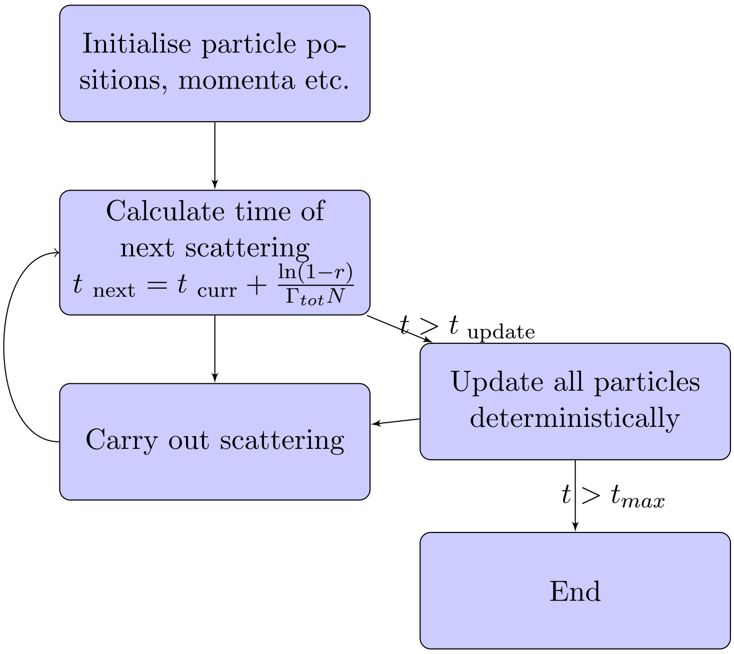

Figure 2.4: General Method Flowchart. Note r is a uniform random number in the range $[0, 1)$ using $1 - r$ instead of r allows the calculation of $\ln(r)$ for all possible r.

the maximum possible scattering rate (See Figure 2.5). As a result each particle has the same chance of scattering at any given time with the time from one scattering to the next being given by a simple exponential decay. When a particle is chosen for scattering we evaluate its real scattering rate of scattering based on the momentum of the particle and scatter it with a probability equal to the ratio of the actual scattering rate to the assumed maximum scattering rate. During scattering the momentum of the particle scattered is updated. At frequent time steps we also update the momentum of the particles, using the velocity Verlet technique and the spin part of the electron wavefunction (using a method described in the next chapter).

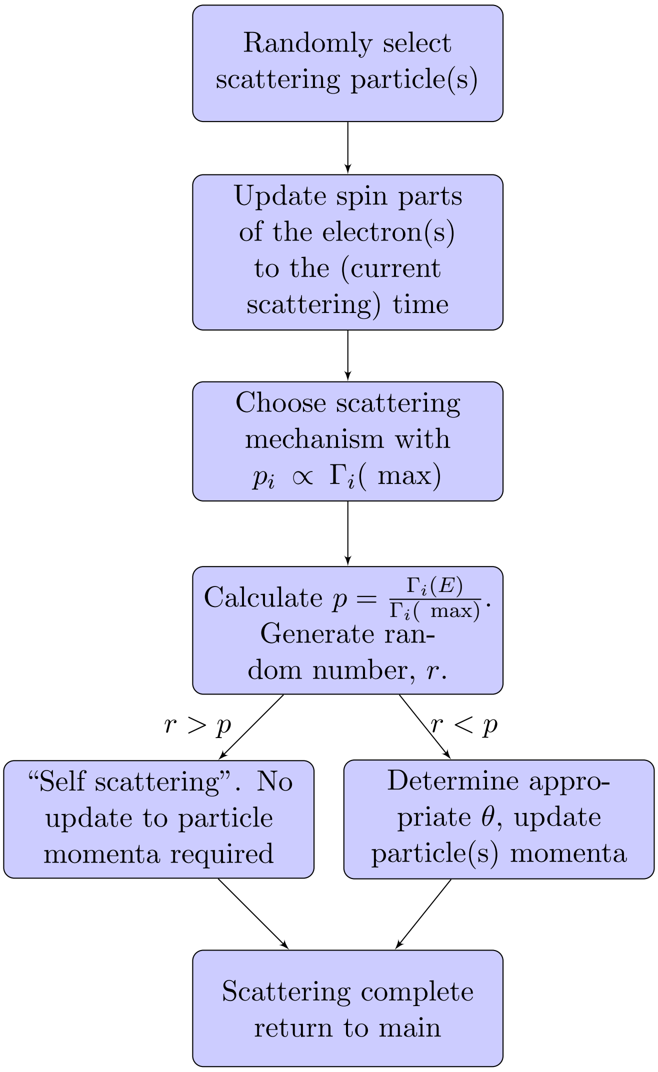

Figure 2.5: The process for carrying out scattering. The nature of "self scattering" allows us to assume at all times that $\Gamma = \Gamma_{max}$. This allows us to generate the next time of scattering without evaluating the actual scattering rate for each electron.

Scattering Type	**Scattering Rate**
POP (emission)	$\Gamma_{emi}(E) = C\frac{N+1}{\sqrt{E}}\ln\left(\frac{\sqrt{E-\hbar\omega_{POP}}+\sqrt{E}}{-\sqrt{E-\hbar\omega_{POP}}+\sqrt{E}}\right)$
POP (absorption)	$\Gamma_{abs}(E) = C\frac{N}{\sqrt{E}}\ln\left(\frac{\sqrt{E+\hbar\omega_{POP}}+\sqrt{E}}{\sqrt{E+\hbar\omega_{POP}}-\sqrt{E}}\right)$
Acoustic Phonons	$\Gamma_{ac}(E) = \frac{\sqrt{2(m^*)^3}k_B T\mathcal{E}_1^2}{\pi\hbar^4 v_s^2\rho_m}\sqrt{E}$
Ionised impurity scattering	$\Gamma_{ei}(E) = \frac{4\sqrt{2}\pi n_e e^4}{(4\pi\varepsilon)^2\sqrt{m^*}E_\beta^2}\frac{\sqrt{E}}{1+4E/E_\beta}$
Electron-Electron	$\Gamma_{ee}(E) = \frac{4\sqrt{2}\pi n_e e^4}{(4\pi\varepsilon)^2\sqrt{\frac{m^*}{2}}E_\beta^2}\frac{\sqrt{E}}{1+4E/E_\beta}$

Table 2.3: Scattering rates in GaAs

2.8.1 Scattering Rates

The important scattering mechanisms in n-doped Gallium Arsenide, in the absence of a strong applied field, are polar optical phonon (absorption and emission), acoustic phonon scattering, doping impurity scattering and electron-electron scattering. For completion the relevant scattering rates, shown earlier, are reproduced here (See Table 2.2).

Note that for the electron-electron scattering the energy and momentum are calculated in the centre of mass of the two electrons.

This technique allows us to study the dynamics of a large number of particles whilst still retaining sufficient detail of each individual particle to produce accurate results. We consider in Gallium Arsenide the important scattering mechanisms to be polar optical phonon scattering (both absorption and emission), acoustic phonon scattering (which we treat elastically), ionized impurity scattering and electron-electron scattering (more detail on how electron-electron scattering is dealt with in the next chapter). The electron spin's are assumed to feel a spin-orbit interaction from the Gallium Arsenide lattice, which is described by the Dresselhaus field. This field varies due to electron momentum and as such is responsible for the spin depolarisation and dephasing (both discussed in detail in later chapters).

Chapter 3

Model Novelties and Verification

3.1 Introduction

This chapter consists of two key parts, firstly it details some of the specific numeric and computational approaches required to implement the method described in Chapter 2 and secondly it shows verification that the model behaves as described, by showing that the model behaves in a physically reasonable way, in particular confirmation that the model correctly thermalises the electron population.

The novel aspects of our model section addresses three key points, firstly the introduction of the electron-electron scattering as a local phenomenon. Here we are making a distinction between the local scattering of electrons off one another and the long range collective behaviour [7], which could be included in a Poisson type manner[1]. Secondly we introduce an alternative numerical integration step for the spin part of the electron wavefunction,

---

[1] Chapter 5 does detail an approach to treat the full classical electrostatic electron-electron and electron-impurity interactions.

and finally we discuss methods of calculating the time taken for the electron spin polarisation to decay.

3.2 Novel Aspects of our model

3.2.1 Localised Electron-Electron Scattering

The scattering approach taken throughout this work is derived using a plane wave basis set, as such they give no information about the local nature of the scattering. From classical considerations would not expect the scattering to happen notably over an unlimited range, or at least very long ranges should contribute relatively little. As we cannot be certain of the exact nature of the distance dependence of the scattering rate we introduce an arbitrary limit to the scattering distance. Here we choose the screening length as the most appropriate distance, however adjusting the distance makes little difference to the overall properties, provided that the distance is not too short that electron-electron scattering is suppressed (see Figure 3.1).

A natural approach to allowing scattering over only particles within a certain distance would be to implement a Verlet neighbour list. In the Verlet neighbour list we start by compiling a list for each particle of the other particles within some distance [72]. This distance, the so called “halo” must be greater (often much greater) than the maximum distance of any interaction. Once the list is built we can treat the interactions only between those particles in each others neighbour lists. We have to update the neighbour lists when a particle has travelled far enough to move from outside the list to within the interaction distance. Performance is optimised by a suitable choice of the halo distance such that the number of particles is small whilst ensuring that updates to the lists are rare. This method is good if the updating to the lists, for N particles, (which is $\mathcal{O}(N^2)$) is much rarer than reading the lists, and can be optimised by careful choice of the halo be at best $\mathcal{O}(N^{\frac{5}{3}})$ [72]. In our case though the typical distance an electron travels between electron-electron scatterings is comparable to, and may even exceed, the screening length.

To more efficiently treat the localised electron-electron system we create a grid, with size equal to the maximum distance of scattering. Each site in the grid contains a doubly linked list of particles in the grid site. The number of potential scattering events for each grid (calculated as the number of particles in the grid multiplied by the sum of all particles in it and all neighbouring grid sites) is then calculated for each grid site (See Figure 3.2).

When a scattering event is determined to occur we select a random grid weighted by the number of potential scattering events for that grid site. Once a grid is chosen we then choose the two particles involved in the scattering, one from the grid site itself and one chosen uniformly from the remaining particles in that grid site and all neighbouring grid sites. If the distance between the two particles is less then the screening length we accept the two particles and continue with the scattering event, otherwise we start the process again choosing a new random grid.

Performance Notes - Choice of grid site

The naive solutions to the choice of grid perform poorly as the number of particles in each grid fluctuates rapidly. For example we may make a cumulative summation of the total number of possible events for the grid sites in some order. We could then generate a random number up to the total for all grids and efficiently select the correct grid (in $\mathcal{O}(\log N)$ [73] time, by implementation of a skip list), however the setting up of the cumulative

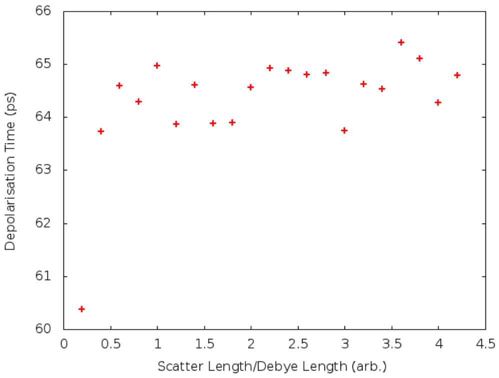

Figure 3.1: The depolarisation time depends on the maximum distance allowed for electron-electron scattering. Around the Debye length it appears to only be weakly dependant, although as we go to significantly lower scattering lengths we suppress the scattering rate as particles able to do scattering can become quite rare, causing a drop in the depolarisation time. Here we use averages of five runs of 50,000 particles with $n = 50 \times 10^{15}$ cm^{-3} and $T = 300$ K.

summation is an $\mathcal{O}(N)$ operation, worse the typical time between required updates is proportional to the number of grid sites, making the overall algorithm $\mathcal{O}(N^2 \log N)$

We instead implement an alternative approach by maintaining the largest weighting of any grid. To choose the suitable grid we randomly select a non empty grid site, and choose to keep it with a probability of $\frac{M}{M_{max}}$ where M is the number of particles in the grid, and M_{max} is the largest such value at the current time in the simulation. This overall requires $\mathcal{O}(\frac{M_{max}}{M})$ iterations, which is very weakly, although non trivially, dependent on N (See Figure 3.3). As a result overall the choice of a site is almost independent of N, though of course the number of scattering events scales linearly with N.

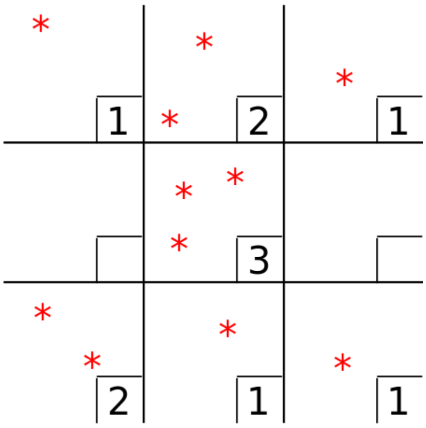

Figure 3.2: A 2D representation of our grid. Each grid site contains a number of particles. The weighting for each grid is $W = M(M + A - 1)$, where M is the number of particles in the grid and A is the number in neighbouring grid sites; for the middle grid in the above figure the weighting is $3 \times (7 + 3 - 1) = 27$. This represents the number of possible pairings any particle in our grid could have, including pairings with nearest neighbour boxes.

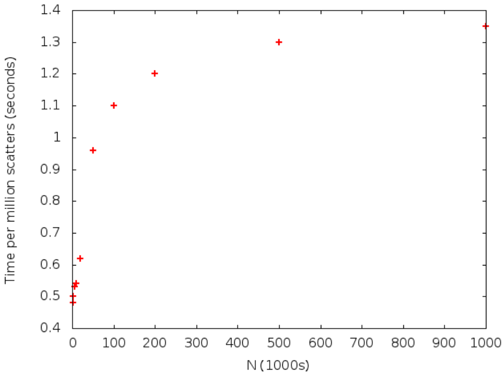

Figure 3.3: The computational cost of a single electron-electron event is not entirely independent of N. For large N it appears to converge to a limiting value.

Comparison to other methods of handling the electron-electron interaction

In general other simulations have tended to ignore the issue of electron-electron scattering, this has been justified (when the charge transport properties are of interest) by the statement that as the electron electron scattering conserves momentum and total energy it cannot impact the important measures of the performance of a device, such as the mobility. In spintronics systems where the rate of scattering strongly impacts the performance of a device we certainly do not have that luxury and some attempt to include electron-electron scattering has been required, however it has generally been poorly treated. The major difficulty is in a method for choosing appropriate pairs of particles, which in practice usually has meant that a single particle is chosen as a primary scatterer and then a second particle is chosen. Here we briefly outline a few of the alternative approaches to choosing that particle, and the reasons we have for discarding them.

- Electron chosen from local slice. This method, used in the previous group model [74], splits the electrons into slices in one dimension. Electron-electron scattering then happens within pairs of electrons within the same slice, regardless of the distance between them. This has a number of disadvantages, in that the apparent temperature in neighbouring slices can drift significantly as the only thermal contact is by the movement of electrons between them. It also has difficulties with scattering between electrons a long distance apart in two directions provided they are close enough in one direction.
- Electron chosen from thermal distribution [41]. In this method instead of choosing a real second particle the relevant properties of the elec-

tron are chosen from a thermal distribution, this method is extremely efficient but results in the electron-electron scattering not conserving momentum or energy, this causes the total energy to vary more than would be usually expected and can be difficult to implement if the device is not in thermal equilibrium.

- Electron chosen from all electrons [7]. This method functions much like the above, with only one electron actually having its statistics updated, however instead of choosing from the ideal thermal distribution the second electron is simply a randomly chosen electron from the entire population. As only one particle is altered this still does not conserve momentum or energy, and cannot handle any temperature gradient within the device. It can perform better than a particle chosen simply from the thermal distribution though, as it can handle situations such as laser heating applied to the entire device, or an electron population in thermal equilibrium at an unknown temperature (perhaps in response to the lattice being heated). This method is the least troubling of all the alternatives to the method we propose and as such the impact of it is briefly studied in Chapter 4 (Section 4.6).

In addition to scattering approaches to the electron-electron interaction we can also consider non scattering based approaches. In Chapter 5 (Section 5.3) we investigate the impact of replacing the electron-electron scattering (and the electron-impurity scattering) with the interaction due to the Coulomb forces, this approach is significantly better performing over a wider range of densities but has significantly poorer performance.

In comparison to the above methods our approach has all the benefits of the first choice, conservation of momentum and energy, with none of the drawbacks (no artificial imposition of a one dimensionality, no cut off between areas), despite this the abrupt change between areas within one screening length (that can all scatter with equal probability) and those outside it (which can't scatter at all) is unrealistic and further work should be undertaken to better attempt to improve the model, perhaps with a scattering rate that decayed the further apart the electrons are.

3.2.2 Spin Evolution

The spin part of the electron wavefunction can be evolved in a number of ways, here we show the Crank-Nicolson approach to be superior to the more commonly used Heun scheme for time evolution of the spin part of the electron wavefunction. The Heun scheme, used extensively in atomistic magnetic simulations and an alternative derived using the Crank-Nicolson approximation to Schroedinger Equation.

The Heun scheme is a predictor-corrector method, correct to second order, which requires two renormalisations of the spin per time step. The scheme is,

$$\tilde{y}_{i+1} = y_i + \Delta t f(t_i, y_i), \tag{3.1}$$

$$y_{i+1} = y_i + \frac{\Delta t}{2} \left(f(t_i, y_i) + f(t_i, \tilde{y}_i) \right). \tag{3.2}$$

Renormalising, immediately after calculation of $\tilde{y}_{i+1}$ and y_{i+1} [75]. The Crank-Nicolson scheme is a general scheme often used for the time evolution of the Schroedinger equation, if we start with the Schroedinger equation

$$\hat{H}\left(t\right)\Psi(t) = i\hbar\frac{\partial\Psi(t)}{\partial t}, \tag{3.3}$$

then rearranging we have

$$\Psi(t) = e^{\frac{iH\hat{(t)}t}{\hbar}}\Psi(0). \tag{3.4}$$

We can expand the exponential in two ways, by use of a Maclaurian expansion;

$$\Psi(t = \Delta t) \approx \left(1 - \frac{i\Delta t}{\hbar}\hat{H} - \left(\frac{\Delta t}{\hbar}\hat{H}\right)^2\right)\Psi(t = 0), \tag{3.5}$$

where 1 is the Identity matrix, and (by replacing Δt with $-\Delta t$)

$$\left(1 + \frac{i\Delta t}{\hbar}\hat{H} - \left(\frac{\Delta t}{\hbar}\hat{H}\right)^2\right)\Psi(t = \Delta t) \approx \Psi(t = 0). \tag{3.6}$$

These two forms can be combined to get the Crank Nicolson Scheme [76],

$$\Psi(t = 2\Delta t) = \left(1 + \frac{i\Delta t\hat{H}}{\hbar}\right)^{-1}\left(1 - \frac{i\Delta t\hat{H}}{\hbar}\right)\Psi(t = 0), \tag{3.7}$$

or by considering the time step to be half the length above

$$\Psi(t = \Delta t) = \left(1 + \frac{i\Delta t\hat{H}}{2\hbar}\right)^{-1}\left(1 - \frac{i\Delta t\hat{H}}{2\hbar}\right)\Psi(t = 0) + \mathcal{O}\left(n^3\right). \tag{3.8}$$

This scheme is correct to third order and conserves probability. Normally it requires the computationally expensive matrix inversion, however in this case we are solving for each electron spin independently we know that our Hamiltonian is only a two by two matrix, so the inversion and multiplication can be done analytically. We treat each electron as behaving independently, which reduces the wavefunction to a complex vector of order 2.

With an effective field $h_x\hat{x} + h_y\hat{y} + h_z\hat{z}$, we have a Hamiltonian of

$$H = \mu \begin{pmatrix} -h_z & h_x + ih_y \\ h_x - ih_y & h_z \end{pmatrix}, \tag{3.9}$$

where μ is the gyromagnetic ratio of the particle.

The inverse of first term of the Crank-Nicolson scheme then is trivially [77]

$$\left(1 + i\gamma\hat{H}\right)^{-1} = \frac{1}{h_x^2 + h_y^2 + h_z^2} \begin{pmatrix} 1 - i\gamma h_z & \gamma(ih_x - h_y) \\ \gamma(ih_x + h_y) & 1 + i\gamma h_z \end{pmatrix}, \tag{3.10}$$

where $\gamma = \frac{\mu\Delta t}{2\hbar}$.

This gives a final scheme of

$$\Psi(t = \Delta t) = \frac{1}{h_x^2 + h_y^2 + h_z^2} \begin{pmatrix} 1 - i\gamma h_z & \gamma(ih_x - h_y) \\ \gamma(ih_x + h_y) & 1 + i\gamma h_z \end{pmatrix} \Psi(t = 0). \tag{3.11}$$

Compared to the Heun scheme this has a number of advantages. Firstly it implicitly conserves length and energy, removing the need for the costly renormalisation steps that are present in the Heun scheme due to it not conserving spin length. The result is that per time step this approach runs between 50% and 75% faster. The conservation of energy prevents the spurious damping to, or anti-parallel to, the applied field, seen in other schemes. Secondly the Crank-Nicolson approach is a third order approach (i.e. the error term is $\mathcal{O}\left(\Delta t^3\right)$) instead of the second order Heun, allowing larger time steps (See Figure 3.4). Finally the Heun scheme, by working on the classical projections, forces us to lose information about the relative phases.

To convert from the wavefunction to the classical projections (for example to determine the net direction and magnitude of the spins) we need to do some additional calculation. The semi-classical approach to spin evolution (such as that employed by the Landau-Lifshiftz-Gilbert technique [78]) makes use of a classically well defined direction for the spin. This idea of a well defined spin direction does have physical meaning even when considering a spin half particle. It is the direction that if we were to observe a spin, in a direction, we would be guaranteed, in principle, to find it lying in (not opposite to) that direction. The x, y and z components of the spin, for a given wavefunction, are the expectation value of each component. That is

$$m_x = 2(\mathcal{R}(\uparrow)\mathcal{R}(\downarrow) + \mathcal{I}(\uparrow)\mathcal{I}(\downarrow)), \tag{3.12}$$

$$m_y = 2(\mathcal{R}(\uparrow)\mathcal{R}(\downarrow) - \mathcal{I}(\uparrow)\mathcal{I}(\downarrow)), \tag{3.13}$$

and

$$m_z = 2(\| \uparrow \|^2) - 1, \tag{3.14}$$

where ↑ and ↓ refer to the up and down component of the spin and $\mathcal{R}$ and $\mathcal{I}$ refer to the real and imaginary component, assuming that the wavefunction is written in an s_z basis. It should be noted, however, that the Crank-Nicolson approach requires one extra double precision number per particle[2] and as such increases the memory requirements by one third.

The use of a numerical approximation, rather than solving analytically is simply required for efficiency. Due to the large number of trigonometric evaluations required to calculate the solution analytically, the Crank-Nicolson approach is more than an order of magnitude faster, essentially removing

---

[2] Needing to store two complex numbers instead of three real numbers in the Heun scheme approach, which works on m_x, m_y and m_z

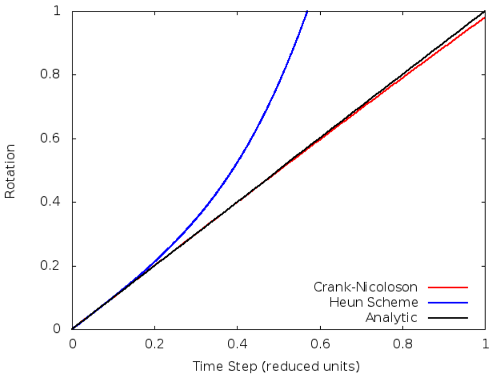

Figure 3.4: Plotting the change in angle against time step in a constant field, we would anticipate a constant rate of change of the azimuthal angle, for large time steps neither scheme is exact but the Crank-Nicolson behaves much better than the Heun scheme, even though it is quicker to calculate.

this aspect of the code from being a limiting factor in overall performance at any number of particles.

3.2.3 Calculation of the Spin Depolarisation Time

For even a relatively small number of particles (N=5,000) each depolarisation curve generally have apparently very low noise. However when considering numerous runs, only varying the seed of the random number generator, we get differences greater than the statistical error on a single depolarisation curve (Figure 3.5), this remains true over a large range of number of particles (certainly up to $N = 250,000$) This difference requires us to be careful in our handling of the error bars in our results and in the method chosen for determining the true value of the spin depolarisation time.

After an initial transient, the electronic spin polarization is observed to decay exponentially (see Figure 3.5). At low times the behaviour is different so estimates of τ that relies solely on the time for the electron spin polarisation to reach a certain value is inaccurate, as the transient time will depend on the details of the initial conditions, even so monitoring for when the spin polarisation passes a certain level (for example $S = exp(-1)$) provides a reasonable approach. There are two other reasonable approaches to take, firstly we could fit an exponential decay to the depolarisation time and secondly we can compare ratios of spin a known time apart.

Exponential Fit

If we carry out a simple least fit regression on the data for each time step, weighting each point to $\ln((S(t_i))$ (ensuring that the tail is not over-weighted), we obtain an expression for the depolarisation time, τ, of [79]

$$\frac{1}{\tau} = \frac{\sum_i^M S(t_i) \sum_i^M t_i S(t_i) ln(S(t_i)) - \sum_i^M t_i S(t_i) \sum_i^M S(t_i) ln(S(t_i))}{\sum_i^M S(t_i) \sum_i^M t^2 S(t_i) - \left(\sum_i^M S(t_i) t_i\right)^2}. \tag{3.15}$$

Ratio Method

If we instead consider the ratio of the spin at two different times (summing over all i timesteps), separated by some amount δt, we have

$$R = \frac{1}{N} \sum_i \frac{S(t)}{S(t+\delta t)}, \tag{3.16}$$

$$\tau = \frac{\delta t}{\ln R}. \tag{3.17}$$

This alternative approach is robust to a large early fluctuation (which we would expect to decay no faster than τ, and which may account for some of the difference in errors between runs compared to the expected error for a single run.

Comparison

We see in Figure 3.6 that in the high particle number limit the two methods described in the previous section are consistent. However at low particle numbers the estimates from both methods deviate from the high particle number limit. The exponential best fit deteriorates dramatically, for particle numbers less than $N = 15,000$, though this may depend on the system parameters (such as temperature or doping density). We also notice the ratio method exhibits similar problems, although less severe, notable deviation starts between 5,000 and 10,000 (See Figure 3.6).

Also for comparison the time to reach a spin state of $S = exp(-1)$ is shown. This does not appear to be affected by the number of particles but in the high limit is inaccurate by around 1 ps.

Conclusion

Care must be taken to accurately determining the spin depolarisation time from ensemble Monte Carlo simulation data. The results demonstrate that, when considering simulations with an intermediate number of electrons ($N \sim 10^4$), an estimate based on the ratios of the average spin polarisation at different times performs better than a more conventional approach. In smaller simulations the crude time to reach a given polarisation, is the best, but this does introduce a systematic error (apparent at large numbers of particles). For larger simulations ($N \sim 20,000$) there is little to choose between the exponential fit and the 'ratios' method. Throughout this thesis, unless otherwise stated, runs consist of a simulation of $25,000$ particles with repeated runs carried out averaging over the runs until the apparent standard error is less than 1% of the result, with at least 5 runs conducted.

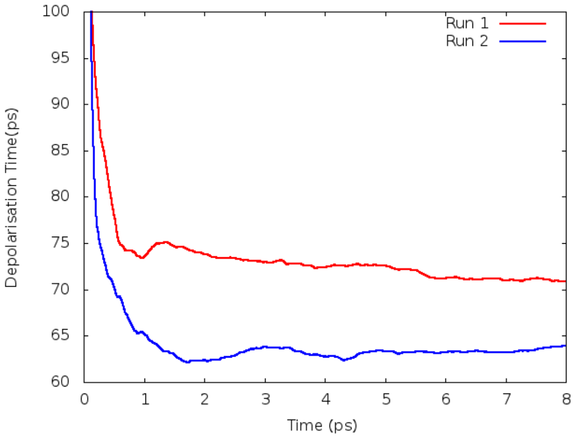

Figure 3.5: Two different runs using the same conditions but different random seeds produce depolarisation times that disagree by more than the apparent standard error in either.
The depolarisation time calculated here is calculated as $\tau = \frac{t}{\log(S)}$. Here $n = 50 \times 10^{15}$ cm^{-3}, $T = 300$ K and $a_{42} = 22$ eVÅ^3 and the runs consist of $15,000$ particles.

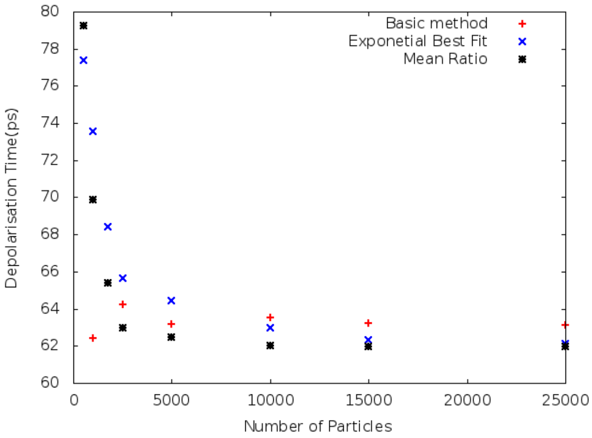

Figure 3.6: The three methods calculation of the depolarisation time is compared here. Here n=40×10^{15} cm^{-3}, T=300 K and $a_{42} =$ 22eVÅ^3. Repeated independent runs were carried out for each method until the standard error in lifetime was reduced to less than 1% of the depolarisation time.

3.2.4 Motional Narrowing and Spin Depolarisation

It is reasonable to discuss how we might go about estimating the spin depolarisation time based on the properties of the electron population, such as the typical scattering times and scattering angles. For the density and temperatures that we are interested in we are in the motional narrowing regime where the time averaged effective field, over the time scales required for depolarisation felt by individual electrons is substantially less than the instantaneous field. The time averaged field can broadly be impacted in two ways, firstly the instantaneous field can be increased (trivially for example by considering materials with different spin-orbit coupling constants), secondly increasing the scattering rate (which reduces the time averaged field as the system becomes uncorrelated over a shorter time). As a result in general the inclusion of additional scattering rates will tend to increase the rate of depolarisation unless it suppresses other scattering events or impacts the equilibrium distribution of the electron population.

If we define the time averaged field, over a time τ, to be

$$h^2\left\{\tau\right\} = \frac{1}{N_{max}} \sum_{n=1}^{N_{max}} \left(\int_{t=0}^{\tau} h_{x_i} dt\right)^2 + \left(\int_{t=0}^{\tau} h_{y_i} dt\right)^2 + \left(\int_{t=0}^{\tau} h_{z_i} dt\right)^2 . \tag{3.18}$$

We can determine how this behaves for increasing time. At short times we see a slow decay increasing in rate such that by 1 ps the decay is of the form $h\left\{\tau\right\} \propto \frac{1}{\sqrt{\tau}}$ (See Figure 3.7). This decay is in accordance with central limit theorem as doubling the length of time the system is considered over doubles the number of essentially independent data points, this suggests that at this time scale each individual electron can be considered to be uncorrelated with the other electrons, feeling a field that is roughly Gaussian and not showing strong time correlation. As this time scale is significantly

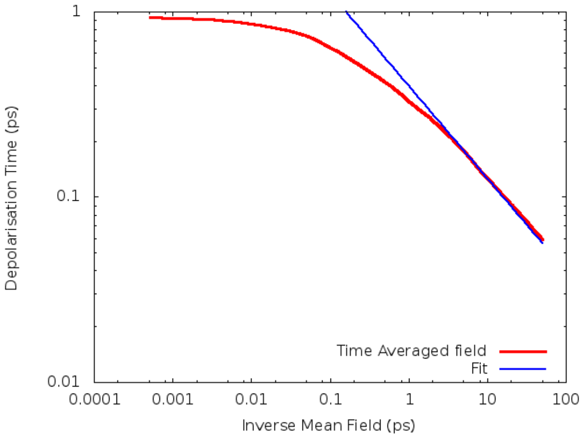

Figure 3.7: The normalised applied field decays, by around one picosecond the decay is close to the expected $\frac{1}{\sqrt{\tau}}$. Here $T = 300$ K, $n = 10^{17}$ cm^{-3}

less than the typically observed depolarisation time (of around 60 ps) we can conclude that the system is certainly in the motional narrowing regime.

We can use the time averaged field as an estimator of the depolarisation time of the system, here we look at the depolarisation time against the field after 10 ps, that is to say the notation used earlier $h\{10 \text{ ps}\}$. For the system to depolarise the average spin must have changed by some amount θ, at least $\frac{\pi}{2}$. The rate of change of the spin is proportional to the effective field felt allowing us to approximate the form of the dependence of the depolarisation time on the effective averaged field as

$$\alpha h\{\tau\} t = \theta. \tag{3.19}$$

For large time we know that $h\{\tau\} \propto \frac{1}{\sqrt{\tau}}$. Substituting in we have

$$\frac{B}{\sqrt{\tau}} = \theta, \tag{3.20}$$

where B is an unknown constant of proportionality. Suggesting that the depolarisation time, t, will be of the form $t = \frac{A}{h^2\{\tau\}}$ for large τ.

Results

To determine the proportionality constant we fit to the observed data. The depolarisation time is calculated by carrying out an exponential best fit to the $S(t)$ curve. Usual procedures apply for this fit we use the standard $a_{42} = 21.9$ eV$\mathring{A}^3$ with temperatures of $250, 300\&350$ K and doping densities ranging from 5 to $200 * 10^{-15}$ cm^{-3} (See Figure 3.8).

We can further extend the range of applied field values by varying the value of a_{42} over the range 5 to 45 eV$\mathring{A}^3$, without carrying out a new best fit. The trend remains in excellent agreement (See Figures 3.2.4). Additionally if we dramatically alter the method used for the electron-electron interaction to the electron-electron classical forces (the detail of this method is given in Chapter 6) we still see the same fit being accurate, again no new fit is carried out (see Figure 3.10).

Conclusion

Determination of the spin depolarisation time can be readily obtained by studying the time averaged spin field, this method appears to be the most accurate and efficient method of calculating the spin depolarisation time. The advantages include a need to only simulate a short time, a smaller number of particles needed and that the error in one run is similar to the error between runs, despite this the method is not used throughout the rest of this work as the result came too late to be used throughout the rest of the document and we lack any proof of generality of this method. This method could also be readily adapted to use using conventional transport codes that lack the ability to handle spin, as the field can easily be calculated from the

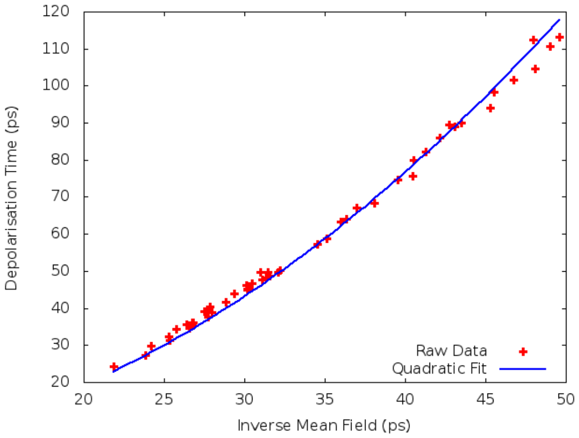

Figure 3.8: Shown is the depolarisation time for the spin system against one over the time averaged field multiplied by the gyromagnetic ratio after 10 ps. The fit shown is generated using the gnuplot nonlinear plotting library. For all other figures the fitted curve is the fit from this data only

instantaneous momenta, although the unknown constant would have to be determined using a full spin code. This method also helps make it intuitively clear that anything that increases the scattering rate, the typical scattering angle or introduces a new scattering mechanism will tend to reduce depolarisation, increasing the depolarisation time. As it will reduce the correlation time, reducing the average effective field.

3.3 Model Testing

3.3.1 Electron Thermalisation

Thermalisation is required before we can start the studies of the spin dynamics of the electron population. As we have no potential energy we expect the electron population to reach a Maxwell-Boltzmann distribution at the lattice temperature [80], that is

$$p(E)dE = 2\sqrt{\frac{E}{\pi}}\left(\frac{1}{k_BT}\right)^{\frac{3}{2}} \exp\frac{-E}{k_BT}dE, \tag{3.21}$$

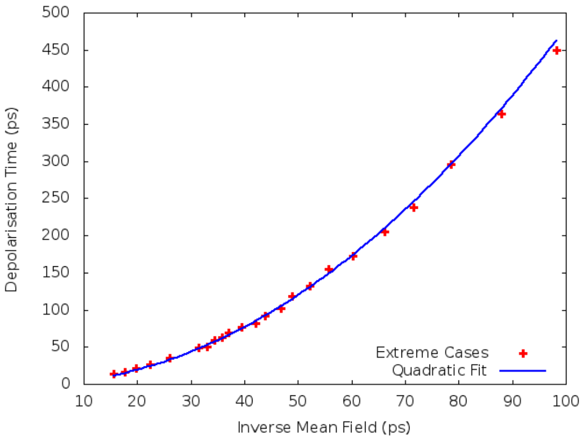

Figure 3.9: To test the reasonableness of the Quadratic fit, we extend the range of the field by artificially altering the spin orbit coupling constant, within the range routinely claimed experimentally. The fit is to the data in 3.8

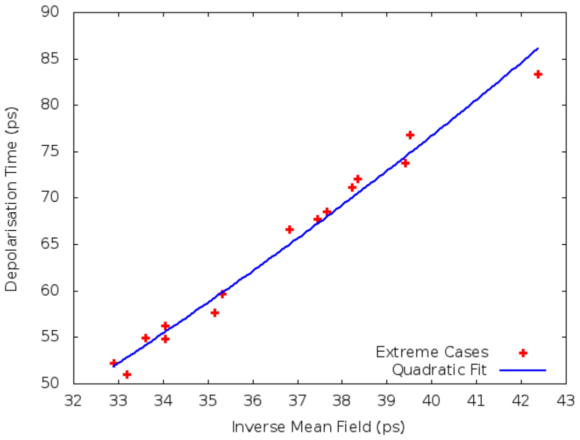

Figure 3.10: Even using a dramatically different form of method for updating the electron, the BH forces approach, we still see a strong agreement with the fit found in 3.8

where k_B is the Boltzmann constant, E is the energy and T is the lattice temperature. During the initial evolution of the system (when started out of thermal equilibrium) the system may not have the Boltzmann distribution for the correct temperature. To determine the temperature through this initial evolution we use a definition of temperature calculated by the average velocity squared of the particles as

$$T = \frac{\langle v^2 \rangle m^*}{3k_B}. \tag{3.22}$$

In the case of a Boltzmann distribution this reproduces the temperature but it is also a property that can be cheaply calculated allowing for monitoring of the temperature at each time step. In addition to the importance of the thermalisation to the correct temperature we also wish to know if the distribution is Boltzmann like. To do this we can produce a histogram of particle energies (placing them in a box with energy $E \pm \frac{1}{2}\Delta E$, at each time step, and compare the differences with the Boltzmann distribution, with the temperature calculated based on $\langle v^2 \rangle$. We calculate the mean squared of the residuals by summing over "boxes" of energy E the difference between the number of particles in that box and the statistical expectation from a Boltzmann distribution, that is

$$\langle R^2 \rangle = \sum_{i=1}^{N} \left(\frac{C(E_i)}{M\Delta E} - p(E_i) \right)^2 , \tag{3.23}$$

(where ΔE is the width of the histogram box,$C(E)$ is the number of particles within that energy 'box', i is the identifier for each box and M is the total number of particles), and use this as a measure to determine if the system is Boltzmann like. The temperature used in the calculation of the $p(E_i)$, is the temperature associated with the $\langle v^2 \rangle$, of the system which is not necessarily the lattice temperature. To determine the expected value of $\langle R^2 \rangle$ and a confidence interval [3], we also carried out this process with a set of data chosen randomly from a Boltzmann distribution. We carried out repeated tests, using the Boltzmann distribution until we had a sufficient sample (10,000 runs used) to determine what value for the residuals a sample randomly chosen from the Boltzmann distribution would be expected to have, and importantly what level 95% of all such samples would fall below. This gives us a reasonable confidence interval against which we can conduct a meaningful hypothesis test. This method is somewhat crude, as it does not consider some features of the real electron system (e.g. the particles are assumed to have uncorrelated energies), however it is sufficient to tell us if the fit is reasonable.

The thermalisation of the system happens on a relatively short time scale (taking less than 5 ps to thermalise from 130 K to 300 K (see Figure 3.11)), but the Boltzmann fit (for an arbitrary temperature) is quicker (taking around 0.5 ps) than the time taken to reach the correct temperature. The thermalisation can then be characterised as two processes, initially the system is far too cold and particles are very likely to undergo many polar optical phonon absorption scatterings, which distorts the system from the Boltzmann distribution, as the system gets closer to equilibrium the heating slows down and the electron electron scattering has enough time to ensure the particles are properly distributed (for the current temperature), during this time the system continues to heat but goes through what appear to be a series of quasi-equilibrium states, until it reaches equilibrium, with the electron temperature matching the lattice temperature.

---

[3] Enabling us to say to what extent the system appears to be Boltzmann like, and therefore to what extent it has a well defined temperature.

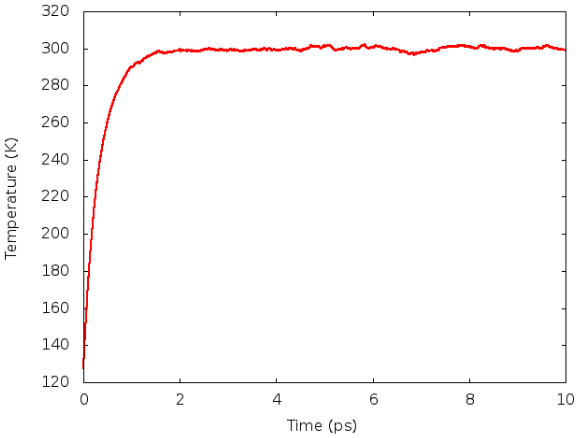

Figure 3.11: The electron population rapidly reaches the lattice temperature, as we allow a full 20 ps for all thermalisation we can have good confidence that the system reaches equilibrium. Here $n = 15 \times 10^{15}$ cm^{-3}, $T = 300$ K and $N = 25,000$.

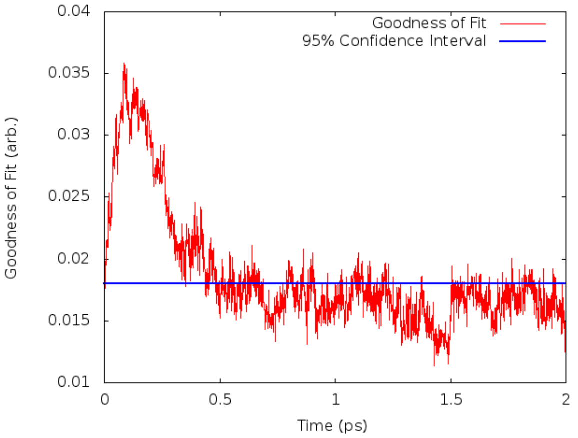

Figure 3.12: The electron population initially starts as a Boltzmann distribution, by selecting Gaussian distributions for the three components of the velocity, as it heats to the lattice temperature we see it is initially driven out of a Boltzmann distribution, before returning to a Boltzmann distribution, even though the sample has not yet reached the equilibrium temperature.$n = 15 \times 10^{15}$ cm^{-3}, $T = 300$ K and $N = 25,000$

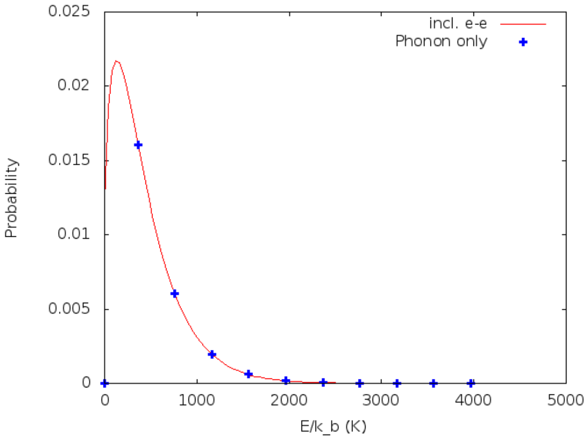

Figure 3.13: The electron population initially starts at $T = 0$ K, as the only way an electron can change energy is to absorb or emit a polar optical phonon it does not reach a smooth Boltzmann distribution, however the energies with non zero occupation match exactly with the Boltzmann distribution and with the distribution function generated from a run including electron-electron scattering. Here the lattice temperature is 300.

No electron-electron thermalisation

In the absence of electron-electron scattering each particle can only change its energy by an integer multiple of polar optical phonon energies (equivalent to around 395 K) and as such the energy distribution does not converge to a good fit of the Boltzmann distribution when we look at granularities in energy less than the polar optical phonon energy (see Figure 3.13). This is to be expected and can result in the apparent, $\langle v^2 \rangle$, measure of temperature having significant deviation from the lattice temperature. This difference is impacted solely by the initial condition, if one starts the simulation at the lattice temperature (instead of allowing it to relax to get there) it does not cause a deviation from the lattice temperature.

As we have observed that the thermalisation time is relatively short, around 5 ps seems to be more than adequate we initialise our system, in all further results, by randomly assigning our particle a velocity, choosing randomly the x,y and z components independently from a Gaussian[4]. We then allow the system to thermalise for 20 ps, so that we can be very confident that the system when we start the “experiment” is in a proper thermal equilibrium state.

---

[4] Which is equivalent to choosing the energies from a Boltzmann distribution

3.4 Conclusion

This chapter has shown how we implement the ensemble Monte Carlo method, including some of the decisions made in treating the electron-electron scattering and verified that the model does appear to be functioning correctly. In particular we showed that the Crank-Nicolson scheme is the best approach for the time evolution of the spin part of the electron wavefunction, showed an accurate way of determining the spin depolarisation time, and detailed the method for implementing a restriction on electron-electron scattering to ensure it remains local in nature. In addition we have described the procedure for the generation of all data presented throughout this Thesis, that is unless otherwise stated all results consist of $25,000$ particles with repeated runs carried out averaging over the runs until the apparent standard error is less than 1% of the result, with at least 5 runs conducted and that the electron momentum is allowed to thermalise for 20 ps before the start of any given run.

The next chapter will look in detail at the properties of the electron population, including the impact of the various scattering mechanisms on the electron population and the spin depolarisation properties at a range of densities and temperatures, particularly paying close attention to the properties near 300 K.

Chapter 4

Electronic and Spin properties of the electron "gas"

4.1 Introduction

This chapter discusses in detail the properties of the electron gas, in particular it looks at the scattering properties against density and temperature and the spin depolarisation properties also against density and temperature.

It should be noted that the basis of the model has been described in a paper (G Marchetti, M Hodgson, J McHugh, RW Chantrell and I D'Amico [81]). This model was jointly developed by Gionni Marchetti and myself. Ref [81] gives details of the underlying theoretical model development (the responsibility of Gionni Marchetti and not reproduced here); I had responsibility for the code development. The calculations and fit to experiment in [81] were carried out in full collaboration with Gionni Marchetti since the work required continuous theoretical and computational development.

The results presented here are obtained with a slightly simpler version of the model, using the Debye approximation for the screening length. However, the differences between the results presented here and in [81] are small, justifying the use of this model; the impact of the fuller calculation of the screening length is shown in Chapter 5.

This chapter starts by establishing the relative impact of the various scattering mechanisms, showing that in the low density limit we see a remnant electron-electron impact that seems to be unreasonable, in this limit we would expect that the impact of the electron electron scattering would be close to linear. It should be noted that even though we look at doping densities far below those experimentally discussed we are still significantly higher that that required for Wigner crystallisation [82], which at any rate our model cannot attempt to describe, and it is doubtful if it is relevant given the classical ground state of our system would not be a Wigner crystal but the binding of the electrons to the ionized doping impurities.

We then use our model, and experimental data, to determine the correct value of a_{42}, the spin-orbit coupling constant under a variety of system variants, when the full model is considered we show good agreement with the experimental value found by Oertel *et al.* [69]. Having shown good experimental agreement for the value of the spin orbit coupling we then go on to show a broad range of densities and temperatures under which experimental agreement remains good, however for higher densities we show a significant deviation from experiment, approaches to discuss this problem are dealt with in the next chapter.

4.2 Scattering Rates

4.2.1 Phonon Scattering

As the sole form of thermal contact with the lattice the phonon scattering plays an important role in assuring the electron population becomes properly thermalised to the lattice temperature. The total rate of polar optical phonon absorption and emission when at equilibrium should balance and is observed to be occur around every 0.9 ps per particle at 300 K, this value is independent of density but varies with temperature (see Figure 4.1). In addition the phonon scattering has a strong forwards bias, with particles more likely to be pointing in the same direction as they started after scattering while this depends on the electron energy as well as the phonon temperature the average angle scattered is a useful crude measure of this, and shows an average scattering angle of 0.15 ± 0.02 at 300 K with the effect stronger the higher the energy of the particle and the hotter the lattice.

The acoustic phonon scattering is treated as being elastic, and as such does not transfer energy from the lattice and is considerably rarer, occurring around once every 7 ps per particle at 300 K, than the POP scattering (see Figure 4.1) however as it does not contain a bias in the scattering direction it can have significant impact on the electron population.

Using these mechanisms, only, we can attempt to study the spin depolarisation of the electron population, obtaining a low density limit. This can be used to fit to experiment (where the zero density depolarisation time is know to be around 40 ps) to determine an appropriate value of a_{42}, which suggests we should use a value of $a_{42} = 14$ eVÅ^3 (see Figure 4.2).

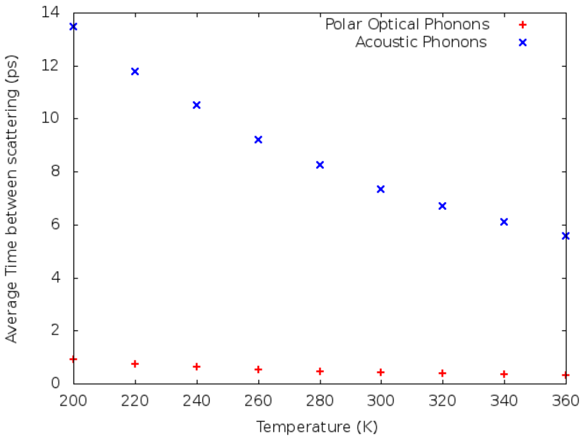

Figure 4.1: The acoustic phonons are considerably rarer than the polar optical phonons, for a broad range of temperatures

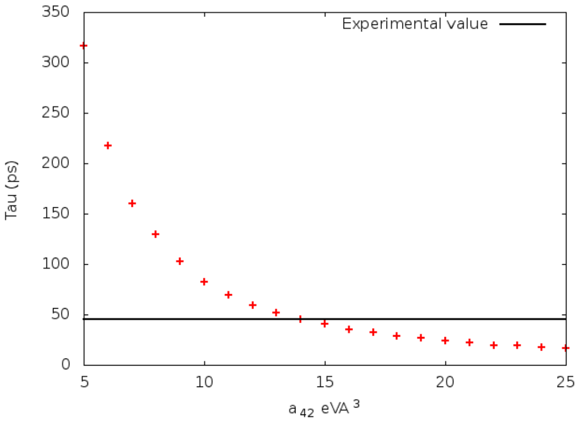

Figure 4.2: Varying the spin-orbit coupling has a strong impact on the depolarisation time, this curve implies a low density limit for a_{42} of 14 eVÅ^3

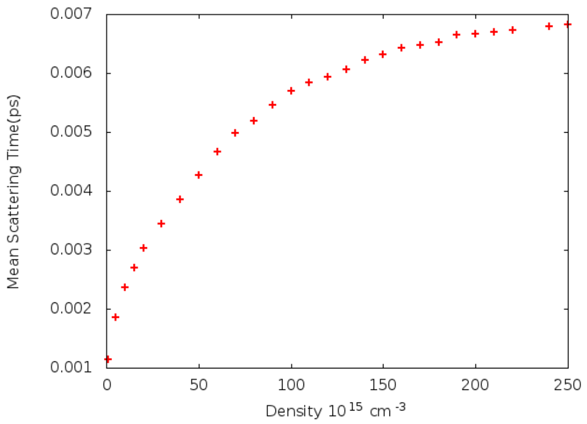

Figure 4.3: The average time between electron-electron scattering events as a function of density. Notably the e-e scattering events are more common at lower densities, as the average time between an event falls. Here and in all others figures unless otherwise specified $T = 300$ K.

4.2.2 Electron Defect and Electron Electron Scattering

The two forms of Coulomb scattering have by far the greatest impact on the scattering properties across the entire density range studied they are the most frequent form of scattering and contain a significant forwards bias. Naively one would expect both mechanisms to be rare at low densities, but this is not the case. For electron-electron scattering the scattering rate actually increases at lower densities while electron-impurity scatterings has a minimum at around 50×10^{15} cm^{-3} and at lower still densities becomes more common (See Figures 4.3 and 4.4). Over the entire observed density rate the electron-impurity scattering does not changed by more than one part in ten. The electron-electron scattering rate behaves even more strangely decreasing monotonically as we increase the impurity density.

Instead of looking at the scattering rate we can multiply it by the average scattering angle, this gives us a good measure of the effectiveness of the scattering (See Figures 4.5 and 4.6), as the scattering angle decreases at

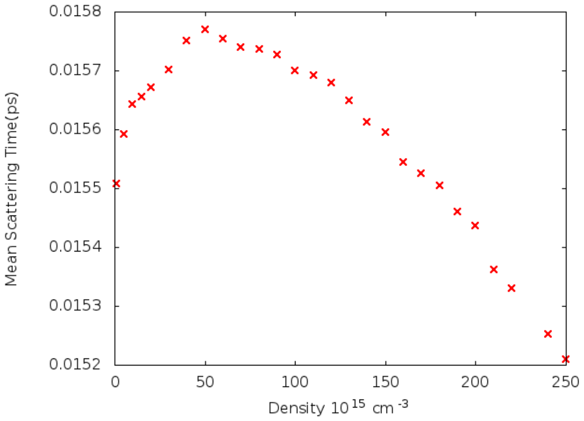

Figure 4.4: The average time between electron-impurity scattering events as a function of density, the change throughout the density range considered is small.

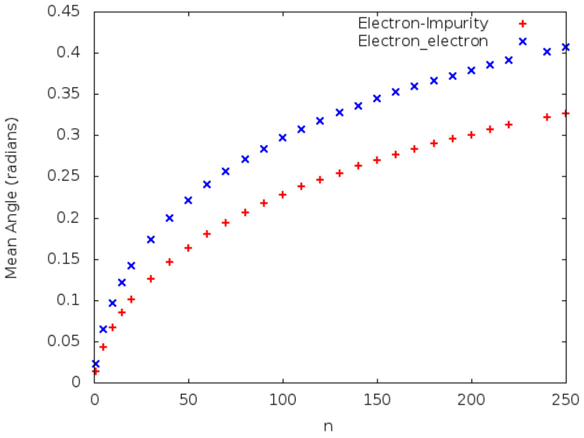

Figure 4.5: The mean angle that the particles are scattered by increases for increasing density, it is this not the scattering rate that gives rise to stronger electron-electron interactions at high densities

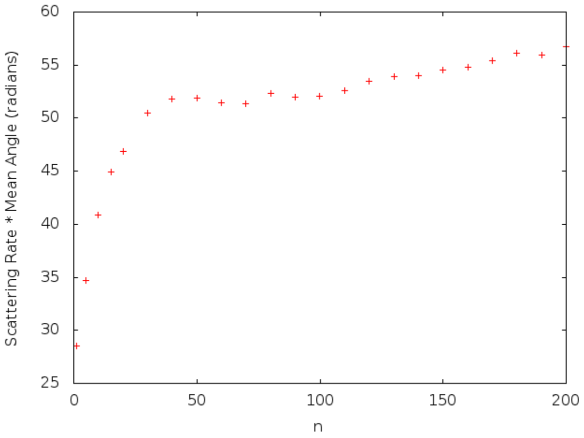

Figure 4.6: The mean angle multiplied by the scattering rate for electron-electron scattering, it does fall dramatically at low densities, but does not vanish, this suggests that even at very low densities the electron-electron scattering will have a strong influence on the overall scattering properties, and hence the depolarisation time. This does not seem to be physically reasonable.

low densities we now see a more reasonable behaviour. As we increase the density this measure of scattering increases in an apparently monotonic way. However the low density limit does not appear to be zero, which suggests that the electron-electron scattering will always play a role even at exceedingly low densities, this does not seem to be correct as we would expect sufficiently low densities the Coulomb interaction such be negligible.

4.2.3 Correlations in scattering events

So far we have discussed the scattering rate of various scatterings as if they are entirely independent of each other, this is in reality not the case, as a single polar optical phonon event raises or drops the energy of an electron by many meV, equivalent to a temperature change of 390 K the behaviour of electrons that have recently undergone a POP absorption event has marked

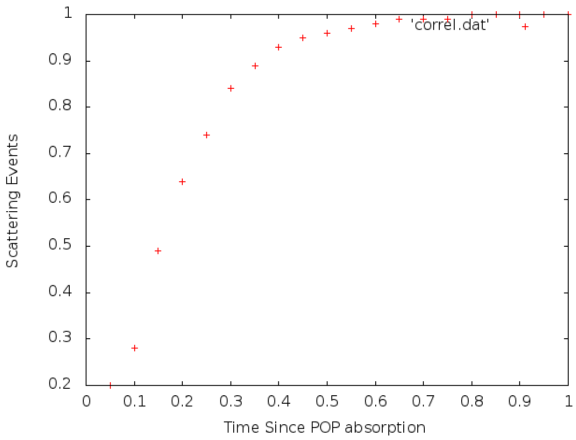

Figure 4.7: The scattering rate immediately after a polar optical phonon scattering is suppressed, here the scattering rate is shown as a ratio with the scattering rate after 1 ps, note that this is the time since the last polar optical phonon scattering, which happen themselves around once every 1 ps. Here the impurity doping density is $n = 1 \times 10^{16}$ cm^{-3} the temperature is 300 K.

differences with the average population. In the time shortly after a polar optical phonon event the electrons are less likely to undergo electron-electron scattering, and if they do scatter will typically scatter by a smaller angle, this effect is stronger the more phonon absorption events it has recently undergone, thus a very hot electron can remain at high energies for a long time (See Figure 4.7).

4.3 Depolarisation Times

The depolarisation time, τ, is defined as the decay constant for the spin polarisation assuming an exponential decay. It is closely related to the decoherence time but that should also include some measure of the change in relative phase, and is discussed later in this chapter. Determining the spin depolarisation time has been the subject of significant experimental study, here we compare to the experiments by Oertel *et al* [69]. This experiment used impurity densities ranging from 5 to $250 \cdot 10^{15}$ cm^{-3} and temperatures from 240 to 360 K. It should be noted that the upper end of the experimental range for densities, especially at lower temperatures, is no longer completely treatable with a non-degenerate approach. This effects only a relatively small portion of the data as we are able to consider some degeneracy effects in a perturbative manner (one approach, altering the screening length to compensate for degeneracy effects, is shown in the next chapter).

4.3.1 Density Dependence of the Depolarisation Time

Using the spin-orbit coupling constant found for the phonon only case, as the low density limit, produces an extremely poor fit to the experimental data, with an inaccuracy of around a factor of two throughout the density range, worse towards the top of the range. To compensate for this we select the value of a_{42} against a moderate density run including electron-electron and electron-impurity scattering (See Figure 4.8). This suggests a value of a_{42} of around 22 $\mathrm{eV\AA}^3$, very close to the value found by Ortel et al [69]. This discrepancy from the phonon only case is probably due to the non negligible impact of the electron-electron scattering even at low densities discussed earlier.

Using this value of the spin-orbit interaction the basic model reproduces the general trend of the data (See Figure 4.9), and is especially accurate up to around $100 \times 10^{15} cm^{-3}$ however beyond that it continues to rise far beyond that which is experimentally observed [69], suggesting that in that regime some unconsidered mechanism may be acting. The next chapter discusses some approaches that can be taken to mitigate this problem. Despite not converging to the phonon limit, as discussed earlier, in low densities the agreement with experiment is reasonable for the low density range.

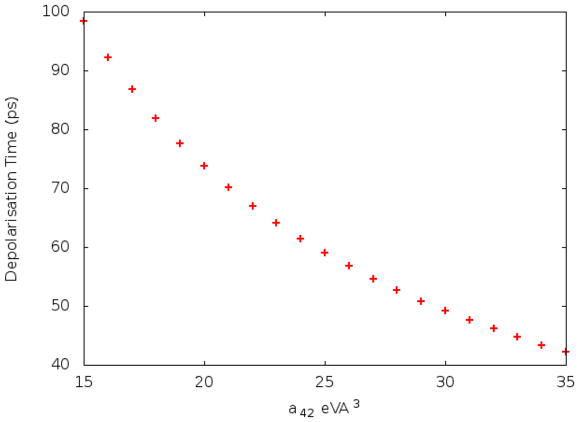

Figure 4.8: At $T = 300$ K and $n = 50 \times 10^{15}$ cm^{-3} the experimental value is 65 ps, here we plot the depolarisation time against a_{42} which suggests the correct a_{42} value is 22 eV$\mathring{A}^3$, further precision is impossible due to the size of the experimental error bars. Here we use a simulation of $N = 100,000$ particles.

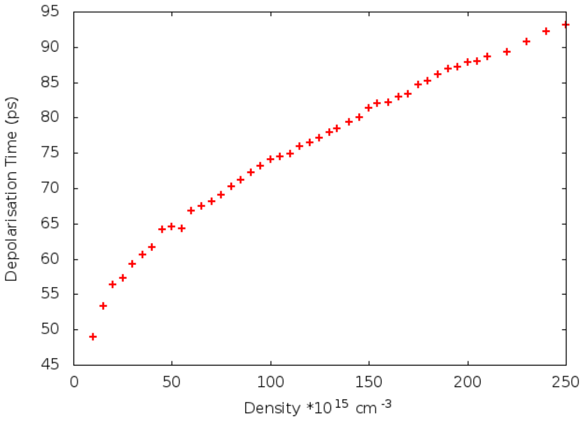

Figure 4.9: The depolarisation time rises with density, at densities greater than $n = 10^{17}$ cm^{-3} we surpass the experimental value, ending inaccurate by over 25%, with no evidence of the flattening experimentally observed. Here $a_{42} = 22$ eV$\mathring{A}^3$.

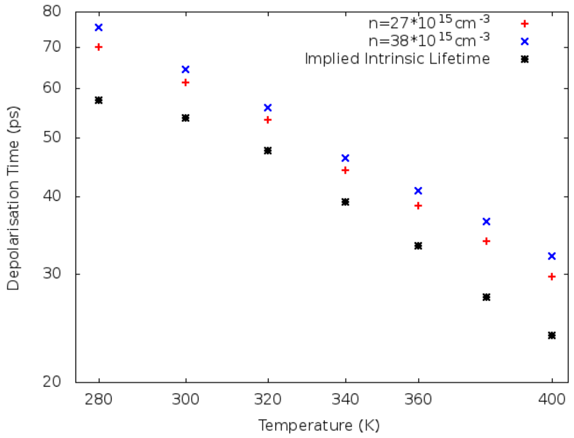

Figure 4.10: The temperature dependence for two different densities, here $a_{42} = 22$ eVÅ^3. We see, as expected, increases the temperature decreases the depolarisation time. From these two values we have also calculated a predicted intrinsic depolarisation time. This shows a slight flattening at low temperatures as the difference between the two densities increases.

4.3.2 Temperature Dependence

Experimentally the temperature dependence has been studied mostly for lower doping densities, here we compare to the results by Oertel *et al.* [69] who studied the temperature dependence at densities of 27 and 38 × 10^{15} cm^{-3}. For these densities we have already seen that the basic model performs well at 300 K and we expect to get a good to fit the experimental temperature dependence.

In comparison with the work by Oertel *et al.* there is a reasonable agreement between the experimental results and our work, this suggests that the model is functioning accurately in the relevant regime. In addition we calculate the implied intrinsic depolarisation time based on these values, the agreement with the experimental results here is reasonable however we observe a slight flattening a low temperatures not present in the experimental results.

4.4 Dephasing

In addition to considering the spin depolarisation we may also wish to consider the time taken for the electron population to have randomised the relative phase of the spin wave function, we refer to the time this takes as the spin dephasing time. The dephasing time is closely related to the depolarisation time but is not proportional to it. As the relative phase is by necessity a two particle phenomenon we determine it by finding the relative phase between a random sample of $1,000,000$ electron pairs. Once we have determined the relative phase for each electron pair we can use the average, of the absolute difference, as a measure of typical phase difference in the sample. That is we use a measure of the coherence by considering the mean *phase* angle between two spins, using a measure of

$$C = 1 - \frac{2\bar{\theta}}{\pi}. \tag{4.1}$$

The dephasing time may have application beyond the "simple" spintronics, as maintaining coherence is a necessary, but not sufficient, criterion for quantum computation.

Starting with the case of all electron spins being aligned in the z direction with no relative phase we can monitor the depolarisation and dephasing together (see Figure 4.11), in general we find that the dephasing is faster that the depolarisation.

For practical quantum computation this dephasing time may well be too fast, it implies a clock cycle of around 25 GHz, considerably faster than even conventional computation which currently have a fastest clock cycle of 5 GHz. Decreasing the temperature would produce a much higher dephasing time but even increasing it to around 250 ps which is equivalent

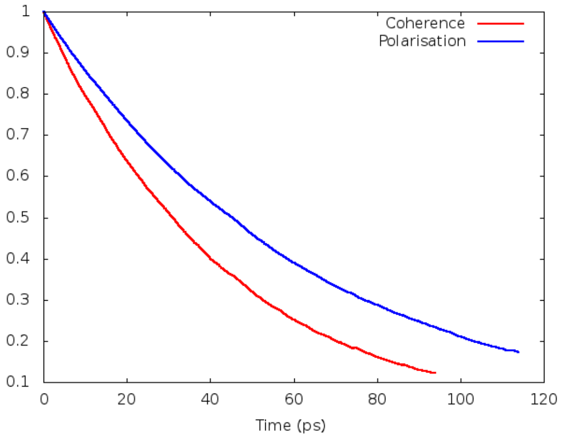

Figure 4.11: The dephasing and the spin polarisation compared. We see that the coherence and polarisation behave very similarly, but that the system loses coherence faster that it depolarises, here the dephasing time is 43 ps. Here $n = 50 \times 10^{15}$ cm$^{-}3$, $T = 300$ K and $a_{42} = 22$ eV$\mathring{A}^3$

to a considerably more manageable 4 GHz, is still unlikely to be enough for viable computation, as this is still a significant loss of coherence over a single cycle, in reality we would wish to maintain coherence for at least hundreds of clock cycles.

4.5 Depolarised Spin Fluctuations

4.5.1 Correlations

The fully spin depolarised state is of interest as it enables us to study the fluctuations in the total spin that emerge as the result of the various scattering mechanisms, these are hard to determine during depolarisation as many fluctuations we would expect to decay at a similar rate to the decay of polarisation. To study this we start by giving each electron a random spin, in addition to its random velocity, these spins are chosen uniformly from the unit sphere. As the selection is not perfectly uniform we would not necessarily expect a zero total spin and during a simulation the fluctuations

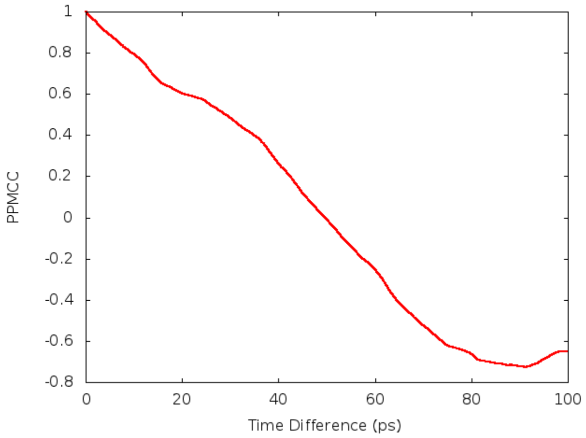

Figure 4.12: The fluctuations in the total modulus of the spin have a short term positive correlation (as measured by Pearson's Product Moment Correlation Coefficient (PPMCC)), but this gives way to a stable long lasting negative correlation. Here and throughout this section $n = 10^{16}$ cm^{-3}, $T = 300$ K and $a_{42} = 22$ eVÅ^3

in this total spin give us a reasonable measure of some of the important time-scales in the spin system.

The total spin appears to have two important characteristic times one a short time noise at around 1 ps that appears to be dominated by small fluctuations carrying out what appears to be a random walk and one a long time general over which the system is negatively correlated. This can be seen by calculating the product moment correlation coefficient[1] of the total magnitude of spin with itself some time later, which shows a short term positive correlation which then gives way to a long time negative correlation (See Figure 4.12).

In addition to these effects which are much as we expected we also see occasional large rapid fluctuations which do not have an obvious origin (See Figure 4.13). These remarkable changes are not well understood, but seem to be correlated to times when there is an increased number of scattering

---

[1] Calculated for two data set x and y as $\frac{\sum(x_i-\mu_x)(y_i-\mu_y)}{\sigma_x\sigma_y}$ (See Chapter 2).

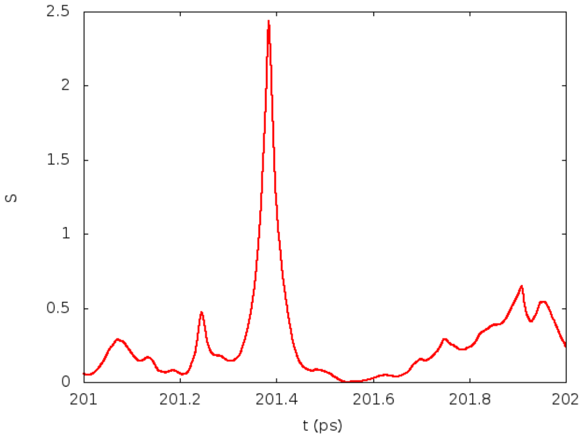

Figure 4.13: The fluctuations in the total modulus of the spin a generally smooth but have occasional sharp changes, this appears to be due to a heightened scattering rate at that time (See Figure 4.14).Many such incidents occur in a normal run.

events (See Figure 4.14), the most likely explanation is that this is caused by a small number of particles reaching abnormally high temperatures and then undergoing many scattering events as they cool down, by scattering with other electrons causing a sudden avalanche of scattering events in many particles. This may cause brief short lived pockets of very hot electrons which rapidly disperse their energy throughout the system by undergoing many scattering events.

4.6 Comparison with alternative electron-electron technique

These results are all based on our implementation of the electron-electron scattering as a local process, in our case one that can only happen within the Debye length. This technique does have the oddity that there is an abrupt jump from scattering being impossible to at a fixed rate once we are within this distance. This is almost certainly not what is actually happening inside

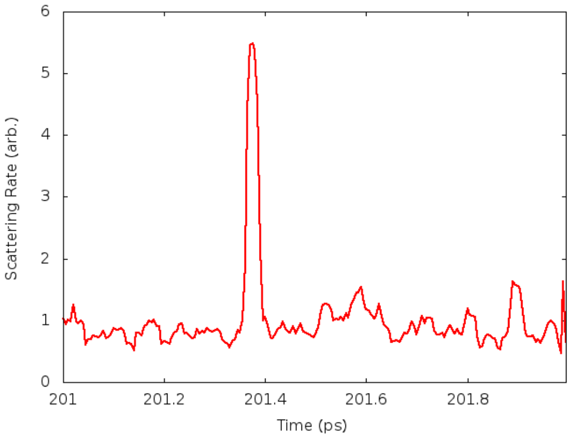

Figure 4.14: The scattering rate during one of the rapid changes in spin polarisation appears to suddenly spike, the mechanism behind this is not well understood. Here the number of scattering events in a time step is compared to the average number, and shown as an implied rate.

a real sample and we should compare the impact of this choice to other ways of handling the electron-electron interaction as a scattering (The next chapter includes an alternative non scattering approach to handling the electron-electron and the electron-impurity scattering).

One commonly implemented approach to the electron-electron scattering is to choose two particles randomly from anywhere in the simulated system but to only update one of the particles (using the non scattered particle purely to provide suitable values for the momentum of the second particle), to compensate the electron-electron rate has to be artificially doubled, providing the sample is bulk and at equilibrium the electrons chosen should be equivalent to choosing from the equilibrium distribution function, but has the advantage that some forms of non equilibrium can be handled (e.g. a step change in temperature for the entire system). This technique obviously fails if there is any spatial variance in the system, particularly problematic is temperature variation.

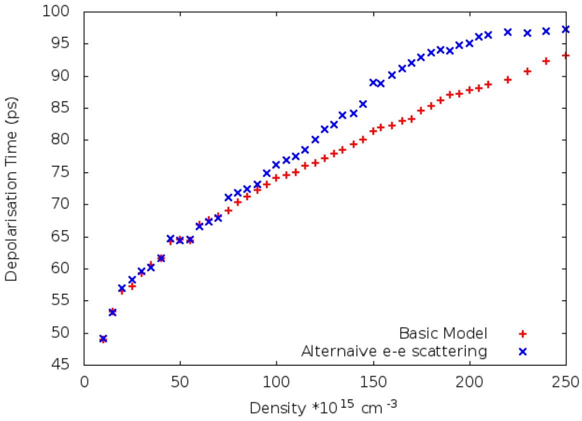

Figure 4.15: The alternative way of handling the electron-electron scattering, is compared to our approach, at 300 K. At low densities the alternative approach to the electron-electron scattering performs just as well, however at higher densities the disagreement with experiment is even worse than the basic model approach.

In general at lot to moderate densities there is little difference between the two methods, but at higher densities we see less of a slowdown than in our model (See Figure 4.15), so the fit to experiment is worse still than our model. This suggests that localising the electron-electron interaction has had some benefit in helping produce the correct behaviour, however it is clearly not enough to explain the entire density range.

4.7 Conclusion

In this chapter we have explored the properties of the electron population in n-doped gallium arsenide, using an ensemble Monte Carlo technique. We started this by considering the scattering, and the impact that has on spin depolarisation, for the case of phonon only scattering. This represents how we would expect the system to behave at very low doping densities, where the electron-electron and electron-ionized impurity interactions would be weak enough that we can neglect them. The inclusion of electron-electron and electron-impurity scattering, even at low doping densities does not exactly reproduce the phonon only case, which may be due to the high scattering rate for electron-electron scattering, even at low doping densities. As evidenced by the inclusion of electron-electron and electron impurity scattering causing an increase in the depolarisation time of up to around 100% we see that the phonon scattering and the charge scatterings are of roughly equal importance, with the exact amounts depending on the density and temperature.

Using the ensemble Monte Carlo model developed and comparison to the experiments by Oertel et al. we have found that the spin orbit coupling constant has a value of 22 ± 0.2 eVÅ^3, within the known experimental range in general and in agreement with the Oertel value in particular.

The basic model presented so far produces reasonable quantitative agreement with experimental studies of the depolarisation time in n-doped gallium arsenide, however for large doping densities it fails to reproduce the saturation in depolarisation time experimentally observed. In the next chapter three potential approaches to increasing the accuracy of the simulation and thereby improving on this behaviour are presented. Similarly at very low doping densities the simulation may be overestimating the role of the electron-electron scattering causing a deviation from the low doping density results, however this region is difficult to explore experimentally so limited studies exist in this area.

Despite the concerns the model is generally successful and with only one free parameter the extent of the agreement is good, further development of this approach may yet be able to fix the issues already outlined, the obvious approach being a more detailed scattering description that allows for multiple particle scattering but such a method was beyond the scope of this research project.

Chapter 5

Beyond the Basic Scattering Approach

While we have seen, in Chapter 4, that the scattering approach using the Debye screening formula is enough to generate a reasonable agreement between theory and experiment throughout the majority of the doping density range studied experimentally, we nonetheless have poor agreement at the higher doping densities ($n > 150 \times 10^{15}$ cm^{-3}), and seen that the system behaves strangely at low densities. As this is a problem due to variation in doping densities it seems natural to consider the mechanisms that vary with doping density (that is electron-electron and electron-Ionized impurity scattering).

In this chapter we discuss further extensions that can be made to the scattering approach, and as they prove unsatisfactory we look at an alternative approach using the classical forces acting on each electron. This classical forces technique is considerably more computationally intensive and the initial part of that discussion deals with the details of implementing an efficient particle forces algorithm (the Barnes-Hut Scheme), before discussing the results of using it.

The work of the improved scattering, i.e. the improved screening length and the third body rejection technique, is primarily the work of Gionni Marchetti, although I did contribute significantly to the implementation of the third body rejection technique, and is included in here for completeness.

5.1 Improved Scattering

5.1.1 Beyond The Debye Approach

The Debye screening approach is only valid in the limit of a non-degenerate gas, i.e. when the chemical potential is much less than the average thermal energy, while this is certainly satisfied at the lower end of our density regime, as we reach the higher end we start to enter an intermediate regime where it is not obvious *a priori* that the thermal energy is sufficiently high that neglecting degeneracy is justifiable (for example at $n = 100 \times 10^{15}$ cm^{-3} the Fermi temperature is 136 K, still smaller than the temperature but perhaps no longer negligible. To calculate the screening we need to evaluate [83]

$$\beta^2 = \frac{ne^2}{k_b T}\frac{\mathcal{F}_{-1/2}(\mu_f)}{\mathcal{F}_{+1/2}(\mu_f)}, \tag{5.1}$$

where β is the inverse screening length,μ_f is the reduced chemical potential (i.e. $^{E_f}/_{k_B T}$) and $\mathcal{F}_j$ is the Fermi-Dirac integral of order j $(\mathcal{F}_j(x) = \frac{1}{\Gamma(j+1)}\int_0^\infty \frac{t^j}{\exp(t-x)+1}dt)$[1] . It should be noted that the first part of this, $\beta_{\text{Deb}} = \frac{ne^2}{k_b T}$, is simply the inverse Debye screening length squared. As such we can simplify this expression to

$$\beta^2 = \beta^2_{\text{Deb}}\frac{\mathcal{F}_{-1/2}(\mu_f)}{\mathcal{F}_{+1/2}(\mu_f)}. \tag{5.2}$$

---

[1] Here Γ is the Gamma function $(\Gamma(x) = \int_0^\infty x^{t-1}e^{-x}dx.)$

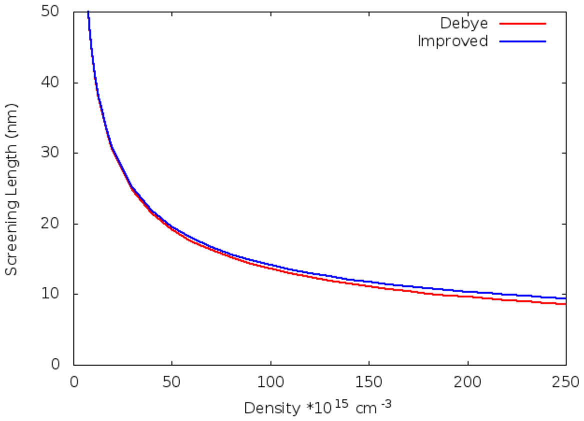

Figure 5.1: The improved calculation of the screening length makes a difference of at most a few percent. Here we use a temperature of 300 K

The impact of this is the suppression of the inverse screening length, i.e. an increase in the screening length (see Figure 5.1). The impact is however small and as such does not significantly reduce the problems at high densities.

5.1.2 Third Body Rejection Criteria

While the inaccuracy of the screening length at high densities goes some way towards explaining the lack of flattening in the depolarisation time that is experimentally observed, it is not sufficient to count for the entire effect. An additional effect is that our scattering does not account for three, or more, body effects. In some cases two particles may be expected to scatter significantly, but in reality a third nearby scattering centre would strongly influence any longer range scattering effects. To compensate for this we could attempt to discard all scattering that consists of two particles that are not each the nearest particle to each other, this approach seems reasonable it can suppress the scattering to an arbitrary amount[2] so instead a more

---

[2] Additionally this approach is incredibly sensitive to the exact position of each electron.

general approach is required.

The third body rejection rate derived by Van de Roer and Widdershoven [84], is a reduction in the probability of scattering based on the average probability of a nearby scattering centre giving a reduced scattering rate, Γ_{tbr}, of

$$\Gamma_{tbr}(v) = \frac{v}{a}\left[1 - \exp\left(-\frac{a}{v}\Gamma_{ee}(v)\right)\right], \tag{5.3}$$

where a is the typical distance between particles, i.e. $a = \frac{4}{\pi}\frac{1}{\sqrt[3]{n}}$. It is this approach that we implement.

5.1.3 Results

The third body rejection method is a much stronger effect than the improved screening length calculation (which changes the scattering rates and mean scattering angle by less than 5% when compared to the Debye approach. The third body rejection reduces electron-electron scattering by around 15% at the top of the range (see Figure 5.2) but unfortunately also plays a significant role at lower densities meaning a poorer agreement at those densities. The two effects together do produce a reasonable agreement with the experimental values of the depolarisation time at higher densities and taken on its own the improved screening length is reasonable at densities less than 100×10^{15} cm^{-3}, where it is indistinguishable from the Debye limit. (See Figure 5.3)[3].

This could simply be a product of this method overestimating the rate of third body rejection at lower densities, but it is not obvious how we could further improve on the method. Neither of the methods do anything to address the poor performance at very low densities and the nonphysical

---

[3] Noting though the problem of very low densities discussed earlier also is not mitigated

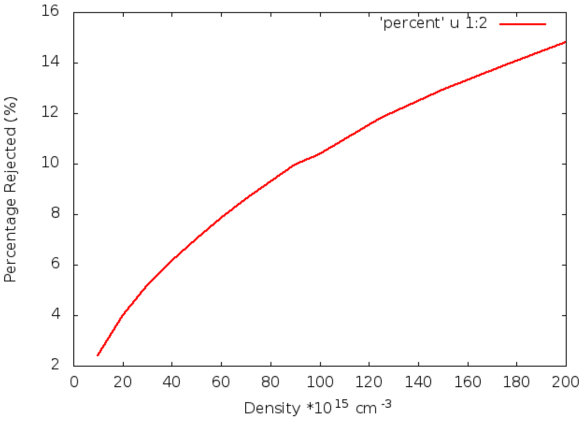

Figure 5.2: The introduction of third body rejection results in a significant suppression of electron-electron scattering at higher densities, however even at densities around 50 to 100 × 10^{15} cm^{-3} the impact is still noticeable.

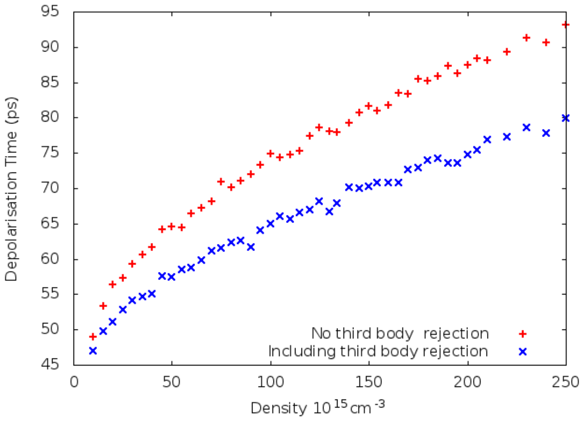

Figure 5.3: The third body rejection rate, by suppressing the scattering rate at high densities prevents the growth of the depolarisation time not experimentally observed, however we do not get agreement with the depolarisation time at lower densities when using this method, the improved screening has negligible impact over the Debye method. Here the temperature is 300 K and the spin orbit coupling constant $a_{42} = 21.9$ $\mathrm{eV\AA}^3$.

difference between simulations with and without electron-electron scattering remains a problem. So while these approaches certainly help to extend the regime that we can simulate correctly they do little to improve our *a priori* predictive power as we have no way of knowing if it is correct to use the third body rejection technique.

5.2 Additional Scattering mechanisms

In addition to the scattering mechanisms studied there are other scattering mechanisms that could play a notable role under a variety of conditions. The most important of these, scattering to higher bands, would be important if the particles had significantly higher energies or in the presence of an applied field, without considering scattering to higher bands we cannot accurately reproduce the behaviour under an applied field of as little as 100μ Vm^{-1}. The extension of our simulation for the consideration of real life device would therefore need to consider the impact of higher bands. We are however at low enough energies that such events are extremely rare (even in a 100 ps run we would not expect to see even a single such event). A similar argument can be made against the necessity to consider Umklapp scattering, which again happens at energies much greater than the typical thermal energy.

Similar arguments exist for all scattering mechanisms that we have considered but inevitably this can become a never ending task, since no matter how many we can eliminate that does not mean other mechanisms not yet considered can't explain the behaviour. So while further scattering mechanisms will certainly play a role in the depolarisation there is no good reason to believe that the divergence from the experiment can be explained simply as the result of the failure to include any particular scattering mechanism. Additionally as increased scattering also increases the depolarisation time

[85] any such mechanism would have to reduce the total scattering at higher densities which while certainly possible is unlikely.

5.3 Classical Forces

A reasonable approach to take is to replace the scattering due to electron-electron and electron-ionized impurities and replace them with the classical interactions between the particles. This approach obviously cannot include some of the finer grained effects of quantum mechanics, such as where the scattering diverges from the classical behaviour, and as such would have little validity in the fully degenerate limit. We can consider the loss of this detail though against the increased quality of the basic electron-electron interaction, for example we no longer are constrained to implicitly assume a lack of correlation in electron positions or a sample of infinite size and uniform densities. The nature of the problem, one that fundamentally must consider $\mathcal{O}(N^2)$ interactions will mean that there is some restriction on the size of systems we can expect to be able to consider in a reasonable timescale.

5.3.1 Computational Technique

To calculate the forces acting on each particle we need to sum over all other particles, as the force is long ranged, such that the force on a given particle is

$$F_i = \sum_{i \neq j} F_{ij}. \tag{5.4}$$

We make the electrostatic approximation which gives rise to forces of $F_{ij} = \frac{q_i q_j}{4\pi\epsilon\epsilon_0} \frac{r_i j}{|r_i j|^3}$. This requires $\mathcal{O}(N^2)$ calculations and as such rapidly becomes computationally intractable (even for moderate numbers of particles).

To avoid this difficulty we use the the Barnes-Hut scheme [44] which is a particle-tree handling of the interaction, reducing the calculation to $\mathcal{O}(N \log N)$. This method is typically used for gravitational simulations, such as planetary formation or galaxy collisions [86]. The Barnes-Hut tree is built recursively for each particle, which are added to the tree sequentially. The Barnes-Hut tree is a data structure in which each level contains averaged properties about the level below (such as the total charge and the centre of charge). Each level is split into eight subsections which are the next level down. Each of these sections is a node and in addition to the physical properties it also contains a pointer to each of its subsections and to the one above it. Before the first particle is added the head node is created, this node is empty at creation. To add a particle to the Barnes-Hut tree we start by adding the particle to the head node and then use the following algorithm (See Figure 5.4).

- Update the total number of particles, total charge and centre of charge (equivalent to the centre of mass, when all particles are the same mass and charge).
- If the particle is the only particle in the current node we have finished.
- If the node contains three or more particles then we determine the appropriate sub node.
    - Sub nodes divide space in eight sections divided at the half way point in x,y,z
- If the node contains exactly two particles (the new particle and one other):
    - First create the eight newly needed empty subnodes

- Then insert one of the two particles into the corresponding subnode
- When that insertion finishes (which will only be one iteration as it is guaranteed to be the only particle in that node), we insert the other particle into its subnode
- This process may need to be repeated an indefinite amount of times, some trigger is needed to terminate the loop in this case.

At the end of this process each particle has a unique subnode (See Figure 5.5), but not all subnodes contain particles and some subnodes contain more subnodes.

This process is expected to have complexity of $\mathcal{O}(\log N)$, but has an infinite worst case. To prevent this we implemented a limit to the number of times the subdivision can occur at which point the particles will always be treated fully. This value makes no noticeable difference provided it is sufficiently large and is simply to prevent two particles placed arbitrarily close from causing an infinite number of subdivisions required. We use a limit of iterations of 25, this means that the chance of two randomly uniformly placed particles exceeding this limit is less than one part in 10^{22}.

Once a particle has been inserted we then move on to the next particle, this brings the total computational cost to $\mathcal{O}(N \log N)$.

Once all particles have been inserted into the tree we are then able to calculate the forces. The Barnes-Hut parameter, θ, defines the accuracy of the scheme. A lower θ leads to more accurate force calculation, but is slower, in the limit that $\theta = 0$ we recover the classical forces limit (albeit at $\mathcal{O}(N^2 \log(N))$. To carry out the force calculation for one particle, we start at the head node and then proceed as follows:

- If the node contains the particle we are interested in, then evaluate all subnodes that contain at least one particle
  - If the node contains only the particle we are interested in then stop.
- If the node does not contain the particle we are interested in we need to determine if we need to calculate the forces
  - If the node contains only one particle we calculate the force, regardless of distance
  - If the node contains more than one particle evaluate the distance from the centre of charge to the particle we are interested in
  - Evaluate $\frac{s}{d}$ where d is the distance and s is the length of the side of the node.
  - If $\frac{s}{d} < \theta$ then calculate the force based on the centre of mass and total charge
  - Otherwise iterate over all subnodes

This approach ensures that there is no spurious self interaction (compared to Poisson type approaches that can never entirely eliminate the self interaction problem) and treats nearby interactions exactly. As the centre of charge approach requires the charge always be the same separate trees are required for the ionized impurities and the electrons. Caution must be taken though as this scheme does not guarantee the conservation of momentum or energy, due to forces not necessarily summing to zero. This is due to the particles interacting sometimes directly with other particles, and sometimes with the tree. Indeed it is possible for one particle to interact directly with another but for the reverse interaction to be with the tree. See Figure 5.6

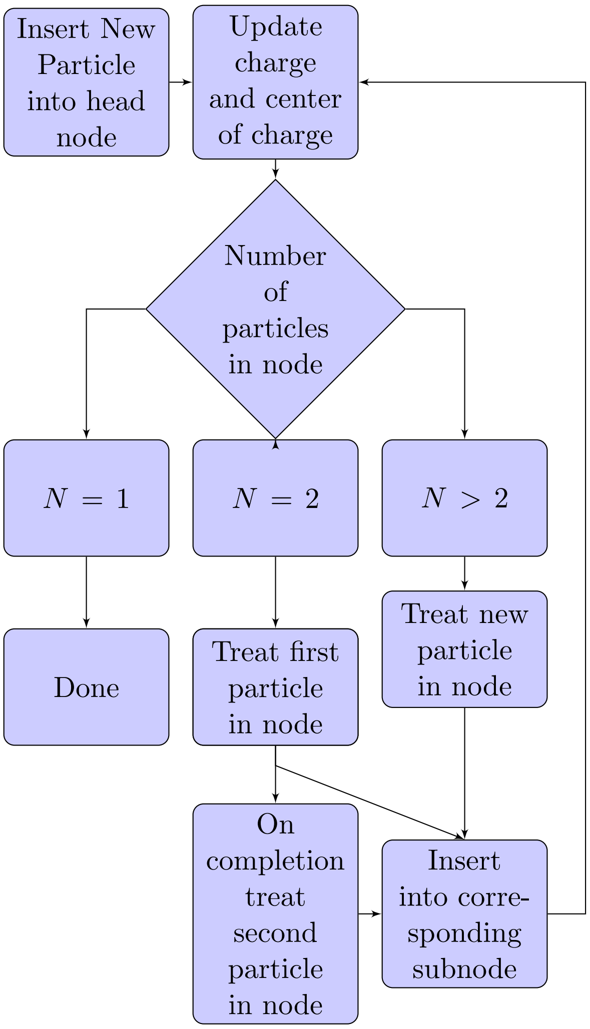

Figure 5.4: Complete Barnes-Hut tree flowchart

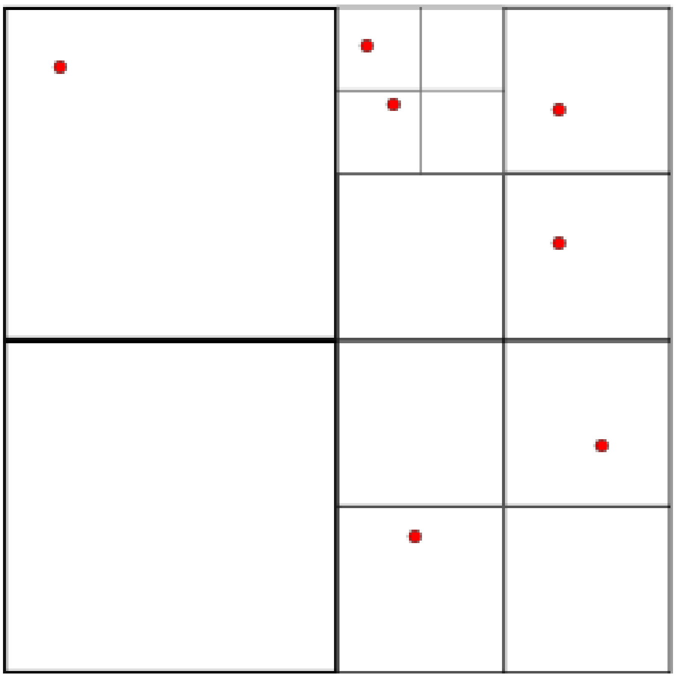

Figure 5.5: Complete Barnes-Hut tree for seven particles, note each of the squares contains either one particle, no particles, or is further subdivided

Force Truncation

So far we have presented what may be considered an idealised form of the numerical algorithm but there a small number of relatively minor corrections that must be made to ensure stability of the electron population. The most notable instability results from the diverging potential as two particles come close together, especially troubling in the case of attracting particles, As our numerical integration scheme contains truncations such rapidly changing forces can cause a notable divergence. In practical terms we observe sudden, apparently spontaneous catastrophic heating during a run. The time for onset of this problem varies wildly dependent on initial positions as well as the impurity density (see Figure 5.7) but is generally seen no later than 10 ps into a simulation.

To correct this we simply introduce a maximum allowable force, above

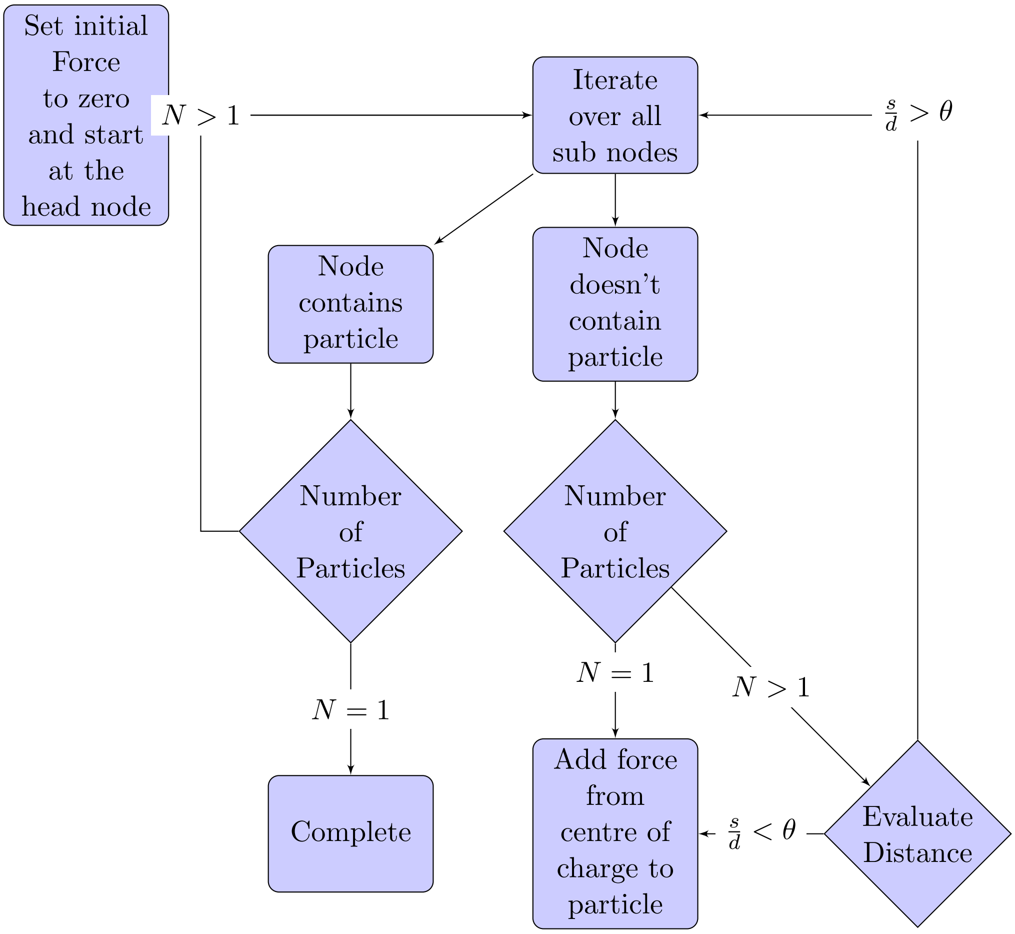

Figure 5.6: Complete Barnes-Hut Forces flowchart

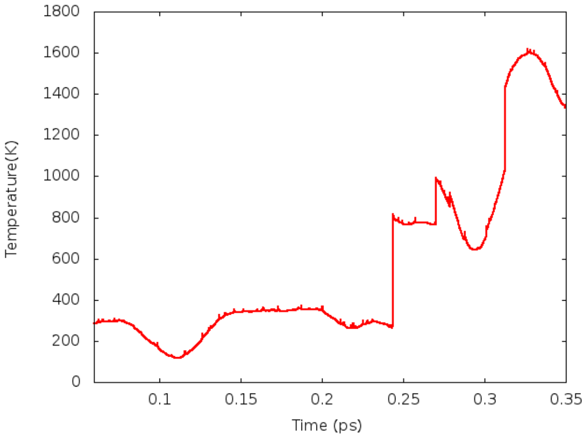

Figure 5.7: In the absence of a truncation in the force, as described in the body, the electron system goes through sudden shock instabilities that catastrophically heat the system in an entirely unstable way.

which the system still sees a force in the same direction but with a magnitude equal to that of maximum allowable force. In choosing the value of this maximum force it is important that we allow it to be large enough that it only impacts very rarely so as to allow the particles to come close enough without impacting the quality of the result, whilst simultaneously it must be small enough that any heating introduced is small. To select an appropriate force we calculate based, on the initial configuration, a mean force; the maximum allowable force is then some constant multiple of this force. Tests we carried out on multiples of $1,000$, $100,000$ and $10,000,000$ particles. Even in the later case there was no observed additional heating (see Figure 5.8). While it may be tempting to consider this due to the polar optical phonon heat bath “soaking up” some of the additional energy; however looking at the number of polar optical phonon events shows, after initial thermalisation, that the two are balanced with no observed excess of phonon emission events.

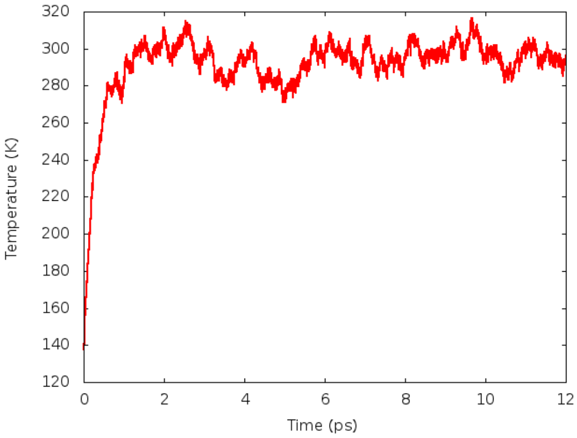

Figure 5.8: The system thermalises to the temperature of the heat bath in a very similar time to the electron-electron scattering case, here we used $5,000$ particles at a density of 25×10^{15} cm^{-3}. The maximum force here is 10 million times the average force found at the initial time step, this truncation is slight so is unlikely to impact the correct evolution of the system.

Boundary Conditions

There is also an instability caused by the use of periodic boundary conditions. This instability is apparent at all temperatures and densities tested, and has its origin in the method of determining the force between two particles a long distance apart. At large distances the particles are not directly interacting with each other, instead they are interacting with a Barnes-Hut box which contains the other particle. If the particle is far enough away that it should be treated through the periodic boundary conditions, but is not so far away that the box that contains it has a centre of mass that does not get the periodicity applied to it then the particle will effectively interact without the periodic boundary conditions. The reverse however may not be true, as a result a significant net force can build up from all the electron-electron interactions, which will tend to radically alter the system momentum.

To remove this problem we must use a different form of boundary condition by considering our sample to be inside a larger material, in this outer

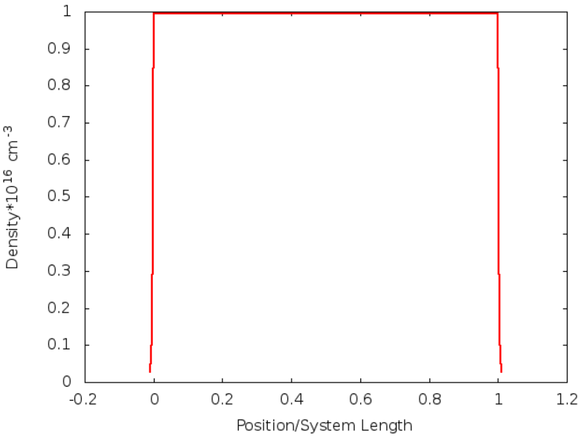

Figure 5.9: By adding additional forces such that it with thermal energy a particle will only reach 0.1% of the main system length the impact to the average density is barely notable. As the potential energy grows quadratically very few particles will ever reach a few multiples of the typical penetration of this outer potential. Here we show the density averaged over 100 ps with $10,000$ particles at 300 K and an impurity density of 25×10^{15} cm^{-3}.

"halo" the particle feels a linearly growing force that attracts it back to the main sample. This does have the impact that the average electron density inside the main sample is slightly reduced but we can tune the outer force to keep this to a reasonable level (see Figure 5.9).

5.3.2 Method Verification and Performance

In addition to the above calculation, checking the temperature of the electron population, we also tested the algorithm to ensure that the forces were being calculated correctly by the Barnes-Hut scheme. The easiest test to carry out is a comparison to the full forces, from which we expect to see some small deviations. The plot of the exact force against the Barnes-Hut force appears to be reasonable, with a roughly linear relationship between the two (a Barnes-Hut constant of zero is equivalent to the full force calculation and in this case the agreement is exact) (See Figure 5.10). Similarly

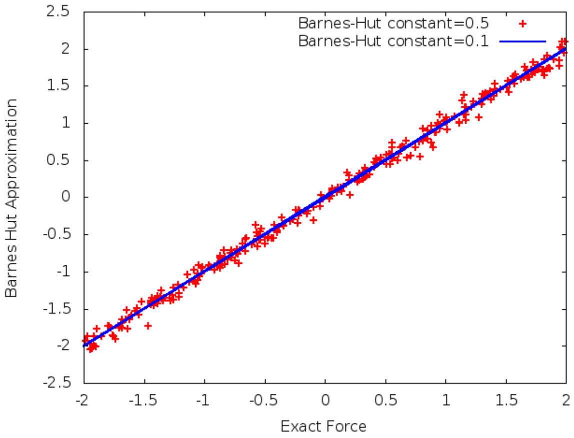

Figure 5.10: The choice of the Barnes-Hut parameter impacts the quality of the agreement between the exact and the approximation calculation of the force, this suggests that the use of a Barnes-Hut constant of around 0.1 is required for accurate force calculation, this value of the Barnes-Hut constant is used in all figures and results using this method. Note this calculation is done in reduced system units and hence is dimensionless.

the performance of the system is in line with the expected $\mathcal{O}(N \log N)$ with a decrease in the Barnes-Hut constant (increasing the accuracy of the calculation) slowing the result as expected.

5.3.3 Results

As the depolarisation against density is smooth at low densities (no abrupt transition when we switch off electron-electron and electron-impurity interactions, unlike in the scattering model, we can use the phonon only low density limit to calculate an appropriate spin orbit coupling constant, a_{42}, of 14 ± 2 eVÅ^3 (See Chapter 4) this value is within the experimental range but is significantly lower than that for the scattering approach. The headline result of depolarisation time against density is in excellent agreement with the experiment throughout the density range (up to $250 * 10^{15}$ cm^{-3}) suggesting that consideration of degeneracy is not necessary to explain the

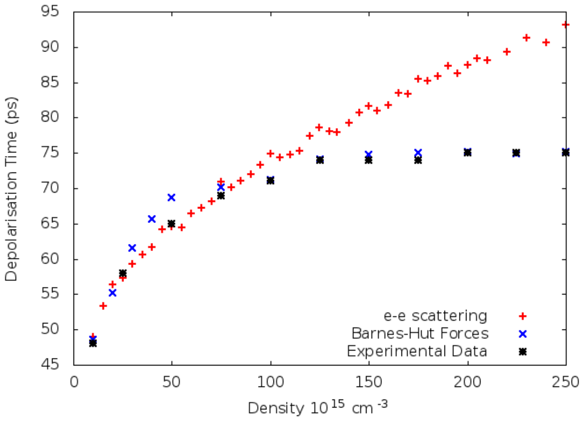

Figure 5.11: The classical forces approach shows excellent agreement with the experimental depolarisation time, throughout the entire range. This suggests degeneracy is unimportant in explaining the saturation of the depolarisation time at high densities, note selected points have been included from the experiments by Oertel [69], even at higher densities the experiment and theory agree within experimental error bars (and certainly have the same qualitative trend), for the full experimental figure see Chapter 2. The run was conducted with a slightly higher value of the spin orbit coupling constant ($a_{42} = 15$ eVÅ^3) than determined earlier using solely the phonon scattering. Here $T = 300$ K.

experimental results (See Figure 5.11) The best fit is achieved using a spin-orbit coupling constant of $a_{42} = 15$ eVÅ^3. Similar quality agreement is found for the comparison of depolarisation time against temperature (See Figure 5.12).

Comparison To Scattering Model Assumptions

The improvements seen by using the classical forces approach suggests that the approximations made in order to derive the scattering approaches cannot be reliable. The most likely cause of the inaccuracy is the assumption that the electron positions are uncorrelated with each other, this can readily be tested against the classical model. The breakdown in the reliability of the approximations goes some way towards explaining the inaccuracies when

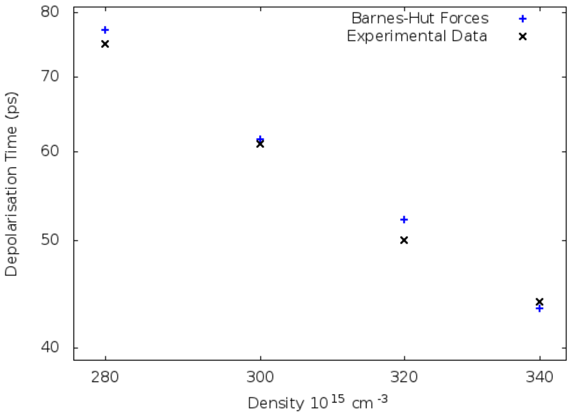

Figure 5.12: The classical forces approach shows excellent agreement with the experimental depolarisation time against temperature, included are selected points from the experiments by Oertel [69]. Here $n = 27 \times 10^15$ cm^{-3}.

compared to experimental results.

The derivation of the scattering rates for the electron-electron and electron impurity scattering treated the electrons as plane waves, implicit in this is a lack of correlation in the electron positions with respect to each other and the ionized impurities. Considering the system from a classical point of view we would anticipate it being unlikely to find two electrons extremely close to each other due to the strong coulomb repulsion, similarly we might expect electrons to be found closer, on average, to the ionized impurities than to an electron.

To determine the probability of finding an electron a distance, r, from another electron we start the simulation with initially random positions and then allow it to thermalise for 10 ps, once thermalisation is complete we randomly choose pairs of electrons and determine the distance between them. As we anticipate the correlations being strongest at shortest distances, we implement a cut-off distance of three times the typical inter-particle distance, this also prevents the boundary conditions having an adverse effect

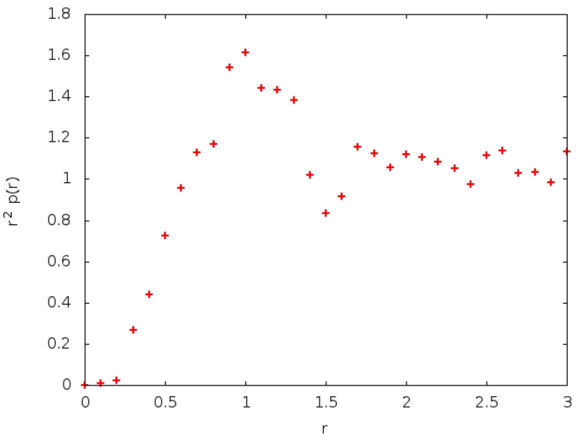

Figure 5.13: The distribution function at higher densities shows a marked reduction in the chance of finding an electron very close to a second electron, note that here we plot $r^2 p(r)$ which removes the reduced number of states at lower distances, if the particles had positions that was purely independent of each other we would expect this distribution to be flat. Here $T = 300$ K and $n = 150 \times 10^{15}$ cm^{-3}.

on the distribution function, as for even the smallest of runs ($N = 5,000$ particles) this cut-off distance is still a small fraction of the length of the entire system.

We see at high densities that there is a significant correlation, with electrons being unlikely to be found near each other, this behaviour is relatively easily understood as originating in the stronger coulomb forces at higher densities (See Figure 5.13). The impact this would have on the spin depolarisation is non trivial but fewer nearby electrons will reduce the rate of exchange of energy and momentum between them, causing electrons to have a longer time between sudden changes brought about by electron-electron interactions, is comparable to a reduction in the scattering rate which would tend to suppress the increase in the depolarisation time at higher densities.

Overall this result gives a good explanation as to why the scattering approach is not reliable at the higher end of densities studied, despite dealing with some corrections that we cannot handle in a classical model (most notably the degeneracy problems), as these corrections are small compared to the errors in the scattering approach' for densities greater than 100×10^{15} cm^{-3}, it do not seem that the inclusion of degeneracy effects is necessary to explain the experimental results. If we were to attempt to extend the model to even higher densities it would be appropriate to attempt to include some version of the degeneracy pressure as a way of introducing this correction into the classical approach, there are though severe limitations to any approach based on quasi-classical properties[4] as we enter a fully degenerate approach and in that regime the use of the ensemble Monte Carlo technique would be dubious at best.

---

[4] For example an inability to include any entanglement

5.4 Conclusions

In this chapter we have seen a few methods for improving on the results found in the earlier chapters. We initially looked at two approaches that improved the scattering rates used for the electron-electron and electron-impurity scattering[5]. These approaches were found to be unsatisfactory as they did not significantly improve our overall agreement (the improved screening length made little difference, while the third body rejection improves the agreement at high densities at a cost of precision at lower densities).

To significantly improve our agreement with experiment over the entire range we had to implement an approach that considered the classical electrostatic forces. This approach certainly could be further extended in a number of fairly obvious ways, for example we could move beyond the electrostatic approximation or introduce degeneracy pressure at higher densities. These corrections are not required though to produce a reasonable model of the electron population capable of reproducing the experimental data across the entire density regime at 300 K. In order to produce a good fit to the experimental data we used the value of a_{42}, calculated by fitting to the low density limit. This is the same as in the phonon only case, suggesting that the system behaves correctly at low densities (As the limiting value of low density behaves the same as the intrinsic non interacting case as we would anticipate).

Using this model we were able to investigate some of the approximations made in deriving the scattering formula for the electron-electron and electron-impurity scattering. This showed that some of the approximations are not valid in the higher density regime and may well explain the poor

---

[5] In the case of the third body rejection approach it is only applied to the electron-electron scattering

agreement with experiment for the basic scattering approach for high densities.

Chapter 6

Interaction with a magnetic impurity

6.1 Introduction

Dilute magnetic semiconductors have recently attracted significant interest, in part because of the unusual magnetic and spintronic properties they possess (See for example [38, 39, 40]). These unusual properties include significant spin polarisation of the equilibrium electron population and long spin relaxation times apparent even at room temperature [87].

In this chapter we outline the theoretical background to extending our model to include a small number of magnetic impurities in otherwise n-doped gallium arsenide; while this approach does have some limitations it still permits us to start developing a process that could, in principle, be used for a more generic class of materials. Throughout this chapter we consider only the impact of a single magnetic impurity and the behaviour of the electron population near to it; further extensions including the introduction of more spin sites and the calculation of total spin properties are natural extensions of this work.

The aim of this chapter is to use the detailed electron model to provide characteristics for a higher level, less detailed, model. This approach would allow simulations of much bigger sizes than is feasible in our model, whilst still maintaining enough of the physics to be realistic.

The Landau-Lifshitz-Gilbert (LLG) equation [88] is the natural approach to implementing an atomistic magnetic model and it is this model for which we calculate parameters using the more detailed electron model. The Landau-Lifshitz-Gilbert equation has been extensively used to simulate a wide variety of magnetic materials including ferromagnets [89, 90], antiferromagnets [91] and more exotic materials for example spin glass [92] materials.

The LLG describes the spin evolution of each magnetic site in the presence of an effective field (H_{eff}); notably it includes a phenomenological damping term (α). Determining the value of the damping constant α is the major theme of this chapter. The LLG equation is [88]

$$\frac{dM}{dt} = -\gamma(M \times H_{eff} - \alpha M \times \frac{dM}{dt}), \tag{6.1}$$

where γ is the gyromagnetic ratio, M is the magnetisation of an individual atom, and α is the phenomenological damping constant.

A number of recent papers have used atomistic spin models to study the response of a magnetic material to an ultrafast laser pulse, typically around 50 femtoseconds in duration [93, 94]. The essential assumption is that the laser energy is transferred to the conduction electron, which heat up rapidly due to their low heat capacity and can achieve temperatures in excess of 1000 K in around 1 ps. The spin dynamics is modelled using Langevin dynamics, which augments the LLG equation with a stochastic field representing thermal fluctuations. The stochastic field H_{therm} is due to the interaction of the magnetic sites with their environment, particularly the conduction electrons. Normally it is assumed that noise is assumed to originate from lots of independent events and is therefore Gaussian[1] and satisfies

$$\langle h^a(t)h^b(t')\rangle = \delta_{ab}\delta(t-t')2\alpha k_B T\mu_s/\gamma, \tag{6.2}$$

where $a, b = x, y, z$ and γ is the gyromagnetic ratio. This guarantees that the system equilibrates to the correct temperature. Although this is an approach which is successful in providing an interpretation of experimental data it is unlikely that the noise is in fact uncorrelated. In this chapter we will discuss the nature of the noise resulting from the interaction with the electron population, including the time correlation and estimate the value for the damping constant, α.

6.1.1 Material

We simulate an n-doped GaAs sample at $T = 300$ K and $n = 50\times10^{15}$ cm^{-3} using the model of the electron population shown earlier. In particular, we use the scattering approach to the electron-electron and electron-ionized impurity interactions, as this model has been shown to adequately reproduce the experimental conditions for this doping density (see Chapter 4) with $N = 20,000$ particles which is large enough that we are not concerned by any impact of the boundary or finite size effects but is still small enough that we are able to conduct the long simulation times required[2].

In addition to the n-doping we introduce a single magnetic impurity,

---

[1] In accordance with the central limit theorem

[2] The difficulty in using the preferred classical forces technique is that some of the results here, particularly for the calculation of the damping constant, α, require extremely long run times which is difficult to achieve with the computational cost of the classical forces code. There is no reason to believe the two techniques would produce significantly different behaviours however as we are in a limit in which they produced similar depolarisation behaviour.

placed at the centre of the material. As there is only a single magnetic impurity we neglect any impact it has on the bandstructure of the system. Notably we do not introduce an electron, or hole, to compensate for the impurity . Additionally we consider only the exchange interactions it induces in the material, of particular note this means we neglect any Coulomb interaction the magnetic spin site would have with nearby electrons.

Although this work is intended to have a more general application as a method to introduce a magnetic site to an ensemble Monte Carlo simulation, the magnetic impurity we use throughout is iron. The nature of this work is highly provisional with additional work required to test the validity of the various assumptions made throughout.

6.2 Theoretical Model

6.2.1 Electron spin thermalisation

Implementation of the magnetic field is introduced by changing the effective field felt by the electron. Prior to the inclusion of the magnetic site the only field considered was the Dresselhaus field (See Chapter 2) we add an additional term such that

$$h_{eff} = h_{dress} + h_{ext}, \tag{6.3}$$

where h_{eff} is the total effective field, h_{dress} is the Dresselhaus field and h_{ext} is the external applied field. To include the impact of the magnetic field on the electron velocity after the time evolution for each time step we apply a rotation to the electron velocity, for the $F = q(v \times B)$ term in the Lorentz force equation [95]. For a magnetic field B applied in the $\hat{z}$ direction this rotation is

$$v_x\left(t+\Delta t\right)=\cos\left(\theta\right)v_x+\sin\left(\theta\right)v_y \tag{6.4}$$

and

$$v_y\left(t+\Delta t\right)=\cos\left(\theta\right)v_y-\sin\left(\theta\right)v_x, \tag{6.5}$$

where $\theta=\Delta t\frac{qB}{m}$.

As we are expecting our electron population to induce the thermalisation to an applied magnetic field via an exchange mechanism, it is reasonable to expect that this is only possible if our electron population correctly thermalises. In Chapter 3 we extensively considered the momentum relaxation to a thermal distribution at the correct temperature but we have made no attempt to show thermalisation of the spin part of the electron wavefunction to an applied field. In the case of the model presented so far, thermalisation of the electron spin to an applied field is not observed; indeed even a strong magnetic field makes no difference to the spin depolarisation time (See Figure 6.1).

Throughout this chapter we wish to see how the system thermalises, this requires the use of a magnetic field that is competitive with thermal energies at the temperature considered. This means the use of implausibly high magnetic fields, ~ 1000 T, while they are far too strong for an applied magnetic field it is no stronger than many exchange fields such as those present in ferromagnetic materials, though of course as we simulate only a single electron it cannot have any magnetic ordering. It should be noted here that the magnetic field does cause the electron spins to precess around it, however as they all precess with the same rate this does not drive spin depolarisation.

To allow the electron spins to thermalise correctly we must introduce infrequent thermal scattering. This scattering represents a large number of sources of thermalisation including electron-electron exchange, spin flips induced by phonon and impurity scattering [7]. We know relatively little about the exact nature of the thermal spin flip scattering but we can introduce a simple model given a few basic facts. Firstly, we know that as a mechanism it is weak compared to other scattering effects, as it does not significantly impact the depolarisation time, which could be fully accounted for without considering it. Secondly, we know that the result of many such scatterings should be a Boltzmann distribution of electron spins. The exact nature of this scattering would require detailed *Ab Initio* work and is beyond the limits of this study, we simply implement a spin scattering process that randomly chooses an angle to the effective field (this includes the spin-orbit interaction as well as an applied field), whilst keeping the azimuthal component constant, this angle (θ) is chosen as

$$p(\cos\theta) = 1 - exp\left(\frac{E_\theta}{k_B T}\right), \tag{6.6}$$

where E_θ is the energy at an angle θ to the applied field. The timescale is expected to be of a similar order to the spin depolarisation time[3], so here we choose 75 ps for the average time between scatterings for a single particle. It should be noted that this is an arbitrary choice and further detailed work could be done to establish a more accurate timescale.

As expected the presence of this scattering causes alignment to an applied field in a time very close to the thermalisation time chosen. The resulting distribution is very close, but not identical, to a Boltzmann dis-

---

[3] Significantly shorter and it would drive depolarisation, significantly longer and it depolarisation would prevent thermalisation to an applied field.

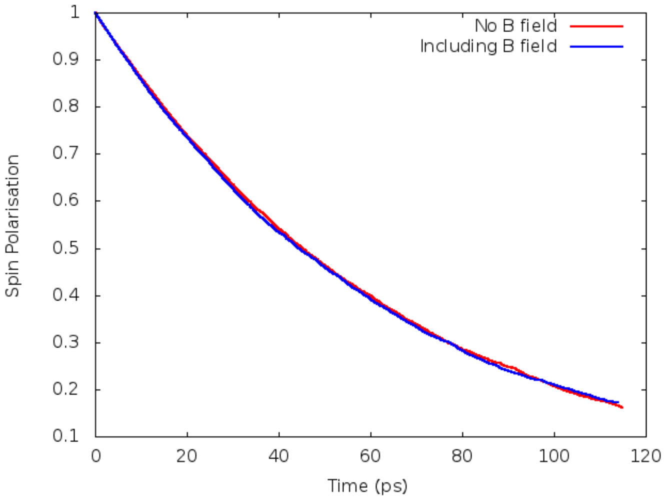

Figure 6.1: The electron population shows no evidence of polarisation to an applied magnetic field, in fact the field makes no difference to the depolarisation. Here we use 50,000 particles.

tribution around the applied field (See Figure 6.2). The difference can be accounted for by the spin-orbit field which means that individual particles at any given time do not experience just the applied field, and so does not simply thermalise to it.

6.2.2 Electron Spin-Magnetic Impurity Interaction

The electron spins interact with the magnetic impurity via an exchange mechanism with the spin site. While we do not know the exact nature of this interaction we would expect it to be fairly short ranged with a distance comparable to the electron wavepacket size as exchange interactions work via the overlap between the two wavefunctions. The exchange [49] is

$$J_{12} = \iint \Psi_1(r_1)\Psi_2(r_2)V(r_1,r_2)\Psi_2(r_1)\Psi_1(r_2)dr_1dr_2, \tag{6.7}$$

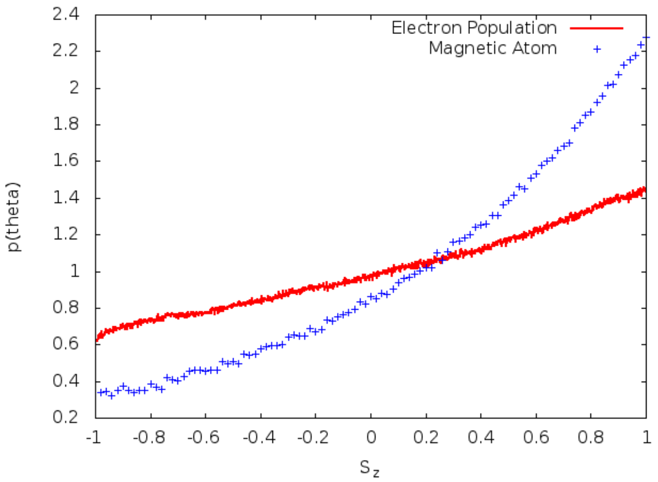

Figure 6.2: The electron population comes into thermal equilibrium with the applied magnetic field as a result of the thermal spin scattering. This induces in the magnetic spin to thermalise. The electron population does not simply thermalise to the applied field due to the presence of the spin-orbit interaction.

where r is the position vector. We model the electron as having a Gaussian wavepacket, with the de Broglie thermal wavelength of $\lambda = \frac{\hbar}{\sqrt{3mk_BT}}$, which gives us a typical value for a room temperature particle of mass m. Therefore we treat the exchange as decaying with distance from the magnetic impurity with $\exp(-\frac{r}{\lambda}^2)$ and with a maximum of $h_{sd} = 6\mathrm{T}$ estimated as 5% of the typical Fe-Fe exchange value [96].

The evolution of the magnetic site was carried out using the method outline in Chapter 3 for the electron spins (i.e. the Crank Nicolson approach).

6.3 Thermalisation of the Magnetic Impurity

6.3.1 Interaction with an idealised electron population

In order to determine if our model of thermalisation is reasonable, we consider a somewhat idealised form of the situation. In order to consider the effects due to imperfect thermalisation it is useful to consider an idealised Boltzmann distribution. Electrons are randomly introduced at a distance of $x = 5\lambda$ from the magnetic site with a velocity v, chosen randomly from the forward biased Boltzmann distribution ($p'(v_x) = v_x p(v_x)$) and a spin chosen from the thermal distribution. This electron undergoes no scattering for the duration of the interaction with the magnetic site. Once the electron is further from the magnetic site than its original position, it is removed and a new particle is introduced. It is not necessary to consider the appropriate time between electron events as during this time the spin merely precesses around the magnetic field and this angle is unimportant for our purposes (as we are looking at the angle to the applied field).

Over time the magnetic spin appears to become properly thermalised, with a Boltzmann distribution of the appropriate temperature (See Figure 6.3). This suggests that the approach of considering the electron population as the source of both the thermal bath and the damping is at least plausible. It should be noted that other sources of thermal noise, including phonon interactions with the magnetic sites would be an additional, albeit minor, source of damping.

6.3.2 Interaction with the Full Electron System

We have established that the magnetic site will thermalise when in contact with an ideal electron gas with a proper thermal distribution of the electron spin and velocity. As such, we have good reason to believe that our method is a plausible explanation of the thermalisation of the magnetic system; to go beyond this we introduce the magnetic site to the electron gas model. The magnetic impurity is placed in the centre of our system and interacts with the electron gas via the exchange mechanism described earlier.

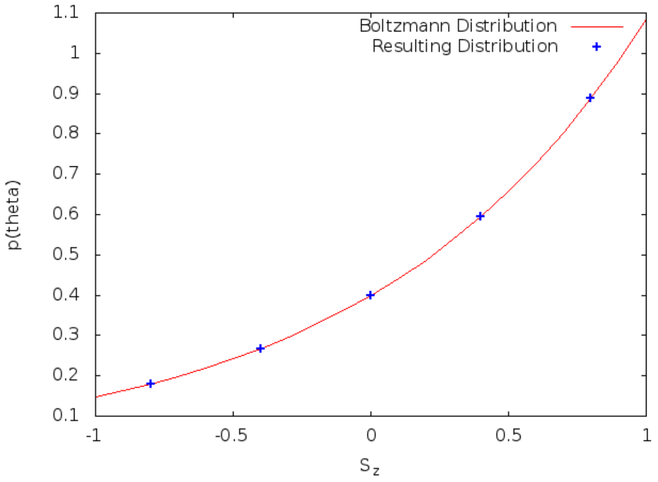

Figure 6.3: The magnetic spin interacting with the idealised electron population, comes to a Boltzmann distribution. Plotted is the Boltzmann distribution and a select number of points at regular intervals.

To carry out our simulation we first thermalise the electron population in the absence of the magnetic site, starting with the correct thermal distribution for the electron spin population in the absence of the spin-orbit coupling. To allow the population to properly reach a thermal equilibrium we carry out this thermalisation step for 150 ps, then introduce the magnetic impurity at the centre of the simulation[4]. The magnetic impurity has its magnetic moment aligned anti-parallel to the applied magnetic field.

Once introduced the magnetic site interacts with the electron population, which slowly results in magnetic reversal, until it eventually comes to be thermalised (See Figure 6.2). During the thermalisation the angle made to the applied field (θ) is plotted as well as a run using the Langevin LLG dynamics (See Figure 6.4), while it is impossible to make an concrete judgement on the similarity of the run from a single particle run the motion does not appear to be significantly different.

---

[4] As our system has periodic boundary conditions the position should make no difference

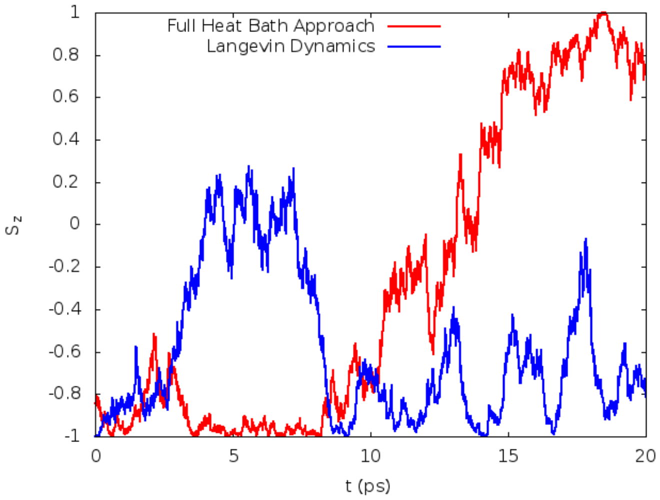

Figure 6.4: The magnetic site and an LLG display similar initial behaviour, here we have chosen $\alpha = 0.03$, a value found for alpha later, it is however impossible to judge if the deviation from each other is simply due to the difference in noise felt by the spins.

6.4 Thermal Noise

As discussed earlier to introduce thermal effects to an LLG model we must add a stochastic term that plays the role of the thermal field. This thermal field is generally assumed to behave as white noise, in that it contains no temporal or spatial correlation and can also be compared to the fluctuations in our electron spin model. The usual thermal field in an LLG model is that of a thermal distribution chosen randomly at each time step with components in each direction of

$$h_{therm} = \mathcal{N}\sqrt{\frac{2\alpha k_b T}{\mu\gamma\Delta t}}, \tag{6.8}$$

where $\mathcal{N}$ is the Normal distribution, γ is the gyromagnetic ratio, α is the damping constant and Δt is the implemented time step. We can compare this to the noise observed in our system, but we must first consider here what is meant by the LLG Δt. The origin of the normal distribution is the consideration that the simulation is at a scale where the random noise processes are much faster than the simulation time scales. As such they can be assumed to be many different random events that can be averaged over. As there are many such events then application of the central limit theorem[5] suggests that the distribution will asymptotically converge on a Gaussian distribution for sufficiently large numbers of events. The assumed lack of correlation in the noise would suggest white noise like behaviour, however we would anticipate that in our system the actual noise would have significant temporal correlation.

6.4.1 Correlated noise

Various types of correlated noise have been studied however the most commonly used is the Ornstein-Uhlenbeck noise [98] which is mean reverting over a characteristic time of τ. To generate Ornstein-Uhlenbeck noise we implement the generating equation

$$\frac{d\vec{H}_{th}}{dt} = -\frac{\vec{H}_{th}}{\tau} + \xi, \tag{6.9}$$

where $\vec{H}_{th}$ is the thermal part of the effective field felt by a magnetic impurity and ξ is a random force whose average is zero and time-correlation function satisfies the fluctuation dissipation theorem.

$$< \xi_i(t)\xi_j(t') >= \frac{\alpha k_B T \delta_{ij} \delta(t-t')}{\tau^2 \gamma \mu}. \tag{6.10}$$

---

[5] Assuming that the individual events are uncorrelated, or at most not too strongly correlated [97] and that they have finite mean, standard deviation, skewness and kurtosis

Integrating over a small time interval Δt to remove the delta functions gives the following expression for the thermal field, H_{th}

$$H_{th}(t + \Delta t) = \left(-\frac{H_{th}(t)}{\tau} + \frac{\sigma \mathcal{N}}{\sqrt{2}\tau} \right) \Delta t, \tag{6.11}$$

where $\mathcal{N}$ is the normal distribution of unit standard deviation and σ is the standard deviation of the the non-correlated noise such that

$$\sigma = \sqrt{\frac{2\alpha k T}{\mu \gamma \Delta t}}. \tag{6.12}$$

Equ. 6.11 can be written as [99]

$$h_{th}(t + \Delta t) = \left(-h_{th}(t) + \frac{\mathcal{N}}{\sqrt{2}} \right) \Delta t / \tau, \tag{6.13}$$

where the reduced thermal field is $h_{th} = H_{th}/\sigma$.

The impact of Ornstein-Uhlenbeck noise is not readily apparent from a casual inspection of the time series of the noise, but is readily apparent from the Fourier Transform in which the magnitude decays with increased frequency [100], the resulting pink noise is very commonly found in many types of electrical noise [101].

We obtain a time series of the noise from the exchange interaction with the electron population, by carrying out a simulation for 50ns, and carry out a Fourier transform on the resulting data. The Fourier transform of the thermal field shows a strong decay at higher frequencies, decaying faster than would be expected of Pink Noise.

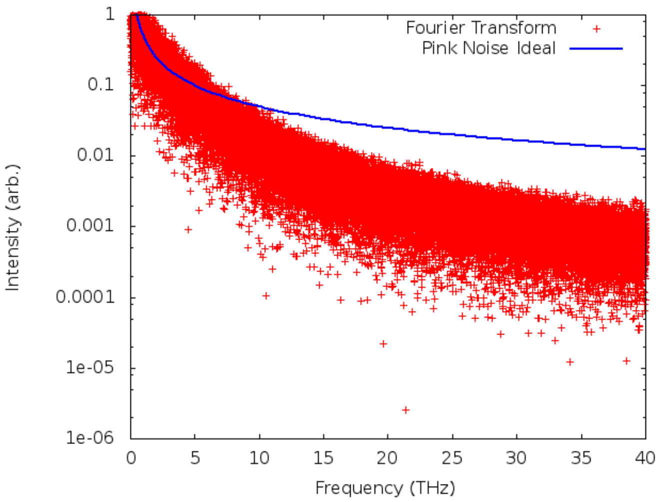

Figure 6.5: The Fourier transform of the noise resulting from the electron model, the low frequency term dominates with the intensity quickly decaying with increased frequency, for comparison we also show a fit of pink noise ($I \propto {}^1\!/_f$). The noise appears to decay faster than the pink noise that would result from a Ornstein-Uhlenbeck process

6.5 Determining α

We have seen that the electron population correctly induces thermalisation in the magnetic atom. This suggests that in such a system the doping and thermalisation can be understood as being, at least in part, due to the exchange interaction with the electron population. To be able to characterise the system for a multiscale approach it is important to calculate the appropriate damping constant α, for the LLG equation.

The value of the damping parameter is important to understanding many of the dynamic properties of a magnetic system and is of particular importance in ferromagnetic resonance (FMR) experiments [102]. However it should be noted that it does not impact the equilibrium properties, such as the Curie temperature[6], as it controls the rate at which the system returns

---

[6] The temperature at which the system ceases to have a net magnetic moment in equilibrium.

to equilibrium, but dose not impact the equilibrium condition.

Conventional experimental calculation of α would require the consideration of the linewidth of an FMR experiment, from which the damping parameter can relatively easily be extracted. This technique however is beyond our capabilities to simulate as it would require a very large number of frequency runs, each of which would take a long time. In addition as we are only dealing with a single spin site it would inevitably be swamped with noise from the system. Instead we consider an approaches based on the properties of our magnetic site, in particular the decorrelation time for the spin.

6.5.1 Determining α using the properties of the magnetic site

To determine the damping constant, α, we might naively set the magnetic atom's spin a long way from equilibrium, for example pointing in the opposite direction to that preferred due to the applied magnetic field. If we simulate an ensemble of magnetic atoms we would expect to see the average case damping to the applied field with a Gilbert-like behaviour. The problem with this approach is that as we get close to thermal equilibrium the system no longer appears to be damping; as it is in thermal equilibrium it is as likely to increase the angle to the applied field as it is to decrease it, this makes it impossible to determine a low θ limit for α.

The damping parameter however does not just determine the damping but is also responsible for the timescale over which the system loses correlation; it is this property that we exploit to determine an accurate value of α. We simulate the magnetic site for a long time (25 ns) and then calculate

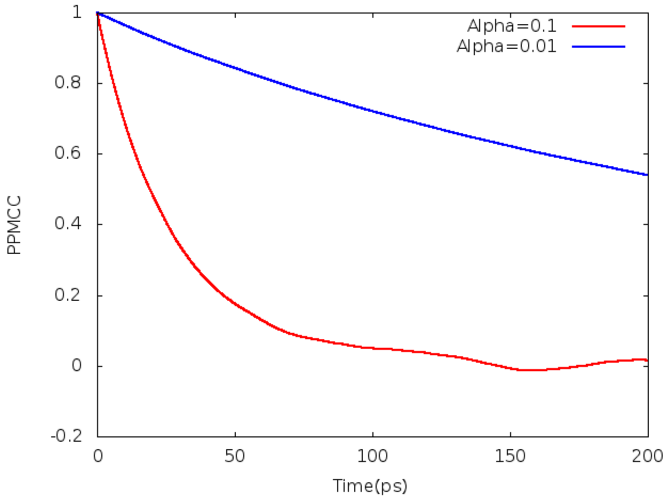

Figure 6.6: The time correlation in the angle to the applied field, decays in a roughly exponential manner. The rate of decay is controlled by the damping parameter, α. Here we ran the LLG simulation for $1\mu s$, before determining the PPMCC (as defined in Chapter 2), based on the value of $\cos\theta$, at time t apart.

the Pearson's product moment correlation coefficient[7] between the θ values with various time differences (See Figure 6.6). As we would expect very short time differences show almost perfect correlation (the system has not had enough time to change), while for longer times the correlation appears to decay exponentially, giving us a typical correlation time of 50 ps (See Figure 6.7).

To use this behaviour we compare to various simulations carried out with different α values using the Landau-Lifshitz Gilbert approach. This approach shows a good agreement between the Langevin enhanced LLG and the electron simulation for an α value of 0.03 ± 0.005. The exact value does appear to have some dependence on the doping density and temperature of the electron "gas", the detail of which is beyond this work but is a fruitful topic of further study.

---

[7] Calculated for two data set x and y as $\frac{\sum(x_i-\mu_x)(y_i-\mu_y)}{\sigma_x\sigma_y}$ (See Chapter 2).

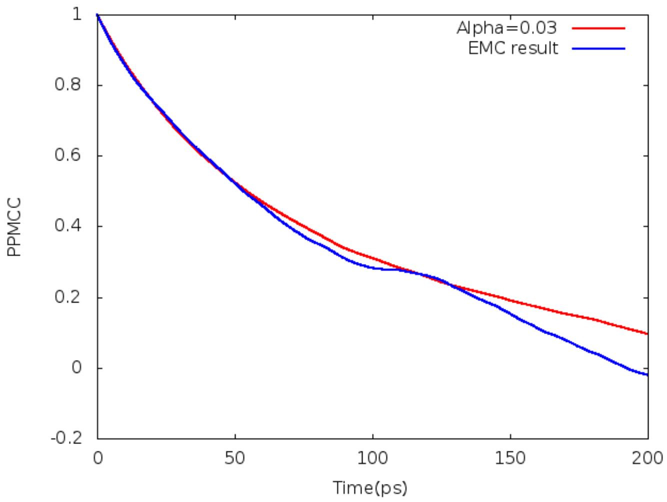

Figure 6.7: The time correlation in the angle to the applied field, here we compare the result from the electron gas spin model to the Langevin LLG result. The Langevin simulation was run for $1\mu s$, while the electron spin model was run for $25ns$ using $N = 25,000$ electrons. The difference in simulation time is due to the extreme computational expense of the electron spin simulation.

6.6 Conclusion

In this chapter we have discussed the introduction of a single magnetic impurity to our sample and we have studied the resulting behaviour. The introduction of a thermalisation term to the spin dynamics of the electron population was also introduced, to ensure the system properly aligns to an applied field. We have studied the interaction of the electron system and seen that it causes the magnetic impurity to damp to the applied field, before eventually reaching thermal equilibrium.

To contrast this with a higher level approach we have compared the observed behaviour to that predicted by a Langevin extension to the Landau-Lifshitz-Gilbert approach and found reasonable agreement. To characterise the unknown damping parameter α, we have considered an approaches based on studying the decorrelation time of the magnetic spin site. This approach shows great agreement between the spin site calculated in our model and a Langevin LLG approach, not only finding a similar timescale but also a very similar type of decay, although computational limitations mean significantly larger noise on the result for the full electron approach, this is especially notable for correlations over large time differences.

The results presented here show that the dynamic behaviour of a single magnetic spin impurity situated in an electron heat bath behaves similarly to a Langevin LLG spin. This suggests that the Langevin enhanced LLG equation, correctly parametrised in terms of the damping constant, is a reasonable atomistic-scale description of the spin dynamics. Further work is suggested to investigate this in more detail and to study the equivalence of the two approaches at elevated temperatures in order to validate the use of the LLG equation in simulations of pulsed laser experiments. Importantly, our model predicts that the electron heat bath cannot be simply represented as a white-noise source. A detailed further study of the correlation time is important in relation to ultrafast magnetisation dynamics since Atxitia *et al.* [45] have shown that the correlation time can have a significant impact on the demagnetisation rate of materials subjected to femtosecond laser pulses.

Further work could be carried out to determine the interaction of two or more spin sites, especially the dependence on distance between them. This could allow a characterisation of the indirect exchange effect which could then be used in a large scale LLG model to determine a variety of material properties including the Curie temperature and the response to an applied field. Additional work could also be carried out on a material such as Gallium Manganese with Iron doping where all the doping sites are magnetic; such a system could then feasibly be simulated using an approach very similar to our approach to study the overall magnetic properties.

Chapter 7

Conclusion

7.1 Summary

In Chapter 2 we introduced the background to the ensemble Monte Carlo technique for simulating the electron population in a semiconductor. For this approach we discussed the dominate scattering mechanisms, which are polar optical phonons, electron-electron and electron-ionized Impurity scattering and acoustic phonon scattering. We also discussed the role of inversion asymmetry giving rise to a spin-orbit coupling parameter which drives the spin depolarisation and spin dephasing. We also introduced the experimental results by Oertel *et al.* [69] which we used throughout the Thesis as our standard experimental data set for comparison to our simulation results.

In Chapter 3 we introduced a limitation of the electron-electron scattering, specifically only allowing scattering between nearby electrons, motivated by a desire to realistically simulate a system much larger than the typical inter-electron distances, in which we would not anticipate overly long range scattering type interactions. This distance limit however has to be introduced artificially as the scattering rates were derived using a plane wave basis and as such do not contain any spatial information. We compared two methods for carrying out the spin evolution of the electron spin, the Heun scheme [75] and the Crank Nicolson scheme [76] showing that the Crank Nicolson is more efficient, more accurate and retains more information than the Heun scheme, which we judged to be more than worth the 33% increase in memory cost. We also discussed the limitations of various approaches to determining the spin depolarisation time, comparing three techniques, an exponential best fit, the time taken to reach a fixed polarisation and a time based on the average ratio of the spin with a time delay. The ratio method appears to be the best method as it introduces no apparent systematic error and has smaller finite size effects than the exponential best fit. A method, although unused in this Thesis due to time constraints, based on the time averaged field was shown to be the optimal method for calculation of the spin depolarisation time.

In Chapter 4 we discussed the material properties that we can determine using the ensemble Monte Carlo technique. These properties can be divided into two types, firstly the electronic properties, considering how the electrons behave and secondly the spin properties. Particularly important was the low density behaviour of the electron-electron scattering which remains important even at the lower densities, it is not as expected as a linear increase of electron-electron scatterings with increasing densities is generally predicted [69]. We looked closely at the spin depolarisation time and how it varied with density and temperature, showing good agreement with experiment for doping densities below $n = 100 \times 10^{15}\mathrm{cm}^{-3}$ however at higher densities our simulation overestimates the depolarisation time. Chapter 4 had substantial overlap with a paper by Gionni Marchetti, James McHugh, Irene D'Amico, Roy Chantrell and myself [81], however the paper introduces some modification to the basic model presented in Chapter 4, in particular in Chapter 4 we use a Debye screening, rather than the more complex form presented and used in the paper.

In Chapter 5 we compared three different approaches to further improving the accuracy of the simulation, introducing a degeneracy correction, a third body rejection technique and the classical electrostatic forces (which replaced the electron-electron and electron-ionized impurity scatterings). The degeneracy correction was shown to be very small, and as such could not account for the difference from the experimental results, suggesting that degeneracy effects are too small even at the higher densities to be an important mechanism. The third body rejection technique has a more dramatic impact, slowing (or perhaps halting) the increasing depolarisation time at high densities in accordance with experiment, it however undermines the behaviour at moderate to low densities decreasing the agreement with experiment in that regime.

The final approach considered, the simulation of the classical electrostatic forces is considerably more computationally expensive than the scattering approach despite using the Barnes-Hut scheme [44] which improves the efficiency of the calculation by grouping distant particles. This computational cost is however more than worth it as the resulting depolarisation times are much more accurate, showing the correct qualitative behaviour, reaching a maximum depolarisation time of 75 ps comparable to the experimental value, although slightly exceeding it. This discrepancy can be accounted for by considering the error in the spin orbit coupling which we have no precise value for.

In Chapter 6 we added a single magnetic atom to our simulation and tried to determine how it will interact with the electron gas. When we include a strong applied magnetic field the magnetic site precesses around the magnetic field and slowly aligns to it. This damping is characterised in terms of a Landau-Lifshitz-Gilbert equation [78]. The phenomenological damping constant α can be estimated by comparing the results of a magnetic spin in our electron model with that of one in a LLG type approach. To find the value of the damping constant we used the time taken for the component of the spin aligned to the magnetic field to become uncorrelated in time. The damping constant is crucial in determining this decorrelation effect and the correlation appeared to decay in an exponential manner in both the LLG and full electron simulation, by comparing the depolarisation curves this suggests a damping of $\alpha = 0.003$.

In addition we looked at the noise felt by the magnetic spin for low times and showed that in that limit the system did not have the typical Gaussian white noise, but when averaged over for longer times the noise appeared to become white noise like, as would be expected from the central limit theorem.

7.2 Further Work

The electrostatic forces version of the model shows excellent agreement to experiment across the density range studied, but fundamentally is only valid in the non-degenerate limit, we certainly would never be able to consider the fully degenerate limit with such a model we can certainly look to add some corrections for degeneracy. The obvious way to continue would be the introduction of an additional electron-electron force to play the role of degeneracy pressure. Although the details of this approach would need to be considered the electron degeneracy pressure has the well known formula [103]

$$P = \frac{\left(3\pi^2\right)^{2/3}\hbar^2}{5m_e}\rho_N^{5/3}. \tag{7.1}$$

To approach this we would need to form a discretised version of the degeneracy pressure, preferably one that works on a pair of particles basis. This would allow us to simulate a larger range of temperatures and densities than we are currently able to consider.

We already have an approach that allows us to place the ionized impurities in whatever locations we want (although so far we choose to do so only in a random manner) so it is fairly natural to extend the model to the simulation of device properties. Depending on the exact nature of the device this would necessitate the introduction of some additional scattering mechanisms, certainly we would want to consider the importance of scattering to higher bands and probably we would also want to consider the introduction of a non parabolic band. A large scale extension of the model would require the ability to handle many more electrons, which requires the parallelisation of the model which is achievable as the algorithms implemented all fairly naturally parrellize, the only difficulty may be the Barnes-Hut scheme but reasonable parallel algorithms for this already exist [104].

The introduction of more magnetic impurities is also a reasonable way to extend the model and would allow the calculation of the induced exchange interaction between magnetic sites. This would require an understanding of the exchange between the different electrons, and would make it possible to use the information in a larger LLG model which could then simulate much larger devices. This would be a multiscale approach and seems a natural way of exploring sufficiently large magnetic impurities to determine important magnetic properties such as the Curie temperature, and more generally the demagnetisation curve. We have seen that the thermal noise from the electron model is correlated over time scales that are shorter than those normally present for magnetic systems, it would be interesting to look at the behaviours where short time scale events are important, for example ultrafast laser heating [105] requires an understanding of the electron system on very short time periods, and is readily implementable using our electron model by adding a laser heating scattering term to the electron dynamics.

Bibliography

[1] M. Holub, J. Shin, D. Saha, and P. Bhattacharya. Electrical spin injection and threshold reduction in a semiconductor laser. *Phys. Rev. Lett.*, 98:146603, Apr 2007.

[2] Datta, Supriyo, and Biswajit Das. Electronic analog of the electro optic modulator. *Applied Physics Letters*, 56(7):665, 1990.

[3] Johan Akerman. Toward a universal memory. *Science*, 308(5721):508–510, 2005.

[4] Igor Žutić, Jaroslav Fabian, and S. Das Sarma. Spintronics: Fundamentals and applications. *Rev. Mod. Phys.*, 76:323–410, Apr 2004.

[5] S.A. Wolf, A. Y. Chtchelkanova, and D.M. Treger. Spintronics a retrospective and perspective. *IBM Journal of Research and Development*, 50(1):101–110, 2006.

[6] S. A. Wolf, D. D. Awschalom, R. A. Buhrman, J. M. Daughton, S. von Molnár, M. L. Roukes, A. Y. Chtchelkanova, and D. M. Treger. Spintronics: A spin-based electronics vision for the future. *Science*, 294(5546):1488–1495, 2001.

[7] S. Bandyopadhyay and M. Cahay. *An Introduction to Spintronics.* CRC PressINC, 2008.

[8] P. Strange. *Relativistic Quantum Mechanics: With Applications in Condensed Matter and Atomic Physics.* Cambridge University Press, 1998.

[9] Michio Kaku. Tweaking Moore's law: Computers of the post-silicon era, 2012.

[10] Ethan Mollick. Establishing Moore's law. *IEEE Annals of the History of Computing*, 28(3):62–75, 2006.

[11] M.H. Kryder and Chang Soo Kim. After hard drives what comes next? *Magnetics, IEEE Transactions on*, 45(10):3406–3413, 2009.

[12] D.E. Knuth. *The Art of Computer Programming: Fundamental algorithms.* Addison-Wesley Series in Computer Science and Information Processing. Addison-Wesley Publishing Company, 1973.

[13] D. Perez. *New NVIDIA GPU Breaks One Billion Pixels Per Second Barrier.* NVIDIA Press Release, 2000.

[14] D.R. Simon. On the power of quantum computation. In *Foundations of Computer Science, 1994 Proceedings., 35th Annual Symposium on*, pages 116–123, 1994.

[15] LM Adleman. Molecular computation of solutions to combinatorial problems. *Science*, 266(5187):1021–1024, 1994.

[16] D.G. Feitelson. *Optical computing: a survey for computer scientists.* Artificial Intelligence Series. MIT Press, 1988.

[17] E.R. Griffor. *Handbook of Computability Theory.* Studies in Logic and the Foundations of Mathematics. Elsevier Science, 1999.

[18] Ethan Bernstein and Umesh Vazirani. Quantum complexity theory. In *in Proc. 25th Annual ACM Symposium on Theory of Computing, ACM*, pages 11–20, 1993.

[19] E. Bernstein and U. Vazirani. Quantum complexity theory. *SIAM Journal on Computing*, 26(5):1411–1473, 1997.

[20] R Tucker. The role of optics in computing. *Nature Photonics*, 4(7):405, 2010.

[21] M. N. Baibich, J. M. Broto, A. Fert, F. Nguyen Van Dau, F. Petroff, P. Etienne, G. Creuzet, A. Friederich, and J. Chazelas. Giant magnetoresistance of (001)Fe/(001)Cr magnetic superlattices. *Phys. Rev. Lett.*, 61:2472–2475, Nov 1988.

[22] K.H.J. Buschow. *Concise Encyclopedia of Magnetic and Superconducting Materials*. Advances in Materials Sciences and Engineering. Elsevier Science, 2005.

[23] R.J. Baker, Institute of Electrical, Electronics Engineers, and IEEE Solid-State Circuits Society. *CMOS: Circuit Design, Layout, and Simulation*. Number v. 1 in IEEE Press Series on Microelectronic Systems. Wiley, 2008.

[24] S.G. Narendra and A.P. Chandrakasan. *Leakage in Nanometer CMOS Technologies*. Series on integrated circuits and systems. Springer, 2006.

[25] Sadamichi Maekawa, Hiroto Adachi, Ken ichi Uchida, Jun'ichi Ieda, and Eiji Saitoh. Spin current: Experimental and theoretical aspects. *Journal of the Physical Society of Japan*, 82(10):102002, 2013.

[26] I. D'Amico and C. A. Ullrich. Nonlocal formulation of spin coulomb drag. *Phys. Rev. B*, 88:155324, Oct 2013.

[27] S. Kakaç, H. Yüncü, K. Hijikata, and H. Hijikata. *Cooling of Electronic Systems.* NATO ASI series: Applied sciences. Springer Netherlands, 1994.

[28] K L Wang, J G Alzate, and P Khalili Amiri. Low-power non-volatile spintronic memory: Stt-ram and beyond. *Journal of Physics D: Applied Physics*, 46(7):074003, 2013.

[29] J. M. D. Coey and M. Venkatesan. Half-metallic ferromagnetism: Example of CrO2 (invited). *Journal of Applied Physics*, 91(10):8345–8350, 2002.

[30] M. Donath and W. Nolting. *Local-Moment Ferromagnets: Unique Properties for Modern Applications.* Lecture Notes in Physics. Springer, 2005.

[31] G.B. Johnston and E.O. Hall. Studies on the heusler alloys—I. Cu2MnAl and associated structures. *Journal of Physics and Chemistry of Solids*, 29(2):193 – 200, 1968.

[32] S.J. Moss and A. Ledwith. *Chemistry of the Semiconductor Industry.* Springer, 1989.

[33] E. Yablonovitch, O.D. Miller, and S.R. Kurtz. The opto-electronic physics that broke the efficiency limit in solar cells. In *Photovoltaic Specialists Conference (PVSC), 2012 38th IEEE*, pages 001556–001559, 2012.

[34] John Markoff. Supercomputer decline topples Cray computer. *New York Times*, 1995.

[35] Sonal Singhal, A.K. Saxena, and S. Dasgupta. Estimation of various scattering parameters and 2-deg mobilities from electron mobility cal-

culations in the three conduction bands of gallium arsenide. *Pramana*, 69(4):687–692, 2007.

[36] G. Dresselhaus. Spin-orbit coupling effects in zinc blende structures. *Phys. Rev.*, 100:580–586, Oct 1955.

[37] T. Dietl, H. Ohno, F. Matsukura, J. Cibert, and D. Ferrand. Zener model description of ferromagnetism in zinc-blende magnetic semiconductors. *Science*, 287(5455):1019–1022, 2000.

[38] B W Wessels. Ferromagnetic semiconductors and the role of disorder. *New Journal of Physics*, 10(5):055008, 2008.

[39] T Fukumura, H Toyosaki, K Ueno, M Nakano, and M Kawasaki. Role of charge carriers for ferromagnetism in cobalt-doped rutile tio 2. *New Journal of Physics*, 10(5):055018, 2008.

[40] Yoon Shon, Sejoon Lee, D Y Kim, T W Kang, Chong S Yoon, Eun Kyu Kim, and Jeong Ju Lee. The structural, optical and magnetic properties and anomalous hall effect of InMnP:Zn epilayers. *New Journal of Physics*, 10(11):115002, 2008.

[41] C. Jacoboni and P. Lugli. *The Monte Carlo Method for Semiconductor Device Simulation*. Computational Microelectronics. Springer, 1989.

[42] R.G. Lerner and G.L. Trigg. *Encyclopedia of Physics*. Number v. 1 in Encyclopedia of Physics. Wiley, 2005.

[43] S. Saikin, Y.V. Pershin, and V. Privman. Modelling for semiconductor spintronics. *Circuits, Devices and Systems, IEE Proceedings -*, 152(4):366–376, 2005.

[44] Josh Barnes and Piet Hut. A hierarchical O(N log N) force-calculation algorithm. *Nature*, 324:446–449, 1986.

[45] U. Atxitia, O. Chubykalo-Fesenko, R. W. Chantrell, U. Nowak, and A. Rebei. Ultrafast spin dynamics: The effect of colored noise. *Phys. Rev. Lett.*, 102:057203, Feb 2009.

[46] Carlo Jacoboni and Lino Reggiani. The monte carlo method for the solution of charge transport in semiconductors with applications to covalent materials. *Rev. Mod. Phys.*, 55:645–705, Jul 1983.

[47] Makoto Matsumoto and Takuji Nishimura. Mersenne twister: A 623-dimensionally equidistributed uniform pseudo-random number generator. *ACM Trans. Model. Comput. Simul.*, 8(1):3–30, January 1998.

[48] Juan Soto. Statistical testing of random number generators. In *In: Proceedings of the 22nd National Information Systems Security Conference*, 1999.

[49] Lev Davydovich Landau and Evgenii Mikhailovich Lifshitz. *Quantum mechanics : non-relativistic theory.* Pergamon Press, Oxford [u.a.], 1994.

[50] A.D. MacNaught, A.R. Wilkinson, International Union of Pure, and Applied Chemistry. *Compendium of Chemical Terminology: Iupac Recommendations.* IUPAC Chemical Data Series. Blackwell Science, 1997.

[51] A.I.M. Rae. *Quantum mechanics.* Taylor & Francis Group, 2008.

[52] P. A. M. Dirac. The quantum theory of the emission and absorption of radiation. *Proceedings of the Royal Society of London. Series A*, 114(767):243–265, 1927.

[53] D.H. Perkins. *Introduction to High Energy Physics.* Cambridge University Press, 2000.

[54] N. Sclar. Neutral impurity scattering in semiconductors. *Phys. Rev.*, 104:1559–1561, Dec 1956.

[55] R. Gottinger, A. Gold, G. Abstreiter, G. Weimann, and W. Schlapp. Interface roughness scattering and electron mobilities in thin GaAs quantum wells. *EPL (Europhysics Letters)*, 6(2):183, 1988.

[56] H. Yukawa. On the interaction of elementary particles. *Proc. Phys. Math. Soc. Japan*, 1935.

[57] R.K. Pathria and P.D. Beale. *Statistical Mechanics.* Elsevier Science, 2011.

[58] I. Prigogine and S.A. Rice. *Advances in Chemical Physics.* Number v. 116 in Advances in Chemical Physics. Wiley, 2009.

[59] A. Dinklage. *Plasma Physics: Confinement, Transport and Collective Effects.* Lecture Notes in Physics. Springer, 2005.

[60] F.F. Chen. *Introduction to Plasma Physics and Controlled Fusion.* Number v. 1 in Introduction to Plasma Physics and Controlled Fusion. Springer, 1984.

[61] Carl A. Kukkonen and Henrik Smith. Validity of the Born approximation as applied to electron-electron scattering in metals: Implications for thermal conductivity. *Phys. Rev. B*, 8:4601–4606, Nov 1973.

[62] C. Kittel. *Quantum theory of solids.* Wiley, 1963.

[63] S. N. Bose. Plancks Gesetz und Lichtquantenhypothese. *Zeitschrift für Physik A Hadrons and Nuclei*, 26(1):178–181, December 1924.

[64] D. Vasileska and S.M. Goodnick. *Computational Electronics*. Synthesis lectures on computational electromagnetics. Morgan & Claypool Publishers, 2006.

[65] R.C. Tolman. *The Principles of Statistical Mechanics*. Dover Books on Physics. Dover Publications, 1938.

[66] William C. Swope, Hans C. Andersen, Peter H. Berens, and Kent R. Wilson. A computer simulation method for the calculation of equilibrium constants for the formation of physical clusters of molecules: Application to small water clusters. *The Journal of Chemical Physics*, 76(1):637–649, 1982.

[67] D. Richards, B. Jusserand, H. Peric, and B. Etienne. Intrasubband excitations and spin-splitting anisotropy in GaAs modulation-doped quantum wells. *Phys. Rev. B*, 47:16028–16031, Jun 1993.

[68] J.Y. Fu, M.Q. Weng, and M.W. Wu. Spin–orbit coupling in bulk GaAs. *Physica E: Low-dimensional Systems and Nanostructures*, 40(9):2890 – 2893, 2008.

[69] S. Oertel, J. Hübner, and M. Oestreich. High temperature electron spin relaxation in bulk GaAs. *Applied Physics Letters*, 93(13), 2008.

[70] J. H. Jiang and M. W. Wu. Electron-spin relaxation in bulk III-V semiconductors from a fully microscopic kinetic spin bloch equation approach. *Phys. Rev. B*, 79:125206, Mar 2009.

[71] B. Martin. *Statistics for Physical Sciences: An Introduction*. Elsevier Science, 2012.

[72] Loup Verlet. Computer “experiments” on classical fluids. i. thermodynamical properties of lennard-jones molecules. *Phys. Rev.*, 159:98–103, Jul 1967.

[73] William Pugh. Skip lists: A probabilistic alternative to balanced trees. *Commun. ACM*, 33(6):668–676, June 1990.

[74] Sheetal Kapoor, Gionni Marchetti, Fausto Rossi, and Irene D’Amico. Monte carlo study of temperature and bias dependence of spin transport in GaAs. *Journal of Physics: Conference Series*, 303(1):012095, 2011.

[75] J. Stoer and R. Bulirsch. *Introduction to Numerical Analysis.* Texts in Applied Mathematics. Springer, 2002.

[76] W.H. Press. *Numerical Recipes 3rd Edition: The Art of Scientific Computing.* Cambridge University Press, 2007.

[77] D.S. Bernstein. *Matrix Mathematics: Theory, Facts, and Formulas (Second Edition).* Princeton reference. Princeton University Press, 2009.

[78] L. Landau. Diamagnetismus der metalle. *Zeitschrift für Physik*, 64(9-10):629–637, 1930.

[79] S. Arlinghaus. *Practical Handbook of Curve Fitting.* Taylor & Francis, 1994.

[80] M. Plischke and B. Bergersen. *Equilibrium Statistical Physics.* World Scientific, 2006.

[81] Gionni Marchetti, Matthew Hodgson, James McHugh, Roy Chantrell, and Irene D'Amico. Spin relaxation in GaAs: Importance of electron-electron interactions. *Materials*, 7(4):2795–2814, 2014.

[82] E. Wigner. On the interaction of electrons in metals. *Phys. Rev.*, 46:1002–1011, Dec 1934.

[83] R. B. Dingle. Scattering of electrons and holes by charged donors and acceptors in semiconductors. *Phil.Mag.*, 46(379), 1955.

[84] TG Van de Roer and FP Widdershoven. Ionized impurity scattering in monte carlo calculations. *Journal of Applied Physics*, 59(3):813–815, 1986.

[85] F. Meier and B.P. Zakharchenya. *Optical Orientation.* Modern Problems in Condensed Matter Sciences. Elsevier Science, 1984.

[86] Travis Desell, Malik Magdon-Ismail, Boleslaw Szymanski, Carlos A. Varela, Benjamin A. Willett, Matthew Arsenault, and Heidi Newberg. Evolutionary N Body Simulations to Determine the Origin and Structure of the Milky Way Galaxy's Halo using Volunteer Computing. pages 1888–1895, 2011.

[87] Yongsheng Xu, Binbin Yao, Dan Liu, Weiwei Lei, Pinwen Zhu, Qiliang Cui, and Guangtian Zou. Room temperature ferromagnetism in new diluted magnetic semiconductor AlN:Mg nanowires. *CrystEngComm*, 15:3271–3274, 2013.

[88] Ivan Cimrák. A survey on the numerics and computations for the Landau-Lifshitz equation of micromagnetism. *Archives of Computational Methods in Engineering*, 15(3):1–37, 2007.

[89] Shufeng Zhang and Steven S.-L. Zhang. Generalization of the Landau-Lifshitz-Gilbert equation for conducting ferromagnets. *Phys. Rev. Lett.*, 102:086601, Feb 2009.

[90] T.L. Gilbert. A phenomenological theory of damping in ferromagnetic materials. *Magnetics, IEEE Transactions on*, 40(6):3443–3449, 2004.

[91] D. Suess, T. Schrefl, W. Scholz, J.-V. Kim, R.L. Stamps, and J. Fidler. Micromagnetic simulation of antiferromagnetic/ferromagnetic structures. *Magnetics, IEEE Transactions on*, 38(5):2397–2399, 2002.

[92] B. Skubic, O. E. Peil, J. Hellsvik, P. Nordblad, L. Nordström, and O. Eriksson. Atomistic spin dynamics of the cu-mn spin-glass alloy. *Phys. Rev. B*, 79:024411, Jan 2009.

[93] N. Kazantseva, U. Nowak, R. W. Chantrell, J. Hohlfeld, and A. Rebei. Slow recovery of the magnetisation after a sub-picosecond heat pulse. *EPL (Europhysics Letters)*, 81(2):27004, 2008.

[94] T.A. Ostler, J. Barker, R.F.L. Evans, R.W. Chantrell, U. Atxitia, O. Chubykalo-Fesenko, S. El Moussaoui, L. Le Guyader, E. Mengotti, L.J. Heyderman, F. Nolting, A. Tsukamoto, A. Itoh, D. Afanasiev, B.A. Ivanov, A.M. Kalashnikova, K. Vahaplar, J. Mentink, A. Kirilyuk, Th. Rasing, and A.V. Kimel. Ultrafast heating as a sufficient stimulus for magnetization reversal in a ferrimagnet. *Nat Commun*, 2012.

[95] J.C. Slater and N.H. Frank. *Electromagnetism.* Dover Books on Physics. Dover Publications, 2012.

[96] K.H.J. Buschow. *Encyclopedia of materials: science and technology.* Number v. 10 in Encyclopedia of Materials: Science and Technology. Elsevier, 2001.

[97] O. Kallenberg. *Foundations of Modern Probability.* Probability and Its Applications. Springer, 2002.

[98] Enrico Bibbona, Gianna Panfilo, and Patrizia Tavella. The ornstein–uhlenbeck process as a model of a low pass filtered white noise. *Metrologia*, 45(6):S117, 2008.

[99] Daniel T. Gillespie. Exact numerical simulation of the ornstein-uhlenbeck process and its integral. *Phys. Rev. E*, 54:2084–2091, Aug 1996.

[100] P. Bak, C. Tang, and K. Wiesenfeld. Self-organized criticality - an explanation of 1/f noise. *Physical Review Letters*, 59:381–384, July 1987.

[101] S. Kogan. *Electronic Noise and Fluctuations in Solids.* Cambridge University Press, 2008.

[102] S.V. Vonsovski. *Ferromagnetic resonance: the phenomenon of resonant absorption of a high-frequency magnetic field in ferromagnetic substances.* International series of monographs on solid state physics. Pergamon Press, 1966.

[103] D.J. Griffiths. *Introduction to Quantum Mechanics.* Prentice Hall International Editions. Prentice Hall International, 1994.

[104] John Dubinski. A parallel tree code. *New Astronomy*, 1(2):133 – 147, 1996.

[105] Xiankai Jiao, Yang Ren, Zongzhi Zhang, Qinyuan Jin, and Yaowen Liu. Modeling of the laser-heating induced ultrafast demagnetization dynamics in ferrimagnetic thin films. *Magnetics, IEEE Transactions on*, 49(7):3191–3194, 2013.